Radiocarbon (2025), **67**, pp. 709–718
doi:10.1017/RDC.2025.23

CAMBRIDGE UNIVERSITY PRESS

RESEARCH ARTICLE

On the impact of micro-CT scanning on radiocarbon dating of fossil material: A cautionary note for the palaeoanthropological community and beyond

Mathieu Duval[1,2,3], Laura Martín-Francés[1,4] and Rachel Wood[5,6]

[1]National Research Centre on Human Evolution (CENIEH), Paseo Sierra de Atapuerca, 3, 09002, Burgos, Spain, [2]Australian Research Centre for Human Evolution, Griffith University, 170 Kessels Road, Nathan, QLD 4111, Australia, [3]Palaeoscience Labs, Dept. Archaeology and History, La Trobe University, Melbourne Campus, Bundoora, VIC 3086, Australia, [4]Monash Biomedicine Discovery Institute, Department of Anatomy and Developmental Biology, Monash University, Wellington Road, Clayton, VIC 3800, Australia, [5]School of Archaeology, University of Oxford, 1 South Parks Road, OX1 3TG, Oxford, UK and [6]Research School of Earth Sciences, Australian National University, 1 Mills Road, Canberra 2601, Australia
Corresponding author: Rachel Wood; Email: rachel.wood@arch.ox.ac.uk

Received: 22 July 2024; **Revised:** 30 January 2025; **Accepted:** 20 February 2025; **First published online:** 14 July 2025

Keywords: fossil; mCT scanning; paleoanthropology; radiocarbon dating; X-rays

Abstract

In this study, we investigate the impact of X-rays produced by conventional mCT instruments on fossil materials dated by radiocarbon. Our results clearly show a decrease on the collagen preservation in fossil and modern bones and teeth, and therefore on the radiocarbon analytical results (in particular, the collagen yield and, possibly, stable isotope composition), after mCT scanning. In other words, all the samples analysed here have experienced a noticeable radiation damage, regardless of their nature (bone and dental tissue) and age (modern and fossil). Given these observations, a prudent approach would be for radiocarbon laboratories to expect lower collagen yields for samples that have been previously mCT scanned and ensure appropriately sized standards are processed alongside these samples. Additionally, samples with originally low collagen yields might become unsuitable for radiocarbon dating after mCT or at least show a yield lower than the usual minimum cut-off value. In this case, it might be viable to extend the collagen yield quality assurance parameter for mCT scanned bones and teeth and instead focus on the C:N ratio as the most appropriate indicator of collagen quality, although we cannot exclude that the latter may also be impacted by X-ray exposure. Further investigations on a larger set of samples are required to confirm these first observations. Nevertheless, in the light of these results, we can reasonably conclude by recommending caution regarding the systematic and unlimited use of mCT scanning in palaeoanthropology or in other related disciplines involving fossil material.

Introduction

In palaeoanthropological research, the study of human fossils is governed by the necessity to cause minimum damage to these rare and valuable remains (e.g., Fox and Hawkes 2019). In this context, micro-computerized tomography (mCT) scanning is now routinely used to record a high resolution three-dimensional reconstruction of samples, enabling to obtain critical information about fossil specimens and extinct species (e.g. García-Campos et al. 2020; Hernaiz-García et al. 2024; Martín-Francés et al. 2018; Smith et al. 2010), and create a digital archive of fossils that may be destructively analysed later. These destructive analyses may be carried out for a wide range of purposes, including palaeoenvironmental or palaeodietary reconstructions, mobility patterns, ancient DNA (aDNA) and geochronology. In particular, a few dating methods may be directly applied to fossil remains, such as radiocarbon, U-series and Electron Spin Resonance (ESR) (e.g., Grün 2006; Grün et al. 2010). Among

them, radiocarbon dating is by far the most widely used for fossils whose chronology is younger than 50 ka (e.g., Grün 2006; Hajdas et al. 2021). It is therefore crucial to establish whether mCT scanning procedures routinely employed in palaeoanthropology have a negative impact on the radiocarbon analysis of collagen samples, and, if any, to determine how this impact can be reduced. This has been very little investigated so far to our knowledge, despite extensive literature showing the ability of ionising radiation to alter the material it interacts with (e.g., Bertrand et al. 2015 and references therein).

Indeed, mCT scanning uses the interaction of X-rays with matter for imaging purpose. While X-rays are by definition ionising radiations that may induce some non-negligible changes in materials at the molecular or atomic level, mCT scanning remains nevertheless widely regarded as a non-destructive technique in palaeoanthropology (e.g. Olejniczak and Grine 2006; Tafforeau and Smith 2008; Tafforeau et al. 2006; or more recently, Mandl et al. 2022). This is because it usually does not cause any major visual damage to the fossils, which is the main criterion typically employed to evaluate the destructiveness of a technique (see Bertrand et al. 2015), although a change of colour (sometimes temporary) in fossils after X-ray synchrotron microtomography has been reported in a few works (Richards et al. 2012; Tafforeau and Smith 2008). Previous investigations have nevertheless showed that X-ray exposure may have a non-negligible 'radiation-induced side effect' (using the terminology employed by Bertrand et al. 2015; p. 131) on both the organic and mineral component of modern and fossil bones and teeth (e.g., Bailey 1964; Bowes and Moss 1962; Duval and Martín-Francés 2017; Grieshaber et al. 2008; Grün et al. 2012b; Immel et al. 2016; Rahman et al. 2018; Sauer et al. 2022). The magnitude of this effect is however largely dependent on the radiation dose absorbed by the material, which is directly proportional to the intensity of the irradiation source. This is why it is essential to make a distinction between conventional (*sensu* Immel et al. 2016), or commercial, mCT instruments, which are widely used in palaeoanthropology (and are the main focus of the present work) as part of routine scanning procedures for human fossil remains, and Synchrotron X-ray sources. Comparatively, the latter provide a significantly higher analytical resolution but are less frequently employed within the community. In that regard, Bertrand et al. (2015) point out that, "In the X-ray range, synchrotron beams are orders of magnitude more intense and brighter than conventional laboratory sources" (p. 129).

Only very few studies have examined the impact of X-rays produced by conventional mCT instruments on fossil materials. While X-ray exposure is known to create a radiation-induced ESR signal in tooth enamel that can be used for dating or dosimetric purpose (e.g., Grün et al. 2012a; Yu et al. 2022), the increasing need to directly date human fossils older than 50 ka (Grün and Stringer 2023) triggered a couple of studies specifically centred on mCT scanning. First, Grün et al. (2012b) initially estimated the dose values given to fossil tooth enamel by CT-scanning to be of several hundreds of Grays (Gy). More recently, Duval and Martín-Francés (2017) confirmed the significant impact of mCT scanning on the intensity of the ESR signal of fossil tooth enamel and estimated that conventional instruments are likely to add a few tens of Gy to fossil teeth when using standard experimental conditions. In contrast, when the metallic filter is removed, the X-ray dose absorbed by the sample may exceed 100 Gy, reaching a dose value of the same order of magnitude as in Grün et al. (2012b). The differences between the two studies are likely to be explained by the use of distinct acquisition parameters and mCT instruments. Regardless, these results consistently demonstrate that mCT scanning may lead to significant ESR age overestimations if the additional X-ray dose absorbed by the sample is not taken into account in the calculation.

In another work centred on fossil biomolecules and aDNA preservation in fossil bones, Immel et al. (2016) observed a clear correlation between decreasing aDNA quantities and increasing X-ray dose-levels above 2000 Gy. They also report no significant damage (i.e., nucleotide misincorporations) below 200 Gy, which is typically the range of dose given by conventional mCT scanners when using a metallic filter. However, a closer look at the Figure 2 of Immel et al. (2016) actually shows a significant reduction ($\sim$ 30–35%) of the aDNA quantitation after a 200 Gy irradiation, with a very sharp decline with increasing dose, suggesting nevertheless a non-negligible effect induced by mCT scanning at relatively low dose levels. The comparability of the integrated dose stated by this study with the dose measured by ESR in mCT (e.g., Duval and Martín-Francés 2017; Grün et al. 2012b) is difficult to

https://doi.org/10.1017/RDC.2025.23 Published online by Cambridge University Press

establish, as Immel et al. quantified the water equivalent surface dose. However, it appears that an increasing dose does have an impact on aDNA quantitation and may lead to significant nucleotide damage when using Synchrotron X-ray sources.

In radiocarbon dating, we are particularly concerned about the potential breakage of the protein component of bone and dentine, which primarily consists of collagen and is knowingly impacted by X-rays (Bailey 1964; Bowes and Moss 1962; Rahman et al. 2018). This protein consists of a triple helix that is insoluble, a characteristic exploited by routine radiocarbon pretreatment protocols where crude collagen is extracted by demineralization in acid (Longin 1971). However, the peptides become soluble once the helix cross-links are disrupted and/or the peptide chains are fragmented, meaning endogenous protein can be lost during demineralization (Marom et al. 2013). Further loss can occur later during during the ultrafiltration step in the pretreatment, where small fragments of the now solubilized gelatin are removed prior to dating (Brock et al. 2013; Brown 1988). Thus, it is possible that radiocarbon dating of bones or teeth that have been exposed to X-rays via a conventional mCT instrument may be more difficult because collagen yields are lower.

In the present work we examine whether mCT scanning using a conventional instrument and a range of standard acquisition parameters may influence radiocarbon analytical results, and especially collagen preservation, obtained from a few modern and fossil bones and teeth.

1. Material and methods

1.1. Samples

We selected two types of samples: one fossil bone (sample ID: ZAGLIK) from a woolly rhinoceros found at the Marine Isotopic Stage (MIS) 5 locality of Zaglik, Irkusk, Russia, and commonly considered as a laboratory standard reference with multiple radiocarbon dates >50 ka (Wood et al. 2023) at the Australian National University (ANU) Radiocarbon Facility, and one tooth sample (M2) belonging to a modern pig (roadkill) from France (sample ID: FP_LM2). Several samples were cut from the ZAGLIK bone and the dentine of FP_LM2: one was directly analysed for radiocarbon (ZAGLIK and FP_LM2) and the others were submitted to various mCT analyses (labeled A, B, C; see Table 1). Samples were taken from neighbouring areas of the bone/tooth to ensure they were as similar as possible in terms of preservation and minimize the uncertainty related to spatial heterogeneity.

1.2. mCT conditions

The samples were mCT scanned with a GE Phoenix v/tome/x_s 240 instrument at at the University of Bordeaux (PACEA/PLACAMAT), France. We selected the set of parameters based on those typically used to scan human fossils (e.g., Martín-Francés et al. 2022; Martinón-Torres et al. 2021; Zanolli et al. 2019): 80–180 kV, 100–300 µA, a 0.1 mm Cu filter and voxel size < 22 µm (Table 1). The mCT instrument and experimental conditions are similar to those previously employed by Duval and Martín-Francés (2017), ensuring thus the acquisition of comparable data.

Table 1. *Overview of the main acquisition parameters employed during mCT experiments*

Sample ID	Type	Number of images	Voltage (kV)	Current (µA)	Filter
FP_LM2_A	Dentine	2550	100	120	0.1 mm Cu
ZAGLIK_A	Bone	2550	80	100	0.1 mm Cu
ZAGLIK_B	Bone	2550	120	200	0.1 mm Cu
ZAGLIK_C	Bone	2550	180	300	0.1 mm Cu

https://doi.org/10.1017/RDC.2025.23 Published online by Cambridge University Press

Table 2. *Effect of mCT scanning on radiocarbon dating*

Sample ID	Subsample	mCT scanned	ANU internal lab number N#	S-ANU#	$F^{14}C$ ± error	Radiocarbon age (yr BP)
FP_LM	1	No	22890	68118	1.0622 ± 0.0027	Not calculated (modern roadkill)
FP_LM2_A	1	Yes	22891	68119	1.0544 ± 0.0025	Not calculated (modern roadkill)
ZAGLIK_mCTA	1	Yes	21318	65433	0.0010 ± 0.00137	>44900
ZAGLIK_mCTB	1	Yes	21321	65418	0.0024 ± 0.00129	>42600
ZAGLIK_mCTC	1	Yes	21324	65419	0.0004 ± 0.00163	>45100

1.3. Collagen extraction

Collagen was extracted using an ultrafiltration protocol at the ANU. After removing the surface with a handheld Dremel drill, bone was crushed using a pestle and mortar to a coarse powder and dentine drilled. Thus, aliquots of the same sample were roughly homogenized before pretreatment.

Pretreatment consisted of reaction with HCl (0.5 M, RT-5°C, overnight), NaOH (0.1M, RT, 30 min) and HCl (0.5 M, RT, 1 hour), followed by gelatinization (0.001M HCl, 70°C, 20 hours), filtration (Ezee™ Filter) and ultrafiltration (Vivaspin™ VS15Turbo 30 MWCO, polyethersulphone membrane) (full details are given in Wood et al. 2023). Cleaned samples were converted to graphite by combustion in a sealed tube with CuO wire and Ag foil, and CO_2 was cryogenically collected and purified before reaction with H_2 over an Fe catalyst. Samples were dated on a NEC SS-AMS (Fallon et al. 2010). Radiocarbon dates were calculated following Stuiver and Polach (1977) using an AMS derived $\delta^{13}C$, and a collagen specific background correction was made (Wood et al. 2023). Carbon and nitrogen stable isotope and elemental abundance of the tooth dentine collagen was analysed using an ANCA-GSL connected to a Sercon 20-22 IRMS operating in continuous flow mode using an in-house gelatin reference. Data was scaled using USGS40, USGS65 and IAEA-C6, and data accuracy assessed with IAEA-600 and USGS61 (Wood et al. 2023). All other samples were measured at the Oxford Radiocarbon Accelerator Unit on a similar instrument, but against an internal alanine standard and using USGS40 and USGS41 to scale the data. In both laboratories, uncertainty was assessed by repeat measurement of the internal standard, and was less than 0.1‰, at 1 sigma for both $\delta^{13}C$ and $\delta^{15}N$.

To reduce potential variables, scanned and unscanned samples were of the same starting mass and were pretreated at the same time and by the same person. For samples with sufficient amount of material, several subsamples were analysed and went through pretreatment separately. Collagen yield is calculated as collagen mass (mg) divided by starting mass (mg), multiplied by 100. Numerical results are given in Tables 2 and 3.

2. Results and discussion

Radiocarbon analyses of the scanned ZAGLIK samples return minimum C-14 ages of >42,600 to >45,100 BP, i.e. in agreement with the known MIS 5 age (Table 2). In other words, we do not observe any significant impact of mCT scanning on the radiocarbon age obtained.

In contrast, collagen yields are significantly reduced (Table 3). For unscanned bone samples, collagen yields were around 7.1%. After mCT scanning, collagen yields were reduced to <5%, suggesting protein is damaged during the scanning process. The scanned and unscanned samples clearly cluster in two groups (Figure 1) showing a reduction of 33% to 42% of the collagen yield after scanning.

https://doi.org/10.1017/RDC.2025.23 Published online by Cambridge University Press

Table 3. *Effect of mCT on collagen yield, carbon and nitrogen stable isotope ratios/values and atomic C:N ratio. Key: s.d. = standard deviation; c.v. = coefficient of variation; n.a. = not applicable*

Sample ID	Subsample	ANU internal lab number N#	Initial pretreatment sample wt (mg)	Pretreatment yield (mg)	Collagen yield (%)	$\delta^{15}N$	$\delta^{13}C$	C:N ratio
French pig (not scanned)								
FP_LM	1	22890	101	6.13	6.2	4.18	–21.79	3.09
French pig (scanned)								
FP_LM2_A	1	22891	98	4.06	4.0	4.49	–21.95	3.09
Zaglik (not scanned, pretreated at the same time as the scanned samples)								
ZAGLIK	1	21315	293	20.6	7.0	7.77	–19.78	3.23
ZAGLIK	2	21316	269	20.1	7.5	7.76	–19.81	3.22
ZAGLIK	3	21317	248	16.6	6.7	7.81	–19.72	3.22
ZAGLIK average ± 1 s.d. (c.v.)					*7.1 ± 0.4 (5.5%)*	*7.78 ± 0.03 (0.3%)*	*–19.77 ± 0.05 (0.2%)*	*3.22 ± 0.006 (0.2%)*
Zaglik (not scanned, pretreated at a different time to the scanned samples)								
ZAGLIK	n.a.	18066	494	25.1	5.1	7.70	–19.61	3.21
ZAGLIK	n.a.	18298	621	41.0	6.6	7.52	–19.70	3.21
ZAGLIK	n.a.	18972	490	36.3	7.4	8.03	–19.35	3.21
ZAGLIK	n.a.	19584	512	44.2	8.6	7.73	–19.46	3.21
ZAGLIK	n.a.	19740	538	30.7	5.7	7.58	–19.42	3.21
ZAGLIK	n.a.	20454	557	44.3	8.0	7.58	–19.27	3.20
ZAGLIK	n.a.	21160	576	37.8	6.6	7.85	–19.51	3.20
ZAGLIK average ± 1 s.d. (c.v.)					*6.8 ± 1.2*	*7.71 ± 0.18 (2.3%)*	*–19.47 ± 0.15 (–0.8%)*	*3.21 ± 0.005 (0.2%)*
Zaglik (scanned)								
ZAGLIK_mCTA	1	21318	271	12.3	4.5	7.23	–19.92	3.25
ZAGLIK_mCTA	2	21319	271	13.4	4.9	7.34	–19.84	3.21
ZAGLIK_mCTA average ± 1 s.d. (c.v.)					*4.7 ± 0.3 (6.0%)*	*7.29 ± 0.08 (1.1%)*	*–19.88 ± 0.06 (0.3%)*	*3.23 ± 0.03 (0.9%)*
ZAGLIK_mCTB	1	21321	253	10.4	4.1	7.25	–19.88	3.24
ZAGLIK_mCTC	1	21324	273	13.1	4.8	7.36	–19.80	3.22
ZAGLIK_mCTC	2	21325	273	12.1	4.4	7.29	–19.83	3.21
ZAGLIK_mCTC average (± 1 s.d.)					*4.6 ± 0.3 (6.1%)*	*7.33 ± 0.05 (0.7%)*	*–19.82 ± 0.02 (0.1%)*	*3.22 ± 0.007 (0.2%)*

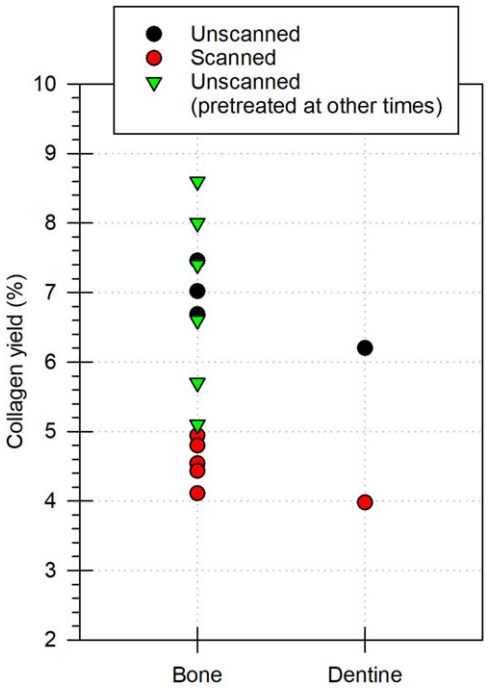

Figure 1. *Graphical overview of the collagen yield values obtained from the bone and dentine samples. Numerical results may be found in Table 3.*

Interestingly, a similar reduction (36%) is independently obtained from the dentine sample, suggesting that mCT scanning may equally impact materials showing somewhat different characteristics (i.e., modern and fossil remains, bones and dental tissues). Additionally, several scanned and unscanned subsamples of the ZAGLICK bone sample were analysed, showing similar variability in collagen yields of about 5.7% to 6.1% (1 standard deviation; Table 3). This illustrates the magnitude of the existing intrinsic uncertainty on the collagen yield results obtained from each fossil specimen. This general uncertainty most likely results from the combined uncertainties associated with the homogeneity of the ZAGLIK bone and the chemical procedure.

Figure 2 shows that there is no strong apparent correlation between the X-ray intensity (expressed in voltage and current) and the collagen yield: while there is a clear drop in the yield after mCT scanning, all mCT scanned subsamples nevertheless return somewhat similar yields, regardless of the voltage (between 80 and 180 kV) and current (100 to 300 μA) values employed. Since experimental conditions employed in the present study are similar to those used earlier by Duval and Martín-Francés (2017), the maximum dose absorbed by the samples under high voltage (180 kV) and current (300 μGy) settings may be reasonably estimated to a few tens of Gy. The lower yield obtained for sample ZAGLIK_B (4.1%) is in agreement with those obtained from the other scanned samples at a 2σ confidence level when considering the existing intra-sample variability (about 6.0% on average at 1σ; Table 3). Additionally, the values obtained for the dentine samples are comparable with those from the bone (Figure 2).

The drop in collagen yield is unlikely to be caused by heterogeneity of the ZAGLIK bone. Seven crushed aliquots of around 500 mg have been pretreated as part of the routine ANU laboratory throughput. Scatter is likely to reflect the maximum variation expected, as they were taken from various locations scattered across the bone and were processed at different times and by different people. While they vary by about 18.1% (1 s.d.), ranging from 5.1 to 8.6% (Table 3), all values are nevertheless

https://doi.org/10.1017/RDC.2025.23 Published online by Cambridge University Press

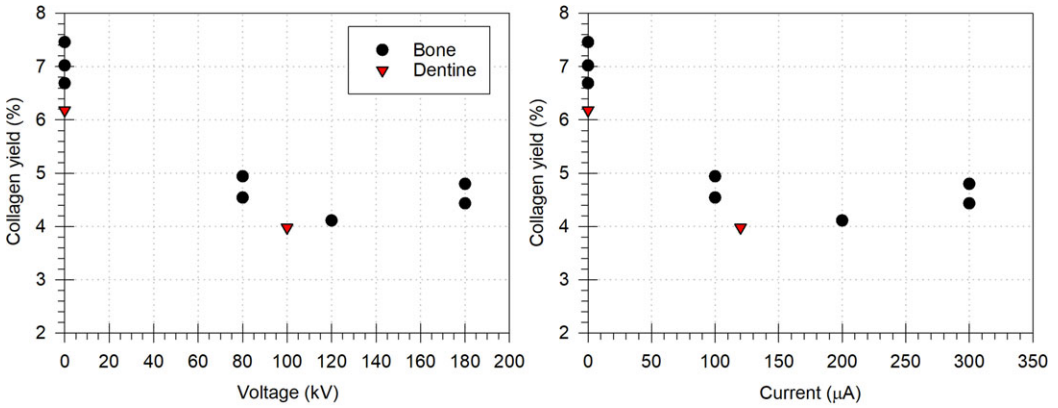

Figure 2. *Impact of the Voltage (left) and Current (right) values employed during the mCT scanning experiments on the collagen yields. Numerical results may be found in Table 3.*

systematically > 5%, i.e. higher than the collagen yield measured from the scanned samples (Figure 1).

These observations are compatible with those from Immel et al. (2016) who observed a similar drop in aDNA quantitation after mCT scanning, but no apparent trend in the low dose range (<1,000 Gy) corresponding to conventional mCT instruments. We hypothesize that the reduction in collagen yield after mCT may be the direct result of radiation damage. Small, damaged fragments of collagen may be either lost in the demineralization stage if soluble, or during ultrafiltration. Additionally, it is possible that minor damage induced by ionising radiation may be amplified during the aggressive acid-base-acid-gelatinization procedure, which is able to hydrolyze peptides, culminating in the removal of a greater portion of the smallest fragments during ultrafiltration. This process is markedly different from aDNA extraction procedures, where soluble components are extracted from bone. Further work is required to confirm this hypothesis.

In these two well-preserved samples, collagen yields remain well above the minimum cut-offs of 0.5 or 1% typically used in radiocarbon laboratories after mCT (e.g., Petchey et al. 2014; van Klinken 1999; Wood et al. 2023). However, the significant reduction of the collagen yield induced by mCT scanning may have two main implications. First, a larger sample may simply be required for radiocarbon analyses from bones and teeth that have undergone previous scanning. Unfortunately, only the most morphologically valuable fossil samples are usually subject to mCT, so this is likely to be problematic. A more prudent approach may be for radiocarbon laboratories to expect lower collagen yields and ensure appropriately-sized standards are processed alongside these samples. If very small samples are extracted containing substantially less than 1mg carbon, precision on the age estimate will decrease. Additionally, samples with originally low collagen yield might also become unsuitable for C-14 dating after mCT scanning, or at least show a yield lower than the usual minimum cut-off value. Consequently, it would be viable to extend the collagen yield quality assurance parameter for mCT scanned bones and teeth and instead focus on C:N ratio as the most appropriate indicator of collagen quality.

However, our results suggest that carbon and nitrogen stable isotopes might also be affected by mCT scanning, although it is important to note that the effect appears very minor (although noticeable), and at most 0.5‰ (Table 3 and Figure 3). There appears to be some heterogeneity within the ZAGLIK bone, with protein extracted at different times to this experiment and from different parts of the bone scattering by 0.5‰ for both $\delta^{13}C$ and $\delta^{15}N$ ratios. The three aliquots extracted from the bone at the same time as the scanned samples are more closely grouped and fall within the measurement uncertainty. In contrast, the data from the bone that had been mCT scanned is depleted in the heavy isotope of both carbon and nitrogen, but we see a particularly large shift (~0.4–0.5‰) in $\delta^{15}N$. No impact is visible on the C:N values, as some scanned subsamples do show somewhat higher ratios, while others return values similar

https://doi.org/10.1017/RDC.2025.23 Published online by Cambridge University Press

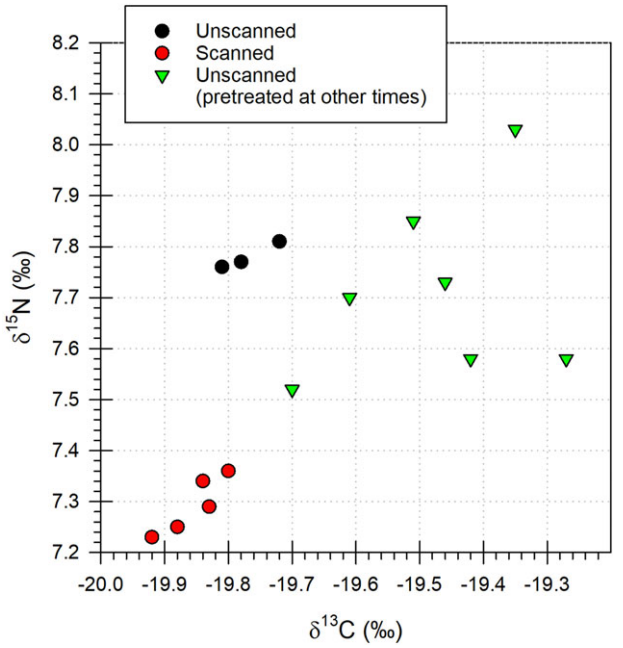

Figure 3. *Graphical overview of the effect of mCT scanning on carbon and nitrogen stable isotope ratios obtained on the Zaglik bone sample. Measurement uncertainty of each point is less than ± 0.1‰, at 1 sigma for both $\delta^{13}C$ and $\delta^{15}N$ ratios. Numerical results may be found in Table 3.*

to the unscanned subsamples (Table 3). The stable isotope composition of bone can vary spatially because the bone is formed at different times during an individual's life. However, the ZAGLIK samples treated alongside the mCT scanned bone were taken from an adjacent location on the bone. Additionally, the mCT scanned samples are clearly distinct from all other subsamples of this bone. Stable isotope results from the pig tooth are less clear as only two samples were analysed. It is possible therefore, that the mCT process has affected the stable isotope values obtained from the bone. This could be expected if different proteins are damaged to different extents during the scanning process. However, given the heterogeneity of the ZAGLIK bone and the very small effect observed, we suggest that this conclusion needs to be investigated further.

3. Conclusion

The common assumption in palaeoanthropology that mCT scanning is a non-destructive technique because it usually does not induce any major visible damage to fossils should probably be reconsidered. Our results contribute to a growing body of evidence indicating that there are undoubtedly non-negligible radiation-induced side effects on the fossils. While we do acknowledge the limitations of the present work (small number of samples analysed), our results nevertheless clearly show the systematic impact of routine mCT scanning (i.e., using a conventional instrument and standard acquisition parameters) on the collagen preservation in fossil bones and teeth. In particular, collagen yield and, possibly, stable isotope analytical results, seem to be affected by X-ray exposure. We nevertheless realize that additional mCT experiments will be required in the future in order to properly quantify the variability of this impact and evaluate to what extent its magnitude may depend on the mCT scanning instrument employed, or the geographic origin, geological context, chronology, preservation and/or fossilization degree of the samples analysed.

https://doi.org/10.1017/RDC.2025.23 Published online by Cambridge University Press

This is the second study showing that mCT scanning of fossils may have a non-negligible impact on dating results, after a similar work focused on Electron Spin Resonance (ESR) dating (Duval and Martín-Francés 2017). It is the first to suggest that we may see an effect on stable carbon and nitrogen isotope composition, although this is a very minor effect and a more tentative observation that requires further investigations in the future. We therefore recommend caution regarding the systematic and unlimited use of mCT scanning in palaeoanthropology or in any other related disciplines involving fossil material.

Acknowledgments. Dr. Ronan Ledevin (Lab Engineer at PACEA, University of Bordeaux) assisted with mCT scanning; Stewart Fallon, Eric Usher and Rebecca Esmay, ANU, helped with radiocarbon dating analyses. Aspects of this research were covered by the Spanish Ramón y Cajal Fellowship (M.D.) RYC2018-025221-I funded by MCIN/AEI/ 10.13039/501100011033 and by "ESF Investing in your future." This work is supported by the Horizon Program-Marie Sklodowska-Curie Actions of the EU Ninth programme (2021–2027) under the HORIZON-MSCA-2021-PF-01-Project: 101060482 (L. M-F). This study is also part of Grants PID2021-123092NB-C22 and PID2021-122355NB-C33 funded by MCIN/AEI/ 10.13039/501100011033/'ERDF A way of making Europe'. Finally, we thank the two anonymous reviewers for constructive comments on the manuscript.

Declaration of competing interests. The authors declare that they have no known competing financial interests that could have appeared to influence the work reported in this paper.

References

Bertrand L, Schöeder S, Anglos D, Breese MBH, Janssens K, Moini M and Simon A (2015) Mitigation strategies for radiation damage in the analysis of ancient materials. *Trends in Analytical Chemistry* **66**, 128–145.

Bailey AJ, Rhodes DN and Cater CW (1964) Irradiation-induced crosslinking of collagen. *Radiat. Res.* **22**, 606–621.

Bowes JH and Moss JA (1962) The effect of gamma irradiation on collagen. *Radiat. Res.* **16**, 211–223.

Brock F, Geoghegan V, Thomas B, Jurkschat K and Higham TFG (2013) Analysis of bone "collagen" extraction products for radiocarbon dating. *Radiocarbon* **55**(2), 445–463. doi: 10.1017/S0033822200057581.

Brown TA, Nelson DE, Vogel JS and Southon JR (1988) Improved collagen extraction by modified Longin method. *Radiocarbon* **30**(2), 171–177.

Duval M and Martín-Francés L (2017) Quantifying the impact of µCT-scanning of human fossil teeth on ESR age results. *American Journal of Physical Anthropology* **163**(1), 205–212. doi: 10.1002/ajpa.23180.

Fallon SJ, Fifield LK and Chappell JM (2010) The next chapter in radiocarbon dating at the Australian National University: Status report on the single stage AMS. *Nucl. Instrum. Methods Phys. Res. B* **268**(7–8), 898–901. doi: 10.1016/j.nimb.2009.10.059.

Fox K and Hawks J (2019) Use ancient remains more wisely. *Nature* **572**(7771), 581–583. doi: 10.1038/d41586-019-02516-5. PMID: 31462783.

García-Campos C, Modesto-Mata M, Martinón-Torres M, Martínez de Pinillos M, Martín-Francés L, Arsuaga JL and Bermúdez de Castro JM (2020) Sexual dimorphism of the enamel and dentine dimensions of the permanent canines of the Middle Pleistocene hominins from Sima de los Huesos (Burgos, Spain). *Journal of Human Evolution* **144**, 102793. doi: 10.1016/j.jhevol.2020.102793.

Grieshaber BM, Osborne DI, Doubleday AF and Kaestle FA (2008) A pilot study into the effects of X-ray and computed tomography exposure on the amplification of DNA from bone. *Journal of Archaeological Science* **35**, 681–687.

Grün R (2006) Direct dating of human fossils. *American Journal of Physical Anthropology* **131**(S43), 2–48.

Grün R, Aubert M, Hellstrom J and Duval M (2010) The challenge of direct dating old human fossils. *Quaternary International* **223–224**, 87–93.

Grün R, Mahat R and Joannes-Boyau R (2012a) Ionization efficiencies of alanine dosimeters and tooth enamel irradiated by gamma and X-ray sources. *Radiation Measurements* **47**(9), 665–668.

Grün R, Athreya S, Raj R and Patnaik R (2012b) ESR response in tooth enamel to high-resolution CT scanning. *Archaeol Anthropol Sci* **4**, 25–28. doi: 10.1007/s12520-011-0079-7.

Grün R and Stringer C (2023) Direct dating of human fossils and the ever-changing story of human evolution. *Quaternary Science Reviews* 322.

Hajdas I, Ascough P, Garnett MH, Fallon SJ, Pearson CL, Quarta G, Spalding KL, Yamaguchi H and Yoneda M (2021) Radiocarbon dating. *Nat Rev Methods Primers* **1**, 62. doi: 10.1038/s43586-021-00058-7.

Hernaiz-García M, Zanolli C, Martín-Francés L, Mazurier A, Benazzi S, Sarig R, Fu J, Kullmer O and Fiorenza L (2024) Masticatory habits of the adult Neanderthal individual BD 1 from La Chaise-de-Vouthon (France). *American Journal of Biological Anthropology* e24926. doi: 10.1002/ajpa.24926.

Immel A, Le Cabec A, Bonazzi M, Herbig A, Temming H, Schuenemann VJ, Bos KI, Langbein F, Harvati K, Bridault A, Pion G, Julien M-A, Krotova O, Conard NJ, Münzel SC, Drucker DG, Viola B, Hublin J-J, Tafforeau P and Krause J (2016) Effect of X-ray irradiation on ancient DNA in sub-fossil bones - Guidelines for safe x-ray imaging. *Scientific Reports* **6**, 32969. doi: 10.1038/srep32969.

Longin R (1971) New method of collagen extraction for radiocarbon dating. *Nature* **230** (5291), 241–242.

https://doi.org/10.1017/RDC.2025.23 Published online by Cambridge University Press

Mandl K, Carlson KSD, Brönnimann D, McCall A, Grassberger M, Teschler-Nicola M, Weiss-Krejci E and Metscher B (2022) Substantiating microCT for diagnosing bioerosion in archaeological bone using a new Virtual Histological Index (VHI). *Archaeological and Anthropological Sciences* **14**(6), 104.

Marom A, McCullagh JSO, Higham TFG and Hedges REM (2013) Hydroxyproline dating: Experiments on the ^{14}C analysis of contaminated and low-collagen bones. *Radiocarbon* **55**(2), 698–708. doi: 10.1017/S0033822200057854

Martín-Francés L, Martinón-Torres M, Martínez de Pinillos M, García-Campos C, Modesto-Mata M, Zanolli C, Rodríguez L and Bermúdez de Castro JM (2018) Tooth crown tissue proportions and enamel thickness in Early Pleistocene Homo antecessor molars (Atapuerca, Spain). *PLoS ONE* **13**(10), e0203334.

Martín-Francés L, Bermúdez de Castro JM, de Pinillos MM, Martinón-Torres M, Arsuaga JL, Bertrand B and Vialet A (2022) Middle Pleistocene hominin teeth from Biache-Saint-Vaast, France. *Archaeological and Anthropological Sciences* **14**, 215. doi: 10.1007/s12520-022-01680-6.

Martinón-Torres M, d'Errico F, Santos E, Álvaro Gallo A, Amano N, Archer W, Armitage SJ, Arsuaga JL, Bermúdez de Castro JM, Blinkhorn J, Crowther A, Douka K, Dubernet S, Faulkner P, Fernández-Colón P, Kourampas N, González García J, Larreina D, Le Bourdonnec F-X, MacLeod G, Martín-Francés L, Massilani D, Mercader J, Miller JM, Ndiema E, Notario B, Pitarch Martí A, Prendergast ME, Queffelec A, Rigaud S, Roberts P, Shoaee MJ, Shipton C, Simpson I, Boivin N and Petraglia MD (2021) Earliest known human burial in Africa. *Nature* **593**(7857), 95–100.

Martinón-Torres M, Martín-Francés L, Gracia A, Olejniczak AJ, Prado-Simón L, Gómez-Robles A, Lapresa M, Carbonell E, Arsuaga JL and Bermúdez de Castro JM (2011) Early Pleistocene human mandible from Sima del Elefante (TE) cave site in Sierra de Atapuerca (Spain): A palaeopathological study. *Journal of Human Evolution* **61**, 1–11.

Olejniczak AJ and Grine FE (2006) Assessment of the accuracy of dental enamel thickness measurements using microfocal X-ray computed tomography. *The Anatomical Record Part A: Discoveries in Molecular, Cellular, and Evolutionary Biology* **288A**(3), 263–275.

Petchey F, Spriggs M, Bedford S, Valentin F and Buckley H (2014) Radiocarbon dating of burials from the Teouma Lapita cemetery, Efate, Vanuatu. *Journal of Archaeological Science* **50**, 227–242. doi: 10.1016/j.jas.2014.07.002.

Rahman N, Khan R and Badshah S (2018) Effect of x-rays and gamma radiations on the bone mechanical properties: literature review. *Cell Tissue Bank* **19**, 457–472. https://doi.org/10.1007/s10561-018-9736-8.

Richards GD, Jabbour RS, Horton CF, Ibarra CL and MacDowell AA (2012) Color changes in modern and fossil teeth induced by synchrotron microtomography. *Am. J. Phys. Anthropol.* **149**, 172–180. https://doi.org/10.1002/ajpa.22103.

Sauer K, Zizak I, Forien JB, Rack A, Scoppola E and Zaslansky P (2022) Primary radiation damage in bone evolves via collagen destruction by photoelectrons and secondary emission self-absorption. *Nat. Commun.* **13**, 7829. https://doi.org/10.1038/s41467-022-34247-z.

Smith TM, Tafforeau P, Reid DJ, Pouech J, Lazzari V, Zermeno JP, Guatelli-Steinberg D, Olejniczak AJ, Hoffman A, Radovčić J, Makaremi M, Toussaint M, Stringer C and Hublin J-J (2010) Dental evidence for ontogenetic differences between modern humans and Neanderthals. *Proceedings of the National Academy of Sciences* **107**(49), 20923.

Stuiver M and Polach HA (1977) Discussion reporting of ^{14}C data. *Radiocarbon* **19**(3), 355–363. doi: 10.1017/S0033822200003672.

Tafforeau P, Boistel R, Boller E, Bravin A, Brunet M, Chaimanee Y, Cloetens P, Feist M, Hoszowska J, Jaeger JJ, Kay RF, Lazzari V, Marivaux L, Nel A, Nemoz C, Thibault X, Vignaud P and Zabler S (2006) Applications of X-ray synchrotron microtomography for non-destructive 3D studies of paleontological specimens. *Applied Physics A* **83**(2), 195–202.

Tafforeau P and Smith TM (2008) Nondestructive imaging of hominoid dental microstructure using phase contrast X-ray synchrotron microtomography. *Journal of Human Evolution* **54**(2), 272–278.

van Klinken GJ (1999) Bone collagen quality indicators for palaeodietary and radiocarbon measurements. *Journal of Archaeological Science* **26**(6), 687–695. doi: 10.1006/jasc.1998.0385.

Wood RE, Esmay R, Usher E and Fallon SJ (2023) Sample preparation methods used at the Australian National University radiocarbon facility. *Radiocarbon* **65**(2), 573–589. doi: 10.1017/RDC.2022.97.

Yu W, Herries AIR and Joannes-Boyau R (2022) Using X-rays as an irradiation source for direct ESR dating of fossil teeth. *Quaternary Geochronology* **72**, 101372.

Zanolli C, Biglari F, Mashkour M, Abdi K, Monchot H, Debue K, Mazurier A, Bayle P, Le Luyer M, Rougier H, Trinkaus E and Macchiarelli R (2019) A Neanderthal from the Central Western Zagros, Iran. Structural reassessment of the Wezmeh 1 maxillary premolar. *Journal of Human Evolution* **135**, 102643. doi: 10.1016/j.jhevol.2019.102643.

Cite this article: Duval M, Martín-Francés L, and Wood R (2025). On the impact of micro-CT scanning on radiocarbon dating of fossil material: A cautionary note for the palaeoanthropological community and beyond. *Radiocarbon* **67**, 709–718. https://doi.org/10.1017/RDC.2025.23

Title
Effects of ex vivo ionizing radiation on collagen structure and whole-bone mechanical properties of mouse vertebrae

Authors
Pendleton, Megan M
Emerzian, Shannon R
Liu, Jennifer
et al.

Publication Date
2019-11-01

DOI
10.1016/j.bone.2019.115043

Peer reviewed

Effects of *ex vivo* Ionizing Radiation on Collagen Structure and Whole-Bone Mechanical Properties of Mouse Vertebrae

*Megan M. Pendleton[1], *Shannon R. Emerzian[1], Jennifer Liu[2], Simon Y. Tang[2,3,4], Grace D. O'Connell[1,5], Joshua S. Alwood[6], Tony M. Keaveny[1,7]

[1]Department of Mechanical Engineering and [7]Department of Bioengineering

University of California

Berkeley, California, USA

[2]Department of Orthopaedic Surgery and [3]Department of Biomedical Engineering and [4]Department of Material Science & Mechanical Engineering

Washington University

St. Louis, Missouri, USA

[5]Department of Orthopaedic Surgery

University of California

San Francisco, California, USA

[6]Space Biosciences Division

NASA Ames Research Center

Moffett Field, California, USA

*these authors contributed equally to this work

Submitted to: Bone

Corresponding author: Tony M. Keaveny; tonykeaveny@berkeley.edu

5124 Etcheverry Hall, Mailstop 1740
University of California
Berkeley, CA 94720-1740

Abstract:

Bone can become brittle when exposed to ionizing radiation across a wide range of clinically relevant doses that span from radiotherapy (accumulative 50 Gy) to sterilization (~35,000 Gy). While irradiation-induced embrittlement has been attributed to changes in the collagen molecular structure, the relative role of collagen fragmentation versus non-enzymatic collagen crosslinking remains unclear. To better understand the effects of radiation on the bone material without cellular activity, we conducted an *ex vivo* x-ray radiation experiment on excised mouse lumbar vertebrae. Spinal tissue from twenty-week old, female, C57BL/6J mice were randomly assigned to a single x-ray radiation dose of either 0 (control), 50, 1,000, 17,000, or 35,000 Gy. Measurements were made for collagen fragmentation, non-enzymatic collagen crosslinking, and both monotonic and cyclic-loading compressive mechanical properties. We found that the group differences for mechanical properties were more consistent with those for collagen fragmentation than for non-enzymatic collagen crosslinking. Monotonic strength at 17,000 and 35,000 Gy was lower than that of the control by 50% and 73% respectively, ($p < 0.001$) but at 50 and 1,000 Gy was not different than the control. Consistent with those trends, collagen fragmentation only occurred at 17,000 and 35,000 Gy. By contrast, non-enzymatic collagen crosslinking was greater than control for all radiation doses ($p < 0.001$). All results were consistent both for monotonic and cyclic loading conditions. We conclude that the reductions in bone compressive monotonic strength and fatigue life due to *ex vivo* ionizing radiation are more likely caused by fragmentation of the collagen backbone than any increases in non-enzymatic collagen crosslinks.

Key Words (6 max): ionizing radiation; bone strength; fatigue; collagen; sterilization; bone-graft

Highlights (3-5 bullet points; maximum 20 words per bullet):

- *Ex vivo* ionizing radiation of whole-bones caused a reduction in compressive monotonic strength and fatigue life.

- Decreased strength was best explained by collagen fragmentation, not the accumulation of non-enzymatic collagen crosslinks.
- Non-enzymatic collagen crosslinks may play a smaller role in degrading mechanical strength of bone than previously considered.
- Irradiation has unique effects on cyclic behavior that are not manifested in static behavior.

1 Introduction

For a variety of clinical applications, bones are exposed to a wide range of ionizing radiation doses. *In vivo*, radiotherapy treatment results in an accumulated localized dose of ~50 Gy[1] in cancer patients [1–3]. *Ex vivo*, bone allografts are sterilized at a dose of 30,000 ± 5,000 Gy [4,5]. While these high-dose applications are critical for overall patient health and safety, high levels of ionizing radiation exposure have been shown to increase risk of fracture [6,7]. For example, for women with anal, rectal or colon cancer, those treated with radiation therapy were more than three times as likely to suffer a pelvic fracture than those without radiation therapy [8]. Furthermore, for patients with implanted bone allografts, allografts sterilized with radiation were twice as likely to fail compared to allografts sterilized using other methods [9]. The increased risk of fracture clinically has led to research into the effect of high levels of ionizing radiation exposure on the mechanical and biochemical properties of bone.

Numerous *ex vivo* studies on either cortical or cancellous bone have demonstrated that ionizing radiation degrades mechanical properties and collagen molecular structure independent of cellular activity. The demonstrated reduction in post-yield properties — ultimate strain, ultimate strength, fracture toughness, work-to-failure — of irradiated bone [10–15] has been attributed to changes in collagen molecular structure [16–18]. Though the exact mechanism dominating irradiation-induced collagen degradation is not fully known, two mechanisms have been suggested as causes for diminished mechanics [10,12–14,19–23]. First, the collagen backbone can be fragmented when the molecular bonds are cleaved directly by x- and gamma-rays, breaking the intact protein chain into smaller polypeptides. Second, collagen molecules can be non-enzymatically crosslinked when radiolysis of water molecules creates free radicals, which cause inter- and intra- molecular bonds within collagen chains. However, it remains unclear which mechanism is more causative and at what dose these mechanisms manifest. Because changes in collagen

[1] Abbreviations: Gy, Gray; N_f, Fatigue Life; ε_f, Strain-to-Failure; $K_{elastic}$, Elastic Stiffness; AGEs, Advanced Glycation End Products; FU, Fluorescence Unit;

structure are associated with a number of clinical conditions, an improved biomechanical understanding of each mechanism (i.e. non-enzymatic crosslinks and fragmentation) may provide insight into applications of irradiation [22], and also aging [24] and diabetes [25–28].

Addressing these issues, we conducted an *ex vivo* ionizing radiation experiment on mouse vertebrae spanning a range of clinically-related radiation doses (i.e. radiation therapy to allograft sterilization) and conducted a suite of mechanical and biochemical assays to assess radiation-induced changes. Specifically, our objectives were to: 1) quantify the effects of radiation dose on the monotonic strength and fatigue life of murine vertebrae; and 2) determine whether the degradation in mechanical properties is dominated by the amount of non-enzymatic crosslinks or fragmented collagen.

2 Materials and Methods

2.1 Animals

Forty-eight female, 20-week old (skeletally-mature) C57BL/6J mice (Jackson Labs, Sacramento, CA) were randomly assigned to five groups (N = 9–10 per group). Mice were euthanized prior to *ex vivo* irradiation. All procedures were approved by the University of California Berkeley Animal Care and Use Committee.

2.2 Specimen preparation

Lumbar vertebrae (L3, L4, L5, S1) were excised and gently cleaned of soft tissue, wrapped in saline-soaked gauze (Gibco PBS 1X, pH 7.4), and stored at -20°C. In preparation for mechanical testing, the vertebral bodies of the L4 and L5 levels were isolated, endplates precisely planed using a diamond microtome (Leica SP1600 Saw Microtome, Wetzlar, Germany) and posterior elements removed [29].

2.3 Ex Vivo X-Ray Irradiation

After specimen preparation, *ex vivo* irradiation was performed on all vertebrae. Mice were randomly assigned to one of five dose groups for x-ray irradiation: 0, 50, 1,000, 17,000, or 35,000 Gy; all

vertebral levels from the same animal remained in the same radiation dose group (e.g. an animal assigned to the 50 Gy group had its L3, L4, L5, and S1 irradiated with 50 Gy). Irradiation was performed (Advanced Light Source synchrotron facility at Lawrence Berkeley National Laboratory) using an x-ray synchrotron micro-tomography beam line, at 21 keV and 500 mA, for a dose rate of 13.3 Gy/sec (see [30] for details on dose calculations). Specimen hydration was maintained during irradiation via saline-soaked gauze.

2.4 Quantitative micro-CT Imaging

After irradiation, the L4 and L5 specimens were imaged with quantitative micro-CT (µCT 50, Scanco Medical AG, Bruttisellen, Switzerland) using a 10-µm voxel size (55 kV, 109 µA, 1000 projections per 180°, 500 ms integration time). Micro-CT images of the L4 and L5 specimens were analyzed for height (ImageJ 2.0, Java 1.6.0). The total bone volume of the vertebrae was measured on the L5 only (ImageJ 2.0, BoneJ2). After manual segmentation of the trabecular compartment, the following parameters were measured between the top and bottom surface of the L5 vertebra: trabecular bone volume fraction (Tb.BV/TV), number (Tb.N), thickness (Tb.Th), and separation (Tb.Sp) (Scanco Medical µCT Evaluation Program v6.5) [29]. The micro-CT analysis confirmed successful random sample distribution; there were no significant differences in bone quantity or microarchitecture between the groups.

2.5 Mechanical Characterization

After micro-CT imaging, uniaxial compressive monotonic (L4) and cyclic (L5) mechanical testing was performed (TA ElectroForce 3200, Eden Prairie, MN; 25 mm linear encoder "High Accuracy Displacement Sensor", resolution ±1 nm, accuracy ±25 µm). Monotonic testing was conducted (displacement rate of 0.01 mm/sec; strain rate ranged from 0.5 to 0.8% strain/s) to provide measurements of stiffness, strength (maximum force), ultimate strain (displacement at maximum force, divided by specimen height), and work-to-fracture (**Figure 1A**).

Cyclic testing was conducted using methods described in detail by Pendleton et al. [29]. In brief, in order to compare the fatigue life across all radiation dose groups, the fatigue test was designed such that

the same initial strains were applied to all samples [29]. Using micro-CT based finite element models of each specimen, we computationally derived the specimen-specific forces (F_{min} and F_{max}) required to achieve the desired initial strains (ε_{min} = 0.05% and ε_{max} = 0.5%) during cyclic testing. Thus, specimens were cyclically loaded in uniaxial compression between the specimen-specific F_{min} and F_{max} values until failure (TA ElectroForce 3200, Eden Prairie, MN; 50 lb. load cell, resolution ±0.1 N). Cyclic loading properties measured include fatigue life (N_f) (i.e. number of cycles to failure), strain-to-failure (ε_f), and specimen elastic stiffness ($K_{elastic}$) (**Figure 1B**). Cyclic testing was not performed for specimens where the calculated F_{max} exceeded the dose group strength observed from monotonic testing, as these specimens would have failed within one loading cycle (confirmed by testing a small sample; data not shown).

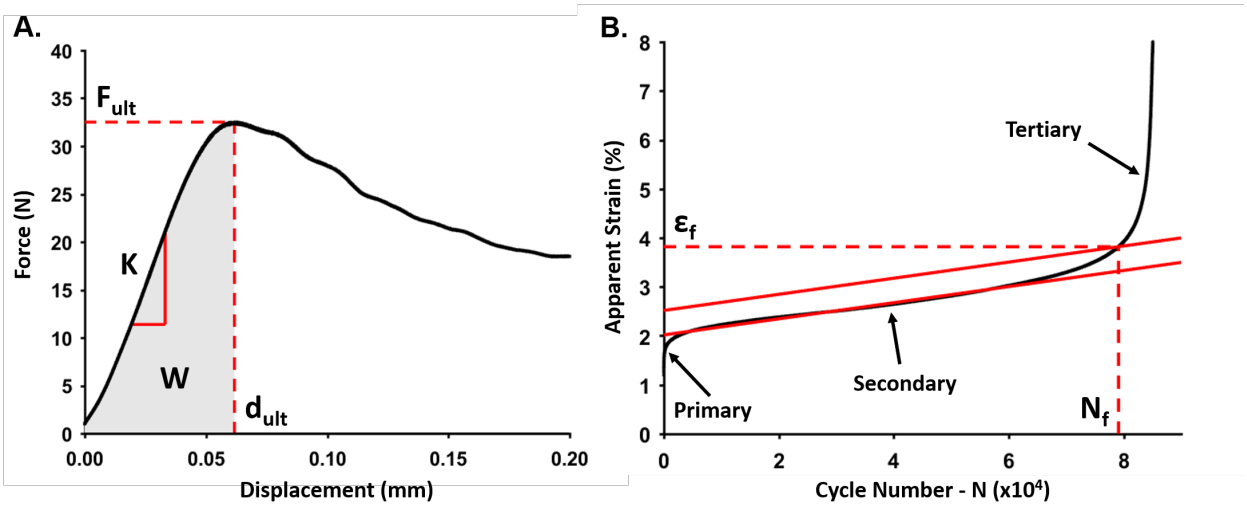

Figure 1: Representative plots generated from mechanical testing of the vertebral specimens. (**A**) For monotonic compression testing, a force-displacement curve was used to calculate stiffness (K), ultimate force (F_{ult}), ultimate displacement (d_{ult}), and work to fracture (W; area in gray). (**B**) For cyclic testing, maximum apparent strain per cycle was plotted to obtain fatigue life (N_f), strain-to-failure (ε_f), and elastic stiffness ($K_{elastic}$), see [29] for details.

2.6 Biochemical Characterization

After irradiation, two biochemical tests (N = 4 specimens for each test) were conducted to assess the two primary molecular mechanisms that are thought to alter bone mechanics: (1) the accumulation of non-enzymatic crosslinks was measured on the S1 vertebrae; (2) the fragmentation of the collagen backbone was quantified on the L3 vertebrae.

To assess non-enzymatic collagen crosslinking, we quantified the relative amount of fluorescent advanced glycation end-products (AGEs) on the S1 vertebrae. AGEs, which form intra- and inter-fibrillar crosslinks along the collagen backbone through oxidation or glycation processes [26,31–33], were quantified using a fluorometric assay (protocol adapted from Sell et al. [34]). Each S1 specimen was demineralized in 0.5 M ethylenediaminetetraacetic acid (EDTA) and hydrolyzed in 12N HCl at 120°C for 3 hours to break down peptide bonds. The hydrolysate was then resuspended in PBS (0.1X) and pipetted in triplicate onto a black-walled 96 well plate. The non-enzymatic collagen crosslink content was determined using fluorescence readings taken using a microplate reader at wavelengths of 370 nm excitation and 440 nm emission. The readings were standardized to a quinine-sulfate standard (quinine dissolved in H_2SO_4) and then normalized to the amount of collagen present in each sample, approximated by the amount of hydroxyproline [13,35]. The quantification of non-enzymatic collagen crosslinks was achieved via the fluorometric assay that determined the relative fluorescence due to advanced glycation end-products (AGEs) relative to the amount of collagen in the bone matrix. The relative amount of non-enzymatic collagen crosslinks (fluorescent AGEs) for each radiation group was compared to the control.

To assess collagen fragmentation, we used an automated electrophoresis assay (2100 Bioanalyzer, Agilent Technologies, Santa Clara, CA) to quantify the molecular weight distribution of collagen isolated from the L3 vertebrae. First, we isolated the collagen via methods adapted from Burton et al. [10] (see [30] for details). In brief, L3 specimens were demineralized over 3 weeks in 0.5M ethylenediaminetetraacetic acid (EDTA) with the solution changed every 2-3 days. Demineralized specimens were defatted for 24-hours in a 1:1 solution of chloroform and methanol and then soaked in 100% methanol for another hour. Specimens were dried in a desiccator overnight, and then flash-frozen with liquid-nitrogen and crushed into bone powder using a mortar and pestle. Bone powder was then lyophilized (Sequence: -38°C for 180 minutes, -38°C at 120 mTorr for 90 minutes, -20°C at 770 mTorr for 900 minutes, -10 °C at 930 mTorr for 270 minutes, and 23°C at 120 mTorr for 55 minutes) (VirTis AdVantage Plus Benchtop Freeze Dryer XL Model, SP Scientific, Stone Ridge, NY). For tissue digestion, the powder was added to a solution of 0.5M

acetic acid and pepsin (1mg of pepsin per 10 mg of bone powder) and placed on a rocker at 4°C for 72-hours. To neutralize the digestion process 5M NaOH was added until pH was neutral (pH = 6-8). To remove non-soluble collagen and non-collagenous proteins, samples were centrifuged for 30 minutes at 13,000 RPM. The supernatant, containing the soluble collagen, was collected. To precipitate the collagen out of solution, solid NaCl was added to a final concentration of 2M NaCl and placed on a rocker at 4°C for 24-hours. Samples were centrifuged for 30 minutes at 13,000 RPM. The supernatant was removed, and the pellets were resuspended in 200 uL of 0.5M acetic acid. Samples were then lyophilized and stored at -20°C until electrophoresis. In preparation for electrophoresis, the isolated collagen was dissolved in 1X PBS, mixed with additional reagents (Agilent Technologies Protein 230 Manual), and loaded on a bioanalyzer chip for automated electrophoresis. Rat-tail collagen (Sigma Aldrich, C7661-25MG) was run as a standard. From this assay, the distribution of molecular weights of the collagen protein was assessed in two ways: (1) visually with a software-generated "gel" and (2) quantitatively with a software-generated fluorescence unit (FU) chart, called an "electropherogram" (Agilent 2100 Expert software). The nominal size of a type-I collagen, either alpha-1 or alpha-2, is between 130-150 kDa. To identify chain fragmentation, we looked for evidence of less protein in this range, and a wider distribution of molecular weights. On the gel, this was observed as a lighter-colored band or smeared band at ~150 kDa. On the electropherogram, fragmentation can be observed when the peak at ~150 kDa is diminished, indicating fewer fluorescence units and therefore fewer collagen chains of the nominal size. The quantification of collagen fragmentation was achieved via the software-generated electropherogram by comparing the quantity of fluorescence units (FU) at the nominal collagen chain length (~150 kDa) for each radiation group to the control.

2.7 Statistics

We used a one-way ANOVA to test for radiation effects, followed by Dunnett's *post-hoc* test (at $p \leq 0.05$) to compare each group against the control (0 Gy) (JMP v 14.0, SAS Institute). For those measurements that were not normally distributed (ultimate strain), a Kruskal-Wallis test was conducted instead, followed by the Steel *post-hoc* to compare each group against the control (JMP v 14.0, SAS

Institute). In order to compare the magnitude of responses across the different measurements – vertebral strength, crosslink AGEs, and fragmentation fluorescence – each datum for the individual specimen was normalized by the mean value of that measurement for the control group. Then, the means of these normalized values for the crosslink AGEs and fragmentation fluorescence measurements were individually compared against the mean normalized value for vertebral strength, using a Student's t-test ($p \leq 0.05$) (JMP v 14.0, SAS Institute).

3 Results

3.1 Mechanical Characterization

For monotonic compression testing, the vertebral strength, ultimate strain, and work-to-fracture were lower than the control group for radiation exposures of 17,000 and 35,000 Gy but were not different than the control group for exposures of 50 and 1,000 Gy. Compared to the control group, for the exposures of 17,000 and 35,000 Gy, vertebral strength was 50% and 73% lower ($p < 0.001$, **Figure 2**), respectively, ultimate strain was 58% and 77% lower (Steel post-hoc $p < 0.05$, **Figure 2**), and work-to-fracture was 76% and 92% lower ($p < 0.01$, data not shown). In contrast, monotonic stiffness remained unchanged for all radiation dose groups compared to the control group (691.3 ± 179.5 N/mm; $p = 0.67$, **Figure 2**).

Similar trends, but more accentuated, were observed for the cyclic properties. Monotonic strength of 17,000 and 35,000 Gy groups were less than the prescribed cyclic loading force, F_{max}, and thus cyclic testing was not conducted for these two groups since the specimens would have fractured after one cycle of loading (confirmed by testing a small sample, data not shown). Fatigue life (5.2 ± 0.4 log(cycles); $p = 0.50$, **Figure 2**), strain to failure (3.8 ± 1.0 %; $p = 0.41$, data not shown), and elastic stiffness (1273 ± 162 N/mm; $p = 0.31$, data not shown) for the 50 and 1,000 Gy exposures did not differ from the control.

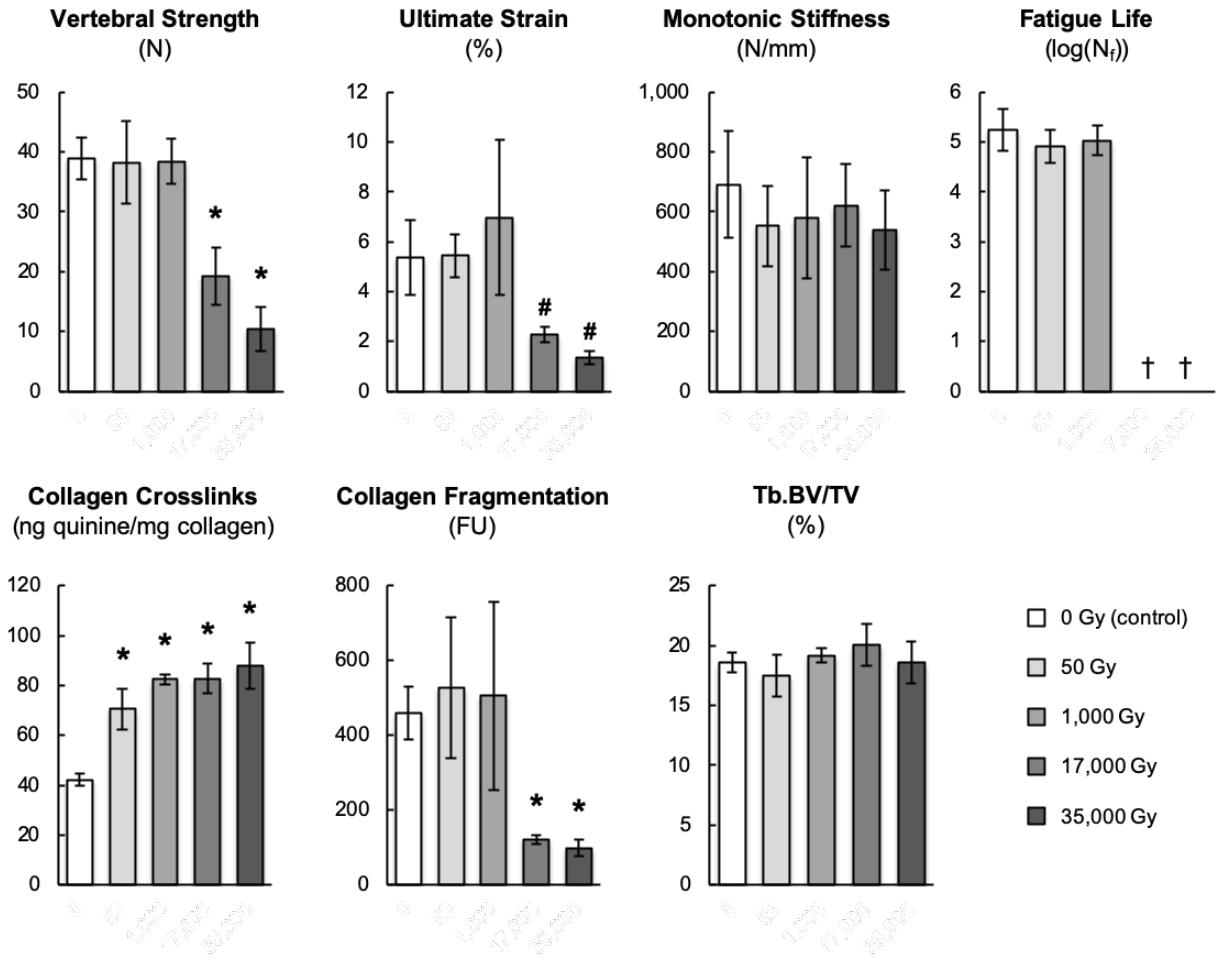

Figure 2: Effect of *ex vivo* x-ray radiation on mechanical (monotonic vertebral strength, ultimate strain and stiffness; cyclic fatigue life), biochemical (collagen crosslink AGEs and collagen fragmentation), and micro-CT (Tb.BV/TV) properties of mouse lumbar vertebrae. Data are shown as least-square means; error bars represent 95% confidence intervals. † indicates cycles to failure not measured. * $p < 0.05$ using Dunnett's post-hoc test; # $p < 0.05$ using Steel's post-hoc test.

3.2 Biochemical Characterization

The relative amount of non-enzymatic collagen crosslinks (fluorescent AGEs) was greater for all radiation groups by nearly twofold, and increased in a dose-dependent manner: by 67%, 95%, 96%, and 108% for 50, 1,000, 17,000 and 35,000 Gy, respectively, compared to the control (42.2 ± 2.3 ng quinine / mg collagen; $p < 0.001$, **Figure 2**).

In contrast, collagen fragmentation was only observed at doses of 17,000 and 35,000 Gy (**Figure 2**). Fragmentation at these doses was observed on both the software-generated gel (**Figure 3A)** and electropherogram (**Figure 3B**). On the gel, a dark band was visible at the nominal collagen chain length of 150 kDa for samples of 0, 50, and 1,000 Gy. This band began to lighten at 17,000 and 35,000 Gy, indicating fewer collagen proteins of this chain size. Also, a "smearing" of bands was observed below 150 kDa, suggesting that there was a greater amount of collagen fragmented chains with lower molecular weights. On the electropherogram, the same result can be observed. The peak fluorescence unit found at 150 kDa for 17,000 Gy decreased by 74% compared to the control (460 ± 72 FU; $p < 0.02$).

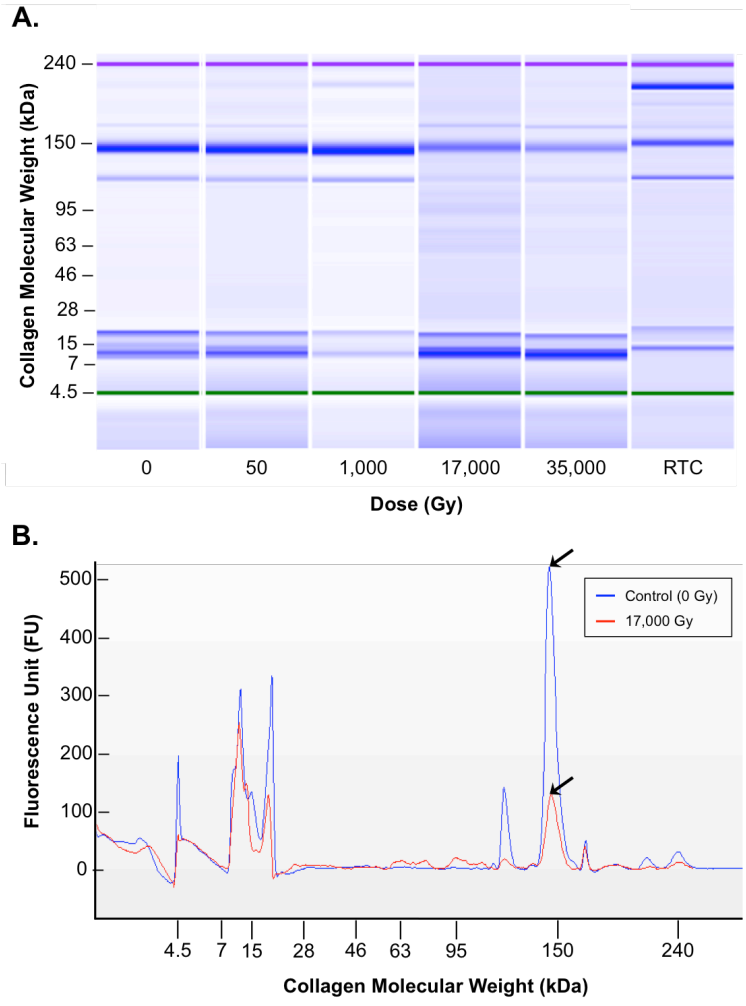

Figure 3: Output from the automated electrophoresis assay (collagen fragmentation). (**A**) A representative gel. (**B**) A representative electropherogram with the results of 0 and 17,000 Gy overlaid. The

peak fluorescence unit found at 150 kDa for 17,000 Gy (red) is significantly lower compared to the 0 Gy control (blue).

When comparing the magnitudes of the effects across the different (normalized) measurements, for all radiation doses, the normalized values were higher for crosslinking than for vertebral strength ($p < 0.01$) (**Figure 4**). By contrast, the normalized values for the unfragmented collagen chains were not different than for vertebral strength ($p > 0.55$), except at the 17,000 Gy dose, for which the difference was significant ($p = 0.03$) but small (vertebral strength 0.50 ± 0.06; fragmentation 0.26 ± 0.03) (**Figure 4**).

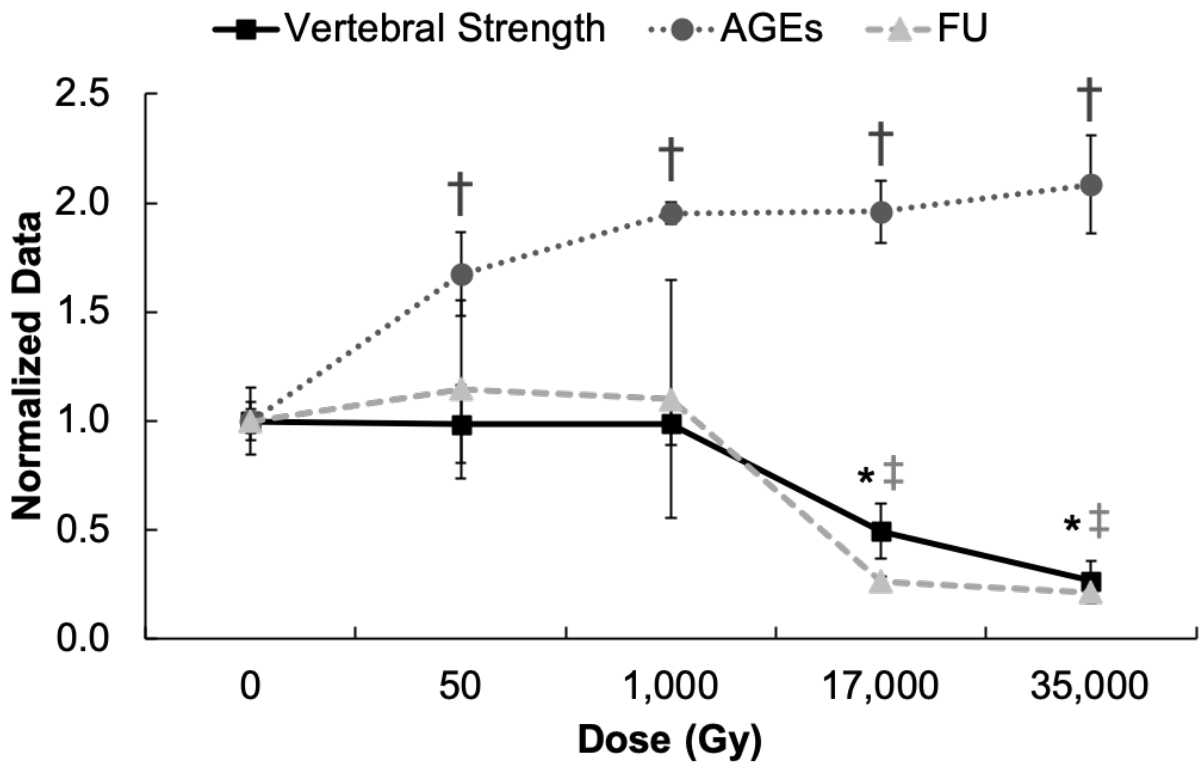

Figure 4: Comparison of vertebral strength with two primary mechanisms of collagen degradation: (1) collagen crosslinks represented by AGEs, and (2) collagen fragmentation indicated by a lower fluorescence unit (FU) value indicating less collagen with a nominal chain length, by radiation dose. Data were normalized by the mean of their respective 0 Gy control, and shown as normalized least-square means, with error bars signifying 95% confidence intervals analyzed by ANOVA with Dunnett's post-hoc test, $p < 0.05$. * represents $p < 0.0001$ for vertebral ultimate strength; † represents $p < 0.0001$ for AGEs; ‡ represents $p < 0.05$ for FU.

3.3 Quantitative micro-CT Imaging

The micro-CT analysis confirmed successful random sample distribution; there were no significant differences in bone quantity or microarchitecture between the groups. Total bone volume (1.41 ± 0.16 mm^3, $p = 0.71$, data not shown), as well as trabecular bone volume fraction (18.79 ± 0.94 %, $p = 0.20$, **Figure 2**), number (3.92 ± 0.13 1/mm, $p = 0.35$, data not shown), and separation (256.97 ± 8.81 µm, $p = 0.47$, data not shown) were the same for all groups. ANOVA results for trabecular thickness were significant ($p = 0.036$), however a Tukey post-hoc analysis found no differences between any groups (50.17 ± 68 µm, $p > 0.05$, data not shown).

4 Discussion

These results demonstrate that the monotonic strength of murine vertebral bodies was only diminished when exposed to ionizing radiation at or above 17,000 Gy. While the relative amount of non-enzymatic collagen crosslinks was greater for all radiation groups compared to the control, the increase in crosslinks measured at lower doses (50 and 1,000 Gy) did not coincide with the observed reduction in mechanical strength (**Figure 4**). In contrast to crosslinks, collagen fragmentation was only observed at doses where reduced mechanical properties were also observed (17,000 and 35,000 Gy; **Figure 4**). Thus, our results suggest that the fragmentation of collagen — and not the accumulation of non-enzymatic collagen crosslinks — was the primary molecular mechanism that caused the observed reductions in mechanical properties in whole bones exposed to ionizing radiation.

Our results are consistent with previous radiation studies, and provide novel insight into the effect of *ex vivo* ionizing radiation on bone mechanics. In accordance with previous investigations of cortical bone, we observed a reduction in both monotonic and fatigue properties at a dose equivalent to nominal allograft sterilization of ~30,000 ± 5,000 Gy [10,15,20,36–38], and a reduction of monotonic strength at 17,000 Gy [11]. While our study is consistent with earlier observations, our findings expand upon previous knowledge in three important areas. First, previous inquiries have been conducted on either cortical

[10,11,15,20,36–38] or trabecular [39] bone tissue specimens, not whole-bones. Second, mechanical characterization has been primarily conducted in either monotonic or fatigue loading conditions, not both. Finally, only a subset of these studies has conducted concurrent collagen biochemical analysis, quantifying either crosslinks [13] or fragmentation [10,36,38]. For the first time, we have demonstrated the effect of irradiation on whole-bones (with both cortical and trabecular tissue) across a spectrum of clinically-relevant doses (i.e. radiation therapy at 50 Gy to allograft sterilization at 35,000 Gy) with both monotonic and fatigue mechanical tests, as well as parallel collagen biochemical assays. We expand on the work of Currey et al. [11] and demonstrate that in addition to a reduction in monotonic strength following irradiation at 17,000 Gy, fatigue properties are also significantly reduced. Importantly, we have demonstrated the doses at which the differences in collagen structure and mechanics arise. Our results provide new insight into the type of molecular change driving the degradation of whole-bone strength and fatigue life following irradiation.

While the exact collagen modifications dominating reduced strength following irradiation are not fully understood, we examined the two proposed mechanisms: photon-induced fragmentation of the collagen backbone [10,20] or radiolysis-induced non-enzymatic collagen crosslinks [12,13,21–23]. Our results suggest that increased collagen fragmentation, and not non-enzymatic crosslinking, is the dominant factor. While no previous studies have quantified the fragmentation of collagen in irradiated whole-bones, our results are in agreement with previous work on cortical bone, which demonstrated that diminished fracture toughness at doses of ~35,000 Gy was a result of collagen fragmentation [10,36]. Expanding on this knowledge, we demonstrate that collagen fragmentation leads to degraded murine whole-bone mechanics at 17,000 Gy, a dose signifiantly lower than the standard for allograft sterilization (25,000 – 35,000 Gy). Our findings emphasize the need for further research into novel radioprotectants that target fragmentation in order to maintain bone strength when sterilizing allografts with radiation [10].

Importantly, our findings suggest that non-enzymatic collagen crosslinks may play a smaller role in degrading mechanical strength of bone than previously considered. Previously, numerous studies attributed the increase in non-enzymatic crosslink concentration as the primary mechanism for degraded

bone strength, specifically in applications of natural aging [24,35,40], drug treatments [41], irradiation sterilization [13], and diseases such as osteoporosis [42] and diabetes [26,43–46]. While the concentration of non-enzymatic crosslinks does accumulate in bone collagen in these applications, any causation of those crosslinks with respect to degraded mechanical properties has not been established. Here, we observed that despite a substantial (95%) increase in crosslink concentration, we could not detect any effect on vertebral strength. Indeed, studies have demonstrated that an increase in non-enzymatic crosslinks induced via ribose incubation can be used to counter the loss of strength due to the fragmentation of the collagen network, not degrade it further [38,47,48]. Taken together, our results strengthen the argument that the contribution of non-enzymatic crosslinks to diminished bone strength with disease and aging plays a smaller role in comparison to other factors, such as collagen network connectivity [49].

There are some limitations in this study. First, because we tested mouse bone, the direct application of our findings to human bone is unclear. However, as discussed above, similar trends in irradiation-induced degraded bone strength [10,11,53,54,15,20,36–38,50–52] and molecular-level changes [10,52] have been seen in other studies across a number of anatomic sites and species, including human bone. That consistency suggests our results are not limited to murine bone. Second, as an *ex vivo* study, we excluded the impact of any biologically induced responses to radiation in order to explore the extent to which radiation directly alters the mechanical behavior of the bone matrix. For applications of allograft sterilization, which are only conducted *ex vivo*, excluding cellular effects is appropriate. However, for *in vivo* applications of radiation therapy, there can be cellular-driven changes, such as reduced bone volume fraction or altered trabecular microarchitecture [49], which can alter bone mechanics beyond what is reported here. Additionally, we performed all mechanical tests, monotonic and cyclic, in compression. While compressive loading is most relevant for *in vivo* behavior, the response may be different for isolated specimens tested in pure tension.

Finally, because our study did not investigate doses between 1,000 and 17,000 Gy, it is unclear at what dose within this range reduced mechanical properties can first be observed. To address this gap, we conducted a post-hoc study for doses of 5,000 and 10,000 Gy (see Appendix) with the same mechanical

and biochemical assays described above. We found some mechanical differences occurred with radiation exposure of 5,000 Gy (and above), but only for cyclic loading: compared to the control, fatigue life was lower by 18% ($p < 0.01$) but monotonic strength was not different ($p = 0.12$). These ad hoc results confirm previous observations that cyclic loading may be a more sensitive test than monotonic loading for detecting mechanical effects of radiation [13,20]. Clinically, radiation-induced fractures are often observed months to years after irradiation and classified as spontaneous or insufficiency fractures (i.e. fractures which are not the result of a fall or trauma, and more likely due to repetitive loading at low forces over time) [55–57]. As such, it is clinically important to consider mechanisms that can affect cyclic loading properties differently than static loading properties. Furthermore, our findings have expanded our knowledge to show fatigue properties are also significantly reduced with doses as low as 5,000 Gy.

Clinically, our results have implications for safe sterilization of allografts and potential radioprotectants. A dose of 11,000 Gy has been proposed as a safe sterilization dose for allografts [58], as this dose achieves the same sterility level as the current standard dose of 30,000 ± 5,000 Gy [4,5]. However, our supplemental findings suggest collagen fragmentation and associated loss of cyclic mechanical properties can begin with a dose as low as 5,000 Gy (see Appendix). To mitigate the loss of mechanical integrity, further studies are needed to investigate how to safeguard the bone with a radioprotectant. Several radioprotectants have been considered for their ability to preserve tissue properties following irradiation [4,48,59]. Based on our results, we would recommend studies focused on radioprotectants which can prevent or offset the fragmentation of collagen, as these types of radioprotectants may preserve bone mechanics to a greater degree than those which protect against non-enzymatic collagen crosslinks.

Our results also have implications for understanding the etiology of the increased fracture risk associated with *in vivo* radiation therapy treatment for cancer [2,8,60–65]. We did not observe any change in mechanical behavior for *ex vivo* dose levels relevant to radiation therapy (i.e. 50 Gy), despite an increase in collagen crosslinks. Thus, direct effects of radiation on the collagen matrix from radiation therapy are not solely responsible for the increased fracture risk observed clinically. From this, we can infer that the

cellular processes of bone remodeling due to *in vivo* irradiation are likely the root cause. Indeed, previous *in vivo* irradiation studies of bone in a murine model have shown reduced trabecular bone mass, number and connectivity associated with hyperactive osteoclast activity [66–68]. Taken together with our *ex vivo* observations, cell-mediated changes in bone quantity, trabecular microarchitecture, or tissue material quality are more plausible explanations for the increased fracture risk from radiation therapy than direct changes to the bone material.

In summary, we quantified the level of collagen fragmentation and non-enzymatic collagen crosslinks in the organic matrix of murine whole-bones at clinically-relevant *ex vivo* radiation doses. Our results suggest that the fragmentation of collagen — and not the accumulation of non-enzymatic collagen crosslinks — was the primary molecular mechanism that caused the observed monotonic mechanical degradation at 17,000 Gy and above, and cyclic mechanical degradation at 5,000 Gy and above.

Disclosures

TMK: Consultant for Amgen, AgNovos Healthcare, and O.N. Diagnostics; equity in O.N. Diagnostics.

Conflict of Interest

All authors certify that there are no conflicts of interest related to the work presented in this manuscript.

Acknowledgements

This study was supported by NASA Science & Technology Research Fellowship NNX14AM56H (MMP), National Science Foundation Graduate Research Fellowship Program #1752814 (SRE), a NASA Space Biology PECASE (JSA), and grants from the National Institutes of Health (K01AR069116, R21AR069804, R01AR07444) (SYT). This research used resources of the Advanced Light Source, which is a DOE Office of Science User Facility under contract No. DE-AC02-05CH11231. Computational

resources were made available through the National Science Foundation via XSEDE, Grant TG-MCA00N019 (TMK). The authors would like to thank Saghi Sadoughi (UCB) for her assistance with finite element modeling, Alfred Li (UCSF) for his micro-CT expertise, Dula Parkinson (LBNL) for his support with the irradiation protocol, and Tamara Alliston (UCSF), Thomas Willet (University of Waterloo), and Elumalai Rangasamy (Agilent Technologies) for their guidance on the biochemical assays.

5 Appendix: Supplemental Study

To gain insight into the effect of ionizing radiation between 1,000 and 17,000 Gy, we conducted an additional *ex vivo* x-ray radiation experiment on excised mouse lumbar vertebrae from 20-week old, female, C57BL/6J mice, randomly assigned to a one-time *ex vivo* radiation dose of either 0 (n = 4), 5,000 (n = 5), or 10,000 Gy (n = 5). As detailed above, we measured mechanical properties, collagen crosslinks, and collagen fragmentation (data not shown). We observed compressive fatigue life to be lower for the irradiated groups, being 18% ($p < 0.01$) and 37% ($p < 0.0001$) lower for 5,000 and 10,000 Gy doses, respectively, compared to the control (5.0 ± 0.4 log(cycles)). We detected no significant effect of radiation dose for any of the compressive monotonic mechanical properties, either for strength ($p = 0.12$), stiffness ($p = 0.62$), or maximum displacement ($p = 0.51$). Collagen crosslinks increased significantly for all irradiated groups, by 71% and 101% for 5,000 and 10,000 Gy, respectively ($p < 0.05$). Collagen fragmentation was evident for 5,000 Gy, observed as a significant decrease in the amount of nominally sized collagen chains (~150 kDa) compared to the 0 Gy control ($p = 0.008$); data for the 10,000 Gy group was lost due to a processing error. These findings suggest that doses well below sterilization standards (30,000 ± 5,000 Gy) and a proposed alternative (11,000 Gy) may compromise the mechanical strength and collagen integrity of bone allografts, making them more susceptible to failure under cyclic loading [4,5,58].

6 References

[1] A.J. Meixel, H. Hauswald, S. Delorme, B. Jobke, From radiation osteitis to osteoradionecrosis: incidence and MR morphology of radiation-induced sacral pathologies following pelvic radiotherapy, Eur. Radiol. 28 (2018) 3550–3559. doi:10.1007/s00330-018-5325-2.

[2] R.L. Wei, B.C. Jung, W. Manzano, V. Sehgal, S.J. Klempner, S.P. Lee, N.S. Ramsinghani, C. Lall, Bone mineral density loss in thoracic and lumbar vertebrae following radiation for abdominal cancers, Radiother. Oncol. 118 (2016) 430–436. doi:10.1016/j.radonc.2016.03.002.

[3] K.K. Shih, M.R. Folkert, M.A. Kollmeier, N.R. Abu-Rustum, Y. Sonoda, M.M. Leitao, R.R. Barakat, K.M. Alektiar, Pelvic insufficiency fractures in patients with cervical and endometrial cancer treated with postoperative pelvic radiation, Gynecol. Oncol. 128 (2013) 540–543. doi:10.1016/j.ygyno.2012.12.021.

[4] R. Singh, D. Singh, A. Singh, Radiation sterilization of tissue allografts: A review, World J. Radiol. 8 (2016) 355. doi:10.4329/wjr.v8.i4.355.

[5] D.G. Campbell, P. Li, A.J. Stephenson, R.D. Oakeshott, Sterilization of HIV by gamma irradiation. A bone allograft model., Int. Orthop. 18 (1994) 172–6. http://www.ncbi.nlm.nih.gov/pubmed/7927967.

[6] C. Okoukoni, M. Farris, R.T. Hughes, E.R. McTyre, C.A. Helis, M.T. Munley, J.S. Willey, Radiation-Induced Bone Toxicity, Curr. Stem Cell Reports. 3 (2017) 333–341. doi:10.1007/s40778-017-0099-z.

[7] L. Bazire, H. Xu, J.P. Foy, M. Amessis, C. Malhaire, K. Cao, A. De La Rochefordiere, Y.M. Kirova, Pelvic insufficiency fracture (PIF) incidence in patients treated with intensity-modulated radiation therapy (IMRT) for gynaecological or anal cancer: Single-institution experience and review of the

literature, Br. J. Radiol. 90 (2017). doi:10.1259/bjr.20160885.

[8] N.N. Baxter, E.B. Habermann, J.E. Tepper, S.B. Durham, B.A. Virnig, Risk of pelvic fractures in older women following pelvic irradiation, JAMA. 294 (2005) 2587–2593. doi:10.1001/jama.294.20.2587.

[9] S.A. Lietman, W.W. Tomford, M.C. Gebhardt, D.S. Springfield, H.J. Mankin, Complications of irradiated allografts in orthopaedic tumor surgery., Clin. Orthop. Relat. Res. 2000 (2000) 214–217. doi:10.1097/00003086-200006000-00026.

[10] B. Burton, A. Gaspar, D. Josey, J. Tupy, M.D. Grynpas, T.L. Willett, Bone embrittlement and collagen modifications due to high-dose gamma-irradiation sterilization., Bone. 61 (2014) 71–81. doi:10.1016/j.bone.2014.01.006.

[11] J.D. Currey, J. Foreman, I. Laketic, J. Mitchell, D.E. Pegg, G.C. Reilly, Effects of ionizing radiation on the mechanical properties of human bone, J. Orthop. Res. 15 (1997) 111–117. doi:10.1002/jor.1100150116.

[12] H.D. Barth, M.E. Launey, A.A. MacDowell, J.W. Ager, R.O. Ritchie, On the effect of X-ray irradiation on the deformation and fracture behavior of human cortical bone, Bone. 46 (2010) 1475–1485. doi:10.1016/j.bone.2010.02.025.

[13] H.D. Barth, E.A. Zimmermann, E. Schaible, S.Y. Tang, T. Alliston, R.O. Ritchie, Characterization of the effects of x-ray irradiation on the hierarchical structure and mechanical properties of human cortical bone, Biomaterials. 32 (2011) 8892–8904. doi:10.1016/j.biomaterials.2011.08.013.

[14] H. Nguyen, D.A.F. Morgan, M.R. Forwood, Sterilization of allograft bone: Effects of gamma irradiation on allograft biology and biomechanics, Cell Tissue Bank. 8 (2007) 93–105. doi:10.1007/s10561-006-9020-1.

[15] O. Akkus, C.M. Rimnac, Fracture resistance of gamma radiation sterilized cortical bone allografts,

J. Orthop. Res. 19 (2001) 927–934. doi:10.1016/S0736-0266(01)00004-3.

[16] P. Zioupos, J.D. Currey, A.J. Hamer, The role of collagen in the declining mechanical properties of aging human cortical bone, J. Biomed. Mater. Res. 45 (1999). doi:10.1002/(SICI)1097-4636(199905)45:2<108::AID-JBM5>3.0.CO;2-A.

[17] J.S. Nyman, M. Reyes, X. Wang, Effect of ultrastructural changes on the toughness of bone, Micron. 36 (2005) 566–582. doi:10.1016/j.micron.2005.07.004.

[18] A.H. Burstein, J.M. Zika, K.G. Heiple, L. Klein, Contribution of collagen and mineral to the elastic-plastic properties of bone., J. Bone Joint Surg. Am. 57 (1975) 956–961.

[19] A. Colwell, A. Hamer, A. Blumsohn, R. Eastell, To determine the effects of ultraviolet light, natural light and ionizing radiation on pyridinium cross-links in bone and urine using high-performance liquid chromatography, Eur. J. Clin. Invest. 26 (1996) 1107–1114. doi:10.1046/j.1365-2362.1996.460602.x.

[20] O. Akkus, R.M. Belaney, Sterilization by gamma radiation impairs the tensile fatigue life of cortical bone by two orders of magnitude, J. Orthop. Res. 23 (2005) 1054–1058. doi:10.1016/j.orthres.2005.03.003.

[21] M.E. Oest, B. Gong, K. Esmonde-White, K.A. Mann, N.D. Zimmerman, T.A. Damron, M.D. Morris, Parathyroid hormone attenuates radiation-induced increases in collagen crosslink ratio at periosteal surfaces of mouse tibia, Bone. 86 (2016) 91–97. doi:10.1016/j.bone.2016.03.003.

[22] B. Gong, M.E. Oest, K.A. Mann, T.A. Damron, M.D. Morris, Raman spectroscopy demonstrates prolonged alteration of bone chemical composition following extremity localized irradiation, Bone. 57 (2013) 252–258. doi:10.1016/j.bone.2013.08.014.

[23] A.J. Bailey, D.N. Rhodes, C.W. Cater, Irradiation-Induced Crosslinking of Collagen, Radiat. Res. 22 (1964) 606–21. http://www.ncbi.nlm.nih.gov/pubmed/14201872.

[24] E.A. Zimmermann, E. Schaible, H. Bale, H.D. Barth, S.Y. Tang, P. Reichert, B. Busse, T. Alliston, J.W. Ager, R.O. Ritchie, Age-related changes in the plasticity and toughness of human cortical bone at multiple length scales, Proc. Natl. Acad. Sci. 108 (2011) 14416–14421. doi:10.1073/pnas.1209596109.

[25] M. Saito, K. Marumo, Effects of Collagen Crosslinking on Bone Material Properties in Health and Disease, Calcif. Tissue Int. 97 (2015) 242–261. doi:10.1007/s00223-015-9985-5.

[26] L. Karim, M.L. Bouxsein, Effect of type 2 diabetes-related non-enzymatic glycation on bone biomechanical properties, Bone. 82 (2016) 21–27. doi:10.1016/j.bone.2015.07.028.

[27] C. Acevedo, M. Sylvia, E. Schaible, J.L. Graham, K.L. Stanhope, L.N. Metz, B. Gludovatz, A. V. Schwartz, R.O. Ritchie, T.N. Alliston, P.J. Havel, A.J. Fields, Contributions of Material Properties and Structure to Increased Bone Fragility for a Given Bone Mass in the UCD-T2DM Rat Model of Type 2 Diabetes, J. Bone Miner. Res. 33 (2018) 1066–1075. doi:10.1002/jbmr.3393.

[28] D. Farlay, L. Armas, E. Gineyts, M. Akhter, R. Recker, G. Boivin, Non-enzymatic glycation and degree of mineralization are higher in bone from fractured patients with Type 1 Diabetes Mellitus, J. Bone Miner. Res. 31 (2016) 190–195. doi:10.1002/jbmr.2607.Non-enzymatic.

[29] M.M. Pendleton, S. Sadoughi, A. Li, G.D. O'Connell, J.S. Alwood, T.M. Keaveny, High-precision method for cyclic loading of small-animal vertebrae to assess bone quality, Bone Reports. 9 (2018) 165–172. doi:10.1016/j.bonr.2018.10.002.

[30] M.M. Pendleton, Effects of Spaceflight- and Clinically-relevant Ionizing Radiation Exposure on Bone Biomechanics, University of California, Berkeley, 2018.

[31] L. Knott, A.J. Bailey, Collagen cross-links in mineralizing tissues: A review of their chemistry, function, and clinical relevance, Bone. 22 (1998) 181–187. doi:10.1016/S8756-3282(97)00279-2.

[32] D.B. Burr, Changes in bone matrix properties with aging, Bone. 120 (2019) 85–93.

doi:10.1016/j.bone.2018.10.010.

[33] A.J. Bailey, Molecular mechanisms of ageing in connective tissues, Mech. Ageing Dev. 122 (2001) 735–755. doi:10.1016/S0047-6374(01)00225-1.

[34] D.R. Sell, V.M. Monnier, Isolation, purification and partial characterization of novel fluorophores from aging human insoluble collagen-rich tissue, Connect. Tissue Res. 19 (1989) 77–92. doi:10.3109/03008208909016816.

[35] S.Y. Tang, U. Zeenath, D. Vashishth, Effects of non-enzymatic glycation on cancellous bone fragility, Bone. 40 (2007) 1144–1151. doi:10.1016/j.bone.2006.12.056.

[36] O. Akkus, R.M. Belaney, P. Das, Free radical scavenging alleviates the biomechanical impairment of gamma radiation sterilized bone tissue, J. Orthop. Res. 23 (2005) 838–845. doi:10.1016/j.orthres.2005.01.007.

[37] A. Islam, K. Chapin, E. Moore, J. Ford, C. Rimnac, O. Akkus, Gamma Radiation Sterilization Reduces the High-cycle Fatigue Life of Allograft Bone, Clin. Orthop. Relat. Res. 474 (2016) 827–835. doi:10.1007/s11999-015-4589-y.

[38] T.L. Willett, B. Burton, M. Woodside, Z. Wang, A. Gaspar, T. Attia, γ-Irradiation sterilized bone strengthened and toughened by ribose pre-treatment, J. Mech. Behav. Biomed. Mater. 44 (2015) 147–155. doi:10.1016/j.jmbbm.2015.01.003.

[39] M.J. Anderson, J.H. Keyak, H.B. Skinner, Compressive mechanical properties of human cancellous bone after gamma irradiation, J. Bone Jt. Surg. 74 (1992) 747–752. http://dx.doi.org/.

[40] J.S. Nyman, A. Roy, R.L. Acuna, H.J. Gayle, M.J. Reyes, J.H. Tyler, D.D. Dean, X. Wang, Age-related effect on the concentration of collagen crosslinks in human osteonal and interstitial bone tissue, Bone. 39 (2006) 1210–1217. doi:10.1016/j.bone.2006.06.026.

[41] S.Y. Tang, M.R. Allen, R. Phipps, D.B. Burr, D. Vashishth, Changes in non-enzymatic glycation

and its association with altered mechanical properties following 1-year treatment with risedronate or alendronate, Osteoporos. Int. 20 (2009) 887–894. doi:10.1007/s00198-008-0754-4.

[42] M. Saito, K. Fujii, S. Soshi, T. Tanaka, Reductions in degree of mineralization and enzymatic collagen cross-links and increases in glycation-induced pentosidine in the femoral neck cortex in cases of femoral neck fracture, Osteoporos. Int. 17 (2006) 986–995. doi:10.1007/s00198-006-0087-0.

[43] M. Janghorbani, R.M. Van Dam, W.C. Willett, F.B. Hu, Systematic review of type 1 and type 2 diabetes mellitus and risk of fracture, Am. J. Epidemiol. 166 (2007) 495–505. doi:10.1093/aje/kwm106.

[44] J.N. Farr, S. Khosla, Determinants of bone strength and quality in diabetes mellitus in humans, Bone. 82 (2016) 28–34. doi:10.1016/j.bone.2015.07.027.

[45] M.R. Rubin, J.M. Patsch, Assessment of bone turnover and bone quality in type 2 diabetic bone disease: current concepts and future directions., Bone Res. 4 (2016) 16001. doi:10.1038/boneres.2016.1.

[46] P. Vestergaard, Discrepancies in bone mineral density and fracture risk in patients with type 1 and type 2 diabetes--a meta-analysis., Osteoporos. Int. 18 (2007) 427–44. doi:10.1007/s00198-006-0253-4.

[47] M. Woodside, T.L. Willett, Elastic–plastic fracture toughness and rising JR-curve behavior of cortical bone is partially protected from irradiation–sterilization-induced degradation by ribose protectant, J. Mech. Behav. Biomed. Mater. 64 (2016) 53–64. doi:10.1016/j.jmbbm.2016.07.001.

[48] T. Attia, M. Woodside, G. Minhas, X.Z. Lu, D.S. Josey, T. Burrow, M. Grynpas, T.L. Willett, Development of a novel method for the strengthening and toughening of irradiation-sterilized bone allografts, Cell Tissue Bank. 18 (2017) 323–334. doi:10.1007/s10561-017-9634-5.

[49] T.L. Willett, D.Y. Dapaah, S. Uppuganti, M. Granke, J.S. Nyman, Bone collagen network integrity and transverse fracture toughness of human cortical bone, Bone. 120 (2019) 187–193. doi:10.1016/j.bone.2018.10.024.

[50] A.J. Hamer, J.R. Strachan, M.M. Black, C.J. Ibbotson, I. Stockley, R.A. Elson, BIOMECHANICAL PROPERTIES OF CORTICAL ALLOGRAFT BONE USING A NEW METHOD OF BONE STRENGTH MEASUREMENT, J. Bone Joint Surg. Br. 78-B (1996) 363–368. doi:10.1302/0301-620X.78B3.0780363.

[51] O. Cornu, X. Banse, P.-L. Docquier, S. Luyckx, C.H. Delloye, Synergetic effect of freeze-drying and gamma irradiation on the mechanical properties of human cancellous bone, J. Ortho. 18 (2000) 426–431. doi:10.1007/s10561-010-9209-1.

[52] N. Russell, A. Rives, N. Bertollo, M.H. Pelletier, W.R. Walsh, The effect of sterilization on the dynamic mechanical properties of paired rabbit cortical bone, J. Biomech. 46 (2013) 1670–1675. doi:10.1016/j.jbiomech.2013.04.006.

[53] K. Tüfekci, R. Kayacan, C. Kurbanoğlu, Effects of gamma radiation sterilization and strain rate on compressive behavior of equine cortical bone, J. Mech. Behav. Biomed. Mater. 34 (2014) 231–242. doi:10.1016/j.jmbbm.2014.02.004.

[54] E.J. Mitchell, A.M. Stawarz, R. Kayacan, C.M. Rimnac, The effect of gamma radiation sterilization on the fatigue crack propagation resistance of human cortical bone, J. Bone Jt. Surg. - Ser. A. 86 (2004) 2648–2657. doi:10.2106/00004623-200412000-00010.

[55] M. Overgaard, Spontaneous radiation-induced rib fractures in breast cancer patients treated with postmastectomy irradiation-a clinical radiobiological analysis of the influence of fraction size and dose-response relationships on late bone damage, Acta Oncol. (Madr). 27 (1988) 117–122. doi:10.3109/02841868809090331.

[56] D. Oh, S.J. Huh, Insufficiency fracture after radiation therapy, Radiat. Oncol. J. 32 (2014) 213–220. doi:10.3857/roj.2014.32.4.213.

[57] T. Shimoyama, H. Katagiri, H. Harada, H. Murata, J. Wasa, S. Hosaka, T. Suzuki, M. Takahashi, H. Asakura, T. Nishimura, H. Yamada, Fracture after radiation therapy for femoral metastasis: Incidence, timing and clinical features, J. Radiat. Res. 58 (2017) 661–668. doi:10.1093/jrr/rrx038.

[58] H. Nguyen, D.A.F. Morgan, M.R. Forwood, Validation of 11 kGy as a Radiation Sterilization Dose for Frozen Bone Allografts, J. Arthroplasty. 26 (2011) 303–308. doi:10.1016/j.arth.2010.03.032.

[59] F. Allaveisi, B. Hashemi, S.M.J. Mortazavi, Radioprotective effect of N-acetyl-L-cysteine free radical scavenger on compressive mechanical properties of the gamma sterilized cortical bone of bovine femur, Cell Tissue Bank. 16 (2015) 97–108. doi:10.1007/s10561-014-9446-9.

[60] G. Yaprak, C. Gemici, S. Temizkan, S. Ozdemir, B.C. Dogan, O.O. Seseogullari, Osteoporosis development and vertebral fractures after abdominal irradiation in patients with gastric cancer., BMC Cancer. 18 (2018) 972. doi:10.1186/s12885-018-4899-z.

[61] S.P. Elliott, S.L. Jarosek, S.R. Alanee, B.R. Konety, K.E. Dusenbery, B.A. Virnig, Three-dimensional external beam radiotherapy for prostate cancer increases the risk of hip fracture, Cancer. 117 (2011) 4557–4565. doi:10.1002/cncr.25994.

[62] K.M. Schmeler, A. Jhingran, R.B. Iyer, C.C. Sun, P.J. Eifel, P.T. Soliman, P.T. Ramirez, M. Frumovitz, D.C. Bodurka, A.K. Sood, Pelvic fractures after radiotherapy for cervical cancer: Implications for survivors, Cancer. 116 (2010) 625–630. doi:10.1002/cncr.24811.

[63] H. Uezono, K. Tsujino, K. Moriki, F. Nagano, Y. Ota, R. Sasaki, T. Soejima, Pelvic insufficiency fracture after definitive radiotherapy for uterine cervical cancer: retrospective analysis of risk factors, J. Radiat. Res. 54 (2013) 1102–1109. doi:10.1093/jrr/rrt055.

[64] S.K. Hui, L. Arentsen, A. Wilcox, R. Shanley, D. Yee, R. Ghebre, Spatial and temporal fracture

pattern in breast and gynecologic cancer survivors, J. Cancer. 6 (2015) 66–69. doi:10.7150/jca.10288.

[65] K. Otani, T. Teshima, Y. Ito, Y. Kawaguchi, K. Konishi, H. Takahashi, H. Ohigashi, K. Oshima, N. Araki, K. Nishiyama, O. Ishikawa, Risk factors for vertebral compression fractures in preoperative chemoradiotherapy with gemcitabine for pancreatic cancer, Radiother. Oncol. 118 (2016) 424–429. doi:10.1016/j.radonc.2016.01.006.

[66] M.E. Oest, C.G. Policastro, K.A. Mann, N.D. Zimmerman, T.A. Damron, Longitudinal Effects of Single Hindlimb Radiation Therapy on Bone Strength and Morphology at Local and Contralateral Sites, J. Bone Miner. Res. 33 (2018) 99–112. doi:10.1002/jbmr.3289.

[67] H. Kondo, N.D. Searby, R. Mojarrab, J. Phillips, J.S. Alwood, K. Yumoto, E.A.C. Almeida, C.L. Limoli, R.K. Globus, Total-body irradiation of postpubertal mice with (137)Cs acutely compromises the microarchitecture of cancellous bone and increases osteoclasts., Radiat. Res. 171 (2009) 283–289. doi:10.1667/RR1463.1.

[68] J.S. Willey, S.A.J. Lloyd, G.A. Nelson, T.A. Bateman, Ionizing radiation and bone loss: Space exploration and clinical therapy applications, Clin. Rev. Bone Miner. Metab. 9 (2011) 54–62. doi:10.1007/s12018-011-9092-8.

A new analytical approach to characterize the effect of γ-ray sterilization on wood

Claudia Mazzuca, Marilena Carbone, Rocco Cancelliere, Silvia Prati, Giorgia Sciutto, Rocco Mazzeo, Laura Tositti, Roberto Regazzi, Domiziano Mostacci, Laura Micheli

PII: S0026-265X(18)30501-0
DOI: doi:10.1016/j.microc.2018.08.001
Reference: MICROC 3285

To appear in: *Microchemical Journal*

Received date: 26 April 2018
Revised date: 31 July 2018
Accepted date: 1 August 2018

Please cite this article as: Claudia Mazzuca, Marilena Carbone, Rocco Cancelliere, Silvia Prati, Giorgia Sciutto, Rocco Mazzeo, Laura Tositti, Roberto Regazzi, Domiziano Mostacci, Laura Micheli , A new analytical approach to characterize the effect of γ-ray sterilization on wood. Microc (2018), doi:10.1016/j.microc.2018.08.001

A NEW ANALYTICAL APPROACH TO CHARACTERIZE THE EFFECT OF γ-RAY STERILISATION ON WOOD

Claudia Mazzuca[1,3], Marilena Carbone[1,2], Rocco Cancelliere[1], Silvia Prati[4], Giorgia Sciutto[4], Rocco Mazzeo[4], Laura Tositti[5], Roberto Regazzi[6], Domiziano Mostacci[6], Laura Micheli[*1,2,3]

[1]Department of Chemical Sciences and Technologies, University of Rome "Tor Vergata" Via della Ricerca Scientifica, 00133 Rome, Italy
[2] Consorzio Interuniversitario Biostrutture e Biosistemi "INBB", Viale Medaglie d'Oro 305, 00136 Rome, Italy
[3]CSGI, Center for Colloid and Surface Science (University of Rome "Tor Vergata" Unit), University of Florence, via della Lastruccia 3, Sesto Fiorentino, 50019 Florence, Italy
[4]Microchemistry and Microscopy Art Diagnostic Laboratory (M2ADL), Department of Chemistry, University of Bologna - Ravenna Campus, via Guaccimanni 42, 48100 Ravenna, Italy
[5]Environmental and Radioactivity Lab, Department of Chemistry "G. Ciamician", University of Bologna, via Selmi 2, 40126, Bologna, Italy
[6]Nuclear Engineering Laboratory, Department of Industrial Engineering, University of Bologna, Via dei Colli 16, 40136 Bologna, Italy

Abstract

Irradiation with γ rays is widely used in the sterilization of a large variety of products and materials in the field of medical supplies, pharmaceuticals, cosmetics, food industry and cultural heritage. It is also applied on wood materials, with the purpose of improving their shelf-life, by lowering the microbial charge and hence the microbial-related deterioration rate. A fundamental issue when applying γ rays is the preservation of the chemico-physical as well as of the structural and mechanical properties of the materials irradiated, since a significant change of properties may jeopardize the use of the materials for the purpose intended. To this end, in this paper we analyzed the chemico-physical properties of four different types of wood used for the construction of musical instruments namely fir, maple, poplar and durmast oak under increasing doses of γ rays. In detail, the effect of incremental radiation doses was evaluated by comparing the results obtained by acoustic tests with those providing information at molecular level, i.e., cyclic voltammetry, linear square voltammetry and infrared spectroscopy. Moreover, in this work the glucose released as a result of the degradation of wood cellulose and hemicellulose, has been analyzed for the first time, with an innovative tool, based on the use of a Gellan gel. The integrated approach presented here, based on both traditional and innovative techniques has proven to be highly efficient in providing a complete picture of wood behavior following γ-ray irradiation, at both the macroscopic and the molecular level.

[1] Corresponding author: Laura Micheli
Dipartimento di Scienze e Tecnologie Chimiche, Università di Roma Tor Vergata, Via della Ricerca Scientifica, 00173 Roma, Italy; Tel. +390672594420; Fax +390672594328

Keywords: wood, sterilization, γ-rays, FTIR, ATR, electrochemical measurements

1. Introduction

Wood is a material closely associated with human activities since prehistoric times. Owing to its versatility, it has been and is still used for many purposes, such as fuel and building material. Moreover, due to its easy workability, it may be employed to construct vehicles, devices, weapons, tools and everyday objects. Along with these technical applications, wood has soon started to play a leading role as a noble material in the field of visual arts (tables, frames and sculptures) and musical instruments.

Being an organic material, wood is exposed to multiple degradation processes, primarily in connection with biological aggression, but also with abiotic processes such as weathering and oxidation, the latter being driven by complex atmospheric chemistry, hydrolysis and fire damage. However, the major hazard for wood is by far the biologically-mediated degradation. Wood decay is produced by bacteria, fungi, insects, mildews and stains [1-2]. To this end, its management requires both preventative and conservative actions. At present, preventative actions rely on the use of preservatives, often consisting of very toxic substances [2-3]. Physical treatments based on high energy irradiation are appealing methods for the control of biological threats, not only for safety reasons, but also for conservation issues. The use of radiation is - in principle - highly desirable, as it is very efficient, it may be easily conducted in safe conditions and, above all, it is non-destructive. Irradiation for pest control is particularly appealing for archaeological, artistic and musical objects for which maximum care in conservation is a priority [4-5]. Extensive use of this approach has been long known in sterilization procedures as well as in food conservation. γ-irradiation is an effective way to solve the problem of biological infestation of wood, but requires careful characterization of potential side-effects on the material [6-9]. Alterations in wood are indeed detectable already following UV-Vis irradiation [10-12], and the effect of γ-radiation has to be explored in detail as it is likely to affect wood properties at the structural scale. Correlations between structural alteration and acoustic properties have already been the subject of previous investigations leading to associate high energy irradiation with several side effects such as random breakup in the cellulose chain and decrease of tensile strength [6-7, 11-12]. However, the use in wood treatment has been sporadic, the major applications being archaeology or timber industry [7-9]. Usually, proper use and maintenance of wooden musical instruments leads to their successful conservation and performance. However, it

is of uppermost importance to develop additional investigation tools and easy-to-use restoring techniques when dealing with unique instruments. To this purpose, the results are presented of a multidisciplinary approach, aimed at characterizing the effects of γ-irradiation of four different kind of wood samples (laminae): poplar (*Populus Nigra*), durmast oak (*Quercus Petraea*), fir (*Picea Abies*) and maple (*Acer Platanoides*); the last two were selected because they are of paramount importance in the construction of musical instruments, while the other ones were included in the tests to gain a deeper insight on wood behavior following high energy/ increasing dose irradiation.

The growing interest in the effects of wood treatments for preservation purposes is underlined by recent papers where the outcomes are analyzed from a macroscopic point of view [13-15]. To understand the degradation processes, chemical and physical characterization of archaeological wood has been conducted with the aim of assessing the occurrence of modifications both in morphology and in the chemical composition of this material. The most used techniques for this kind of investigation are microscopic and spectroscopic techniques, such as scanning electron microscopy (SEM), Fourier transform infrared spectroscopy (FTIR) [11-12, 16-21], Raman, nuclear magnetic resonance (NMR) and other analytical techniques, such as gel permeation chromatography and analytical pyrolysis coupled with gas chromatography/mass spectrometry (Py-GC-MS) [22]. However, a detailed chemical investigation correlated to the mechanical and acoustic properties upon treatments is reported in few research works [23-27].

The focus of the present paper has been the evaluation of the effects of the increasing doses of γ-rays on the following wood components: cellulose, hemicellulose and lignin [28-31]. Cellulose is a linear, relatively rigid polysaccharide made of β-glucose units linked together by β(1→4) glycosidic bonds, essentially free of branching. Differently from cellulose, hemicelluloses are heterogeneous polysaccharides, with a random amorphous structure, made of several sugar units including xylan, glucuronoxylan, arabinoxylan, glucomannan and xyloglucan [32]. Lignin is a redox-active copolymer constituted of phenyl propane units linked with beta-O-4 ethereal bonds, and containing several carboxyl and carbonyl groups [33]. It undergoes a series of redox reactions, depending on its polymerization degree and thus, on the nature of the plant from which it is extracted [34-35]. The molecular composition of lignin and hemicellulose, and the state of cellulose (crystalline or amorphous state) are varying as a function of the wood state of health and quality [11-12, 19, 30, 34-36].

In the present work, the influence of γ-rays treatments on lignin, cellulose, and hemicellulose in different quality of wood has been assessed focusing on the degradation effects [37] by means of either traditional techniques such as infrared spectroscopy or a fairly innovative approach based on

several electrochemical techniques [38-41] including cyclic voltammetry, linear square voltammetry and amperometry. In particular, the effects of γ-rays treatments on cellulose and hemicellulose have been evaluated using a method involving the application of Gellan gel, coupled to an electrochemical biosensor, based on a screen-printed electrode connected with a portable instrumental setup. This tool was previously developed for cleaning paper artworks since it is suitable for *in situ* and in a simple way the assessment of degradation of artwork [42-43]. Gellan gel is able to remove in non-invasive way degradation products of cellulose present on the surface of wood manufacture, while the biosensor, specific for glucose, the main degradation product of this polysaccharide, offers the possibility to combine the analytical capability of the electrochemical techniques with the detection specificity, characteristic of the biosensor itself. To this end, a glucose biosensor in which glucose is amperometrically detected after the enzymatic conversion of H_2O_2 by glucose oxidase (GOx) was used [44]. At the best of the authors' knowledge, this is one of the few papers in which electrochemical characterization of lignin as a function of its composition has been investigated, as will be described in the results and discussion section. Finally the outcomes were compared to the results of acoustic and mechanical tests previously obtained in order to gain a complete understanding of the effects of this sterilization method on the several woods [11-12, 16-19].

2. Materials and Methods

2.1 Wood samples and their γ-ray irradiation treatments

For the present research wood boards free of macroscopic defects (knots, decay areas, parasites) aged between 5 and 7 years, of poplar (*Populus Nigra*), durmast oak (*Quercus Petraea*), fir (*Picea Abies*) and maple (*Acer Platanoides*) were used; to ensure homogeneity, samples of each species were produced from one single board. Since each type of wood was irradiated at five different doses of γ-rays, six 140x20x3 mm^3 laths were cut, one of which was used as non-irradiated reference, while the other ones were irradiated with the different doses selected.

The irradiation treatments were conducted in an industrial facility, by packing the samples and placing them on the conveyor system (Figure 1). The typical γ-rays source is an array of stainless steel bars loaded with Co-60, the overall activity is usually of the order of the tens of petabecquerel. These systems are capable of delivering very high dose rates: typically, 1-10 kGy are accumulated in a single pass. The material to be irradiated enters the irradiation cell on a conveyor belt and is transported around the powerful gamma source to receive the scheduled dose.

The dose levels selected for the present study were respectively 25, 50, 100 and 200 kGy (with 5% tolerance with respect to the nominal level), corresponding to the usual levels applied against infestants [6-7, 45-49]. As γ-ray irradiation does not activate the materials undergoing treatment, all the samples were safe to handle as soon as they emerged from the irradiation facility [50].
Samples have been stored in the laboratory at 25°C and RH=50%, before and during electrochemical and spectroscopic measurements.

2.1.1 Wood treatment for cyclic and linear sweep voltammetries

Prior to cyclic and linear sweep voltammetry (from now on respectively CV and LSV), wood samples were treated as follows:
wood samples of 2.5 g each were obtained by manually grinding 1 mg of each powder was added with 100µL of a 50mM NaOH, stirring overnight at room temperature. Subsequently the solution was centrifuged (4000rpm for 30 minutes). The supernatant was added with 100µL of 0.1 M phosphate buffer + 0.1 M KCl 0.1M, pH 7.4. CV and/or LSV measurements were carried out using 70 µL of the final solution (the measurements were done with 6replicates per samples)

2.2 Reagents

Gellan gum was purchased from CP Kelco (Atlanta Georgia, USA) under the commercial name KELCOGEL® CG-LA. Glucose oxidase (GOx, EC 1.1.3.4, type II, 15,500 Ug^{-1}, from *Aspergillus Niger*), D (+)-glucose monohydrate, glutaraldehyde (GAD, 25% v\v aqueous solution), calcium acetate, potassium chloride and phosphate buffer were purchased from Sigma-Aldrich (Sigma-Aldrich, St. Louis, MO, USA). Nafion® 5% (v\v) solution was from Carlo Erba (Carlo Erba Reagenti -Italy). All reagents were of analytical grade and used without further purification. The preparation of buffer solutions was made using bi-distilled water (Millipore, Billerica, MA, USA).

2.3 Fourier Transform Infrared Spectroscopy (FTIR) experiments.

Spectra of wood samples (as it was, without any pretreatment) were acquired on a Thermo-Scientific (mod. Is50) instrument (Thermo Scientific Inc., Madison WI), equipped with an attenuated total reflectance (ATR) diamond crystal [42]. Spectra were collected in the region between 4000-525 cm^{-1}, with 64 scans for each sample at a resolution of 2 cm^{-1}, by placing the samples directly on the ATR crystal. All experiments were performed in triplicate on the different wood samples. The characterization of the degradation of the wood components was carried out by

normalizing the absorbance and performing a deconvolution of the bands in the range 840–1900 cm^{-1}, using a sum of Lorentzian/Gaussian functions [42, 49-51]. To this purpose the OMNIC software was employed.

2.4 Electrochemical apparatus and protocols

CV, LSV and amperometry were conducted using a computer-assisted system (AUTOLAB model PGSTAT 12) equipped with GPES software (Metrohm/ECO-CHEMIE, the Netherlands). All the electrochemical data were processed with SigmaPlot 11.0 software.

2.4.1 Screen printed electrode (SPE) preparation

The Screen Printed Electrodes (SPEs) were prepared in the Laboratory of Analytical Chemistry of the University of Rome "Tor Vergata" using a 245 DEK (Weymouth, UK) screen printing machine. Working and counter electrodes were printed on a flexible polyester film (Autostat HT5, Autotype Italia, Milan, Italy) using a graphite-based ink (Electrodag 423 SS from Acheson Milan, Italy) whereas a silver ink (Electrodag 477 SS, from Acheson Milan, Italy) was used for the reference electrode. The diameter of the working electrode was 0.3 cm and its geometric area 0.07 cm^2.

2.4.2 Electrochemical techniques applied for characterization the y-ray effects on wood

The supporting electrolyte used in voltammetric experiments, unless otherwise stated, was a 0.05 M phosphate buffer + 0.1 M KCl, pH 7.4. CV experiments were conducted using a -1 to 1 V potential range and a scan rate of 50 mVs^{-1}, whereas a voltage range from 0 to 0.7 V, a scan rate 50 mVs^{-1} and a step potential 50 mV were used in LSV experiments.

All CV and LSV measurements were repeated in triplicate using three different bare SPEs.

2.4.3 Biosensor for glucose determination and lignin degradation analysis

Glucose is the final product of cellulose hydrolysis, an endogenous paper and wood degradation process [52-53]; to this end, this sugar was chosen as the target to be monitored by the biosensor [53-55]. For the biosensor production, the SPEs were modified with Prussian Blue (PB) (potassium iron (III) hexacyanoferrate (II)) prior to enzyme immobilization. The working electrode surface modification protocol was based on the procedure optimized by F. Ricci et al. [44]. In general, 5 µl of each PB precursor solution, comprised of 0.1 M of $K_3Fe(CN)_6$ in 10 mM HCl and 20 µL of 0.1 M $FeCl_6$ in 10 mM HCl, CV and LSV were applied onto the working electrode area.

The electrodes were incubated for 10 min in the dark, rinsed with 10 mM HCl, and, then, left for 1 h in an oven at 100˚C to obtain a dry and stable active layer of PB. The PB modified electrodes were stored dry at room temperature in the dark until use.

Enzyme modified electrodes were prepared by immobilizing the enzyme of choice onto the surface of PB-modified working electrode using a glutaraldehyde cross-linking method. This was implemented by applying 2 µl of glutaraldehyde (1% v/v) onto the working electrode and allowing the drop to dry before applying 2 µl of a solution containing a mixture of enzyme (GOx – immobilizing 0.37 Unit), Nafion (0.3% in ethanol, pH neutralized with NH_4OH) and BSA (5% w/v) in ratio of (1:1:1) [56-57]. Hydrogen peroxide, produced by the enzymatic reaction in presence of glucose, was detected amperometrically using a SPE modified with Prussian Blue, at an applied potential of 50 mV. The calibration curve of the biosensor was obtained using standard solutions of glucose (fig.S1). The measurements were performed using the non-irradiated wood samples as a reference. The samples were prepared as follows: several standard solutions of glucose (7 concentrations in the range 0 - 1 mM) were added to wood squares (3 cm x 3 cm) that were subsequently dried at 37°C for 2 h. The Gellan gel was then applied to the surfaces and measurements were performed as reported in the next paragraph of the experimental section. The resulting calibration curve was compared with the ones obtained using known standard glucose solutions to calculate the dilution factor F (due to water present in the gel and in the sampling system):

$$F = 100 \times \frac{i_c}{i_f} \qquad (1)$$

where i_c is the mean value of current measured for each glucose concentration present on the wood samples and removed by the method proposed, and i_f is the current mean value obtained by measuring the glucose in solution at the same concentration.

The electrochemical analysis was conducted on wood powder previously treated with an alkaline attack, aimed at making the lignin more soluble in the buffer solution. The resulting CV and LSV profiles were, then, compared with those obtained using not irradiated lignin.

In detail, 2.5 g of each wood sample (treated or not with γ-rays) were grafted; then, 1 mg of the homogenized samples were dissolved in 100 µl of a 50 mM NaOH solution for the extraction of alkaline lignin. The mixtures were stirred overnight at room temperature, and then centrifuged at 4000 rpm for 30 minutes. The supernatant was removed and 100 µl of phosphate buffer (0.1M + 0.1M KCl, pH 7.4) was added to obtain a wood final concentration of 0.4 mg mL^{-1} for each sample.

2.4.4 Amperometric measurements of cellulose degradation analysis using Gellan gel

The Gellan hydrogel was prepared according to the general protocols reported elsewhere [42, 51]; in detail, to prepare the hydrogel containing calcium ions an aqueous solution of deacylated Gellan gum (20 gL^{-1}) was mixed for almost a minute with a solution of calcium acetate (0.40 gL^{-1}) in a microwave at 600W (Mars Microwave, CEM Corporation, Matthews, NC, USA) until the sample boiled and became transparent; then it was left to cool on a Petri dish. Subsequently, all the wood specimens were completely covered with the gel to recover the degradation products by adsorption; the process was optimized by pressing each sample with a glass plate under a 550 g weight for 60 min at room temperature. Prior to amperometric analysis, 1 g of the Gellan gel from wood sample treatment was stirred together with 1 ml of 50 mM phosphate buffer, pH 7.4 for 90 minutes to extract the wood degradation products adsorbed. The solution was finally centrifuged for 30 minutes at 5000 rpm and the supernatant analyzed by amperometric measurements [58]. The amperometric measurements were carried out applying -50 mV vs pseudoreference of Ag for 180s

2.5 Mechanical tests

A three-point bending flexural test was adopted, yielding the bending modulus of elasticity and the maximum load the sample could sustain before breaking. The tests were conducted on six samples per wood species and per irradiation level, to obtain reasonable statistics. The tests were conducted in keeping with the European Norm EN 408:2010, at the mechanical laboratories of the Department of Industrial Engineering of the University of Bologna. Two machines were used for the tests: an Instron series 8500 model 8033 universal testing machine and an 8032 model [45, 59]. 6 laths of each wood species were used for the destructive mechanical testing aimed at determining the load to rupture and the modulus of elasticity, and the broken specimens were subsequently used for the spectroscopic and electrochemical analyses object of the present paper.

3. *Results and Discussion*

As stated in the introduction, the purpose of the present work has been to analyze the effects of γ radiations on different types of wood at a chemical level. To this end, a comprehensive ensemble of traditional and innovative techniques such as FTIR and electrochemical experiments has been put in place, with the aim to obtain a deeper insight on the resulting modifications and degradation of cellulose, hemicellulose and lignin.

3.1 FTIR-ATR experiments

Infrared spectroscopy is a technique universally used to study the degradation processes occurring on the constituents of wood, i.e. cellulose, hemicellulose and lignin [11-12; 60]. In this work ATR spectra were collected and evaluated for wood diagnostics following high energy irradiation. A clear-cut evaluation of the effects of γ-irradiation on these wood components has been achieved by analyzing the intensities of a series of diagnostic bands. In particular, six bands were selected for the analysis, centered at about 896 cm^{-1}, 1160 cm^{-1}, 1505 cm^{-1}, 1600 cm^{-1}, 1640 cm^{-1} and 1740 cm^{-1}. The band at 896 cm^{-1} was chosen as it is characteristic of the C-C-H deformation in cellulose, whereas hemicellulose and oxidized groups in cellulose can be identified through the stretching of unconjugated C=O groups, at 1740 cm^{-1}. In addition, the band centered at 1160 cm^{-1} has been examined, corresponding to the bending of the C-O-C groups present in holocellulose, which is the total amount of cellulose and hemicellulose, together. The band at 1505 cm^{-1} has been checked as a function of γ-ray doses, because it is associated with the skeletal vibration of the aromatics and is diagnostic of the presence of lignin. Finally, the band at 1640 cm^{-1} is due to bound water, whereas the one at 1600 cm^{-1} corresponds to the skeletal vibration of the aromatics conjugated with C=O stretching [16, 59]. The former, in particular, is important, because an increase in the amount of water present in the samples might accelerate sample degradation [36].

To obtain a direct comparison between different experiments, we used, as a reference, the band at 1045 cm^{-1}, assigned to the C–O stretching associated with primary alcohols in holocellulose and lignin, and is found to be one of the bands changing the least upon treatments [12,16]; this means that the absorbance of the selected bands in the spectra have been normalized by the one obtained at 1045 cm^{-1}. Moreover, the ratio between the bands at 1505 and 1600 cm^{-1} (labelled, from here onward, L.O.) is calculated as it gives an indication of the degree of oxidation of lignin.

FTIR-ATR spectra are presented in Figure 2, whereas the effects of the diagnostic bands on the intensity [44] (as obtained from the deconvolution method as described in Materials and Methods), as a function of γ-ray doses, are reported in Figure 3.

Several changes are evident in all the spectra; however, the most striking feature is that the γ irradiation processes appear to clearly affect the polysaccharide and the lignin moieties of the different wood samples to different extents (Figure 3 A-D).

Small changes are observed in the overall FTIR-ATR spectra of poplar (Figure 3A) as a function of the γ-ray dosage; the most notable variation is the increase of the band at 1730 cm^{-1} as a result of the chemical oxidation of cellulose. As regards lignin, the intensity of the band at 1505 cm^{-}

[1] remains constant independently of the γ-ray dosage, thus implying that the lignin content is not affected by the sterilization treatments. Simultaneously, the labelled L.O. ratio remains constant, suggesting that no variation in the C=O content in lignin due to aging occurs. Finally, the oscillating changes in intensity of the band at 1640 cm^{-1} indicate a variation in the water bound content.

The analysis of the spectra of durmast wood (Figure 3B) shows that the relative intensity of the band at 896 cm^{-1}, attributable to cellulose, decreases on increasing the γ-ray dosage, indicating that also in this case, cellulose undergoes modification and degradation. The intensity of the bands at 1733 cm^{-1}, 1160 cm^{-1}, 1640 cm^{-1}, and 1505 cm^{-1} changes on ageing; this means that the degradation involves both holocellulose and lignin. Moreover, the changes with the γ-ray dosage are complex, but display a peculiar trend, with the peaks of lignin (1505 cm^{-1}), water (1640 cm^{-1}) and oxided groups in cellulose and hemicellulose (1733 cm^{-1}) reaching a maximum for 50 kGy, decreasing and, then, slightly increasing again for 200 kGy. Finally, the L.O. ratio increases up to 100 kGy irradiated samples and then slightly decreases, suggesting that the irradiation with γ-rays always involves lignin oxidation.

In maple an overall decrease of bands intensities, corresponding to an overall degradation of wood components (Figure 3C) upon increasing γ-ray irradiation is found. The relative intensity of the band at 1505 cm^{-1} (due to the lignin) decreases, though the L.O. increases suggesting progressive lignin degradation due to the sterilization. Simultaneously, a decrease of the intensity of the bands at 1160 and 1730 cm^{-1} related to the holocellulose and the xylan groups in hemicellulose is observed. After an initial decrease, the relative intensity ratio of band at 896 cm^{-1} increases for the 200 kGy irradiated samples. This suggests a preliminary alteration of the cellulose components; at higher irradiation doses, however, the modifications in lignin overcome those of cellulose as shown by the increase in its bands.

As far as fir is concerned (Figure 3D), again, a complex variation is observed for both lignin and cellulose components (oxidized or not) as a function of the irradiation dose, with the exception of the band at 1160 cm^{-1}, related to the holocellulose content. The variations, however, are smaller as compared to durmast. In particular, the overall data indicate a decrease of the lignin content (as demonstrated by the decrease of the band at 1505 cm^{-1}) and an increase of the amount of water in the samples (except after a 50 kGy irradiation dose). It is noteworthy that in fir, irradiation does not induce the oxidation of lignin and holocellulose moieties, as demonstrated by the general diminishing of the L.O. ratio and of the band at 1730 cm^{-1}.

It appears that while ATR spectra obtained clearly reveal the influence of γ irradiation on wood, the actual behaviour is neither easily interpretable at this stage nor comparable both across species and irradiation doses. The authors speculate that this might be due to the relative importance of different distinct processes, including depolymerization and cross-linking as suggested by several papers (11-12, 31) leading to contrasting effects on a series of IR bands as actually observed. Such characterization would require further evaluations and quantification attempts through techniques among which a combination of chemometric and IR bands which is beyond the scope of the present work, aiming at evaluating the preservation of acoustic properties of wood for the construction of musical instrument and not merely devoted to conservation problems.

3.2 Electrochemical characterization of wood: lignin degradation

Before performing the electrochemical characterization of the wood samples, a preliminary set of CV and LSV measurements was performed in order to determine the effects of the supporting electrolyte. To this purpose, pure lignin extracted from silver fir was used as a reference and deposited on bare SPEs. The results are reported in the ESM (Figures S2 and S3) and indicate that CV and LSV are suitable techniques for monitoring the electrochemical behavior of lignin in the μg mL^{-1} range, using 0.1 M phosphate buffer pH 7.4.

Afterwards, the electrochemical behavior of the four wood species under examination has been followed by monitoring the CV and LSV lignin profile. Alkaline extracts of both non-irradiated and irradiated wood specimens were subjected to cyclic voltammetry under different conditions of scan speed/rate and potential. The results are summarized in Figure 4A and B and Figure S6.

No electrochemical signal is observed analyzing the extracts of the non-irradiated samples, indicating the absence of electrochemically active species. Similarly, no electrochemical interference is observed from the alkaline medium used to recover the extracts. In the case of the four wood samples no signal is observed below 200 kGy doses (Figure 4A), whereas the CVs of the extracts of poplar and durmast, irradiated with a dose of 200 kGγ, show an oxidation peak at around 100 mV and a reduction peak at approximately -100 mV (Figure 4B). A comparison of these voltammograms with that of pure lignin obtained in analogous experimental conditions show similar profiles; an oxidation peak at around to 100 mV and a reduction peak at approximately -100 mV are indeed present (Figure 4B and Figure S2, S3).

These results indicate that this irradiation dose has affected the structure of wood, producing electroactive degradation compounds, partly deriving from lignin (see Figure S3). It should be

noted that the absence of signals obtained from wood subjected to lower irradiation doses might be due to the relatively low sensitivity of CV technique (detection limit: 10^{-6} M). To this end, similar measurements were repeated using the linear square voltammetry (LSV), a more sensitive technique (detection limit: 10^{-8} M). In this case, the oxidation, rather than the reduction region was studied, because the results were more reproducible ($RSD\%_{ox}$= 3%, RSD_{red}= 10%) (Figure 5). With this technique, all the extracts of wood samples subjected to medium-low irradiation dose (25-50 kGγ) did not show appreciable electrochemical responses (data not shown), whereas those treated with the highest irradiation power (except for poplar) showed a peak at 493 mV, which is comparable with the peak present in the CV of pure lignin (Figure S3).

Durmast shows a different behavior, with two peaks instead of one in the characteristic region of lignin oxidation, suggesting the presence of other electroactive degradation products, resulting from the degradation processes of lignin, as a consequence of γ-treatments. This is in agreement with the results of Parpot et al. [40] and with the electrochemical behavior of vanillin, one of degradation product of lignin, as reported by Bertazzi et al. and Peng et al. [61-62]. These results show that irradiation at doses up to 100 kGγ does not produce significant effects on the wood molecular structure, but can however break some inter- and intra-molecular bonds among the various wood components, in a nonspecific way, generating electroactive moieties. The overall electrochemical results are in good agreement with the infrared analysis results.

3.3 Electrochemical characterization of wood: determination of the cellulose degradation

In this section, the authors report the effects of γ-irradiation treatments on cellulose and hemicellulose. To investigate these potential effects, a non-invasive method, applied to paper artworks for a real-time monitoring of the paper cleaning processes, has been employed in according to a method previously set-up by the authors [51, 58, 63]. The description of the system applied is reported in par. 2.4.3 and 2.4.4. In a previous application of the method on paper artworks [63] a dilution of the glucose released was observed due to the water in the Gellan gel. For this reason, the dilution factor of the glucose measured was calculated for the wood samples as reported in "Material and Methods", section "*Glucose determination on irradiated wood",* allowing to correct experimental data by a factor corresponding to (48 ± 1) %.

Gel-extracted glucose was measured by the selective electrochemical sensor directly on the wood sample surface. This allowed to determine the amount of glucose released from cellulose degradation as induced by γ doses on the different types of wood. The results are reported in Table 1.

In particular for poplar and durmast, the amount of glucose product after γ irradiation, increased with the γ-ray doses up to 100 kGγ, to decrease at 200 kGγ, an oscillating behavior similar to the one observed with FTIR/ATR (see "Results and Discussion", section FTIR measurements on wood samples). The wood samples analyzed gave different results in terms of glucose production, showing different trends as a function of irradiation dose. This is probably due both to different wood composition and preservation state and different degradation level due to γ-rays.

3.4 A joint platform for wood analysis

The combined IR, CV, LSV and Gellan gel-extracted glucose analyses depict a complex scenario of wood degradation upon γ-ray treatment, where initial composition, initial degree of degradation and ageing play key roles. From a comparison with the results (currents *vs* potential) obtained with a cellulose and lignin standards, it is possible to understand the amount of cellulose and lignin present in the wood sample, the presence and/or production of the degradation product of cellulose and lignin due to the γ-radiation treatment.

The overall scenario indicates different behavior of the different wood types as a function of the γ-ray irradiation.

Poplar shows the least modifications for all the investigated wood components, as a function of the irradiation (IR spectra) as well as the least variation in the amount of oxidized lignin (L.O.). This is consistent with the LSV measurements, which indicate the highest content of oxidizable electroactive lignin among all woods, after 200 kGy irradiation. In terms of degradation products as measured by glucose content, an initial increase by irradiation is followed by a plateau and then by a subsequent decrease at the highest dose.

Maple shows small variations of the wood components, with a linear trend and a decreasing content of the oxidized lignin fraction. This is, again, consistent with the LSV measurements that indicate a small residual of oxidizable electroactive lignin upon the highest dose of γ rays. The overall glucose content remains rather constant throughout the irradiation steps.

Durmast displays a sort of paradigmatic behavior, with a complex dependence of wood components as a function of the irradiation doses, a decreasing amount of glucose as degradation product upon the first irradiation dose that stays, then, constant at higher irradiation doses, and a double oxidation peak in LSV, typical of vanillin generation upon degradation. Furthermore, the ratio of oxidized lignin does not parallel to lignin content (L.O. in the IR spectra). This suggests a two-step wood degradation, where lignin acts as a protective component. As soon as the first

fraction is either decomposed or oxidized, the degradation of the other components proceeds to a higher extent.

Fir, as durmast, shows a complex behavior of the wood components as a function of the irradiation, though the lignin ratio, first, decreases and, then, increases. The overall fraction of oxidized lignin is lower as compared to durmast and no oxidizable electroactive fraction of lignin is detected at all by LSV measurements of the most irradiated sample. The released glucose level is the highest of all the woods, and remains constant regardless of the irradiation, suggesting that it is an intrinsic amount, rather than a degradation product.

3.5 Mechanical tests and correlation to the chemical composition of the woods

The modulus of elasticity and the maximum rupture load were measured for all wood samples and irradiation doses, to determine whether the wood sterilization has effects at the macroscopic level and if a relationship can be found between macroscopic and chemical properties of the wood samples. This is even more important in the perspective of adopting γ-rays as a preservation tool for woods for musical instruments, where the elasticity properties are an asset. The results of the tests are reported in Figure 5. It can be observed that the mechanical properties of all woods are affected by γ-ray irradiation, though to different extents and trends depending on the wood type. Provided that the modulus of elasticity and the rupture load have systematically opposite trends, we can focus to just one of these properties, say the modulus of elasticity.

As reported in Figure 6, poplar, durmast and fir display an increase of the modulus of elasticity with the irradiation dose (i.e. the wood becomes stiffer). On the contrary, maple is characterized by a decrease of the modulus of elasticity upon irradiation. The variations are not linear with the γ ray dose. Typically, the loss of elasticity is ascribed to cellulose degradation [6, 44]; on the other hand, lignin (which is reported to be more resistant to γ-radiation than cellulose) clearly plays a role in the overall mechanical properties. It is noteworthy that, in the present set of data, the modulus of elasticity of the woods upon irradiation mostly parallels the lignin content ratio, as determined by IR measurements. Some discrepancies are observed for poplar, which is the wood with the largest amount of oxidizable electroactive lignin (LSV measurements), thus suggesting that the lignin type (oxidation, branching etc.) also influence the degradation pathway.

4. Conclusions

In this work a focused investigation on the possibility of using γ-rays for the preservation of wood materials from biological threats has been reported. In detail, the effects of high energy irradiation as a sterilizing method were have been investigated on four different types of wood (poplar, maple, durmast and fir), treated with different increasing doses of γ-rays. Structural analysis by both conventional methods (FT-IR, CV and LSV) and up-to-date analytical techniques such as based on voltammetric and amperometric biosensors, applied within an integrated and smart flow sampling tool, has led to understanding and partly reconstructing the chemical and structural modifications occurring at the molecular level when this sterilization method is adopted. Though the trends of lignin and glucose levels released under increasing intensity of irradiation depend on the specific type of wood, there is a general agreement between the data obtained with mechanical analysis and the various analytical techniques applied, thus showing that the integrated use of infrared spectroscopy and electrochemical measurements are a suitable platform to assess the degree of wood degradation following γ-ray irradiation.

The study of the mechanical properties of the investigated wood samples confirmed that all samples have been negatively affected by γ-ray irradiation, though to different extents and trends depending on the wood type. The overall results from the chemical characterization herein presented confirmed how irradiation by high energy electromagnetic is detrimental to this material, revealing, at least preliminarily, the link between macroscopic physical properties and chemical modifications occurring at the molecular/supramolecular level following a high-energy treatment.

In fact, while the primary scope of this work was the assessment of the effects produced by γ-ray irradiation on wood and the consequences on the acoustic properties of this material in the field of musical instruments, [cancellato un inciso perchè spostato prima] the results obtained prove once again as extremely promising in the cultural heritage field, where the overall approach will allow to determine the degradation state of wood artworks, thanks to its relatively safe, portability and, low cost. In fact, from the comparison of the results obtained from the application of spectrophotometric, electrochemical and mechanical tests, the principal results, that emerges (cancellare virgola ed s), underlines that the type and quality of wood answered in different way to the increasing doses of γ-rays. This behavior can be ascribed to the classification of wood in softwood or hardwood, and consequently to the distinct lignin structure, enriched in guaiacyl units the former and syryngil+guaiacyl the latter.

Acknowledgments

We are grateful to prof. C. Crestini for useful suggestions and pure lignin samples. The authors are grateful to Jury Cecca, Raffaella Lettieri, I. Bonacini, Yuanyuan Zhang for their contribution in this research work. Special thanks to the professors Antonio Palleschi and Giuseppe Palleschi, that have supported this work both financially and scientifically. We, also, thank Eng. Gabriele Ricci for his contribution in the mechanical and acoustic testing conducted on the woods subsequently investigated in the present paper, and for offering the woods themselves for the chemical tests object of the analyses presented here.

Conflict of interest

The authors declare that they have no conflict of interest.

References

1. R.M. Rowell. Handbook of Wood Chemistry and Wood Composites, CRC Press, 2005.

2. G. Tsoumis. Science and Technology of Wood. Structure, properties, utilization, Springer, 1991.

3. A. Unger, A. Schniewind, W. Unger. Conservation of Wood Artifacts: A Handbook, Springer Science & Business, New York, 2001.

4. C.M. Freitag, J.J. Morrell, Use of γ-radiation to eliminate fungi from wood, Forest Prod. J., 48(3) (1998) 76-78.

5. B. Katušin-Ražem, D. Ražem, M. Braun, Irradiation treatment for the protection and conservation of cultural heritage artefacts in Croatia, Radiat. Phys. Chem., 78 (2009) 729–731.

6. R. Despot, M. Hasan, C. Brischke, C.R. Welzbacher, A.O. Rapp, Changes in physical, mechanical and chemical properties of wood during sterilisation by γ-radiation, Holzforschung, 61 (2007) 267–271.

7. R. Despot, M Hasan, A.O. Rapp, C. Brischke, M. Humar, C.R. Welzbacher, D. Ražem, Changes in Selected Properties of Wood Caused by Γ Radiation, Chapter 14. In γ-Radiation, Adrovic F. ed., 2012.

8. S.O. Inyang, I.S. Inyang, N.O. Egbe, Radiation exposure levels within timber industries in Calabar, Nigeria, J. Med. Phys., 34(2) (2009) 97–100.

9. H.J. Banks, Alternatives to methyl bromide for durables and timber. Proceedings of International Conference on Alternatives to Methyl Bromide "The Remaining Challenges", Batchelor T and José Bolivar J (Eds.), European Commission, Brussels, Belgium, pp. 1-5, 2000.

10. F. Divos, L. Bejo, The effect of γ-irradiation on the MOE of various species, Wood Sci. Technol., 40 (2006) 87–93.

11. X. Colom, F. Carrillo, F. Nogues, P. Garriga, Structural analysis of photodegraded wood by means of FTIR spectroscopy. Polym. Degrad. Stab. 80 (2003) 543-549.

12. D. Rosu, C. A. Teaca, R. Bodirlau, L. Rosu, FTIR and color change of the modified wood as a result of artificial light irradiation. J. Photoch. Photobio. B. 99 (2010) 144–149.

13. B.P. Jelle, P.J. Hovde, Fourier Transform Infrared Radiation Spectroscopy Applied for Wood Rot Decay and Mould Fungi Growth Detection, Advances in Materials Science and Engineering, 2012 (2012) Article ID 969360, 6 pages, http://dx.doi.org/10.1155/2012/969360

14. S. Rimdusit, S. Wongsongyot, S. Jittarom, P. Suwanmala, S. Tiptipakorn, Effects of γ-irradiation with and without compatibilizer on the mechanical properties of polypropylene/wood flour composites, J. Polym. Res., 18 (2011) 801–809.

15. L. C. Severiano, F.A.R. Lahr, M.A.G. Bardi, A. C. Santos, L.D.B. Machado. Influence of γ radiation on properties of common Brazilian wood species used in artwork. Progress in Nuclear Energy 52 (2010) 730-734.

16. K.K. Pandey et al, FTIR studies of the changes in wood chemistry following decay by brown-rot and white-rot fungi, Int. Biodeterior. Biodegrad., 52 (2003) 151-160.

17. E.D. Tomak et al. An FT-IR study of the changes in chemical composition of bamboo degraded by brown-rot fungi, Int. Biodeterior. Biodegrad., 85 (2013) 131-138.

18. S. Durmaz, Examination of the chemical changes in spruce wood degraded by brown-rot fungi using FT-IR and FT-Raman spectroscopy, Vib. Spectrosc., 85 (2016) 202-207

19. H. Chen, C. Ferrari, M. Angiuli, J. Yao, C. Raspi, E. Bramanti, Qualitative and quantitative analysis of wood samples by Fourier transform infrared spectroscopy and multivariate analysis Carbohydrate Polymers 82 (2010) 772–778

20. K.K. Pandey, A.J. Pitman, A.J., FTIR studies of the changes in wood chemistry following decay by brown-rot and white-rot fungi, Int. Biodeterior. Biodegrad., 52 (2003) 151-160.

21. S. Durmaz, Ö. Özlem, H. Ismail, C. Ümit, E. Emir, Examination of the chemical changes in spruce wood degraded by brown-rot fungi using FT-IR and FT-Raman spectroscopy, Vib. Spectrosc., 85 (2016) 202-207.

22. J.J. Łucejko, F. Modugno, E. Ribechini, D. Tamburini, M.P. Colombini. Analytical instrumental techniques to study archaeological wood, Applied Spectroscopy Reviews 50 (2015) 584-625.

23. C. B. Wessels, F. S. Malan, T. Rypstra, A review of measurement methods used on standing trees for the prediction of some mechanical properties of timber. European Journal of Forest Research 130(6) (2011) 881–893.

24. J. J. Łucejko, J. La Nasa, C. M.A. McQueen, S. Braovac, M. P. Colombini, F. Modugno, Protective effect of linseed oil varnish on archaeological wood treated with alum, Microchem. J. 139 (2018), 50-611.

25. S. Bugani, F. Modugno, J. J. Łucejko, G. Giachi, S. Cagno, P. Cloetens, K. Janssens, L. Morselli, Study on the impregnation of archaeological waterlogged wood with consolidation treatments using synchrotron radiation microtomography. Anal. Bioanal. Chem. 395 (2009) 1977-1985

26. D. Tamburini, J. J. Łucejko, F, Modugno, M, P, Colombini, Combined pyrolysis-based techniques to evaluate the state of preservation of archaeological wood in the presence of consolidating agents, J. Anal. Appl. Pyrolysis 122 (2016) 429–441

27. C.M.A. McQueen, D. Tamburini, J.J. Łucejko, S. Braovac, F. Gambineri, F. Modugno, M.P. Colombini, H. Kutzke. New insights into the degradation processes and influence of the conservation treatment in alum-treated wood from the Oseberg collection, Microchem. .J. 132 (2017), 119–129

28. L. Zoia, D. Tamburini, M. Orlandi, J.J. Łucejko, A. Salanti, E.L. Tolppa, F. Modugno, M.P. Colombini, Chemical characterization of the whole plant cell wall of archaeological wood: an integrated approach, Anal. Bioanal. Chem. 409 (2017) 4233-4

29. A.J. Swallow, Radiation chemistry of organic compounds. International series of monographs on radiation effects in materials. London: Pergamon Press. 1960.

30. S. Curling, J.E. Winandy, Comparison of the effects of γ-irradiation and steam sterilization on southern pine sapwood, Forest Prod. J., 58(1) (2008) 87-90.

31. F. Khan, S.R. Ahmad, E. Kronfli, γ-radiation induced changes in the physical and chemical properties of lignocellulose, Biomacromolecules, 7(8) (2006) 2303-2309.

32. M.C. Area, H. Cheradame, Paper aging and degradation: recent findings and research methods, Bioresour., 6(4) (2011) 5307-5337.

33. H. Lange, S. Decina, C. Crestini, Oxidative upgrade of lignin–Recent routes reviewed, Eur. Polym. J., 9(6) (2013) 1151-1173.

34. H.L. Chum, ORGANIC Electrochemistry. An introduction and guide. 3rd ed., Lund H, Baizer HM editors, Marcel Dekker, New York, 1991.

35. M.A. Ribeiro, H. Oikawa, M.N. Mori, C.M. Napolitano, C.L. Duarte, Degradation mechanism of polysaccharides on irradiated sugarcane bagasse, Radiation Physics and Chemistry 84 (2013) 115–118.

36. C. Casieri, S. Bubici, I. Viola, F. De Luca, A low-resolution non-invasive NMR characterization of ancient paper, Solid State Nuclear Magnetic Resonance, 26 (2004) 65–73.

37. B. K. Mahato, Aspects of the Role of Lignin Additives in Pasted Lead Electrodes, J. Electrochem. Soc., 124(11) (1977) 1663-1667.

38. M.Y. Vagin, S.A. Trashin, A.A. Karyakin, Corrosion protection of steel by electropolymerized lignin, Electrochem. Comm., 8 (2006) 60–64.

39. G. Milczarek, Preparation and characterization of a lignin modified electrode, Electroanal., 19(13) (2007) 1411-1414.

40. P. Parpot, A.P. Bettencourt, A.M. Carvalho, E.M. Belgsir, Biomass conversion: attempted electrooxidation of lignin for vanillin production, J. Appl. Electrochem., 30 (2000) 727-731.

41. E. Evstigneev, S. Shevchenko, H. Mayorova, A. Platonov, Polarographically Active Structural Fragments of Lignin. II. Dimeric Model Compounds and Lignins, J. Wood Chem. Technol., 24 (2004) 263-278.

42. C. Mazzuca, L. Micheli, M. Carbone, F. Basoli, E. Cervelli, S. Iannuccelli, S. Sotgiu, A. Palleschi, Gellan Hydrogel as a Powerful Tool in Paper Cleaning Process: A Detailed Study, J. Colloid Interf. Sci., 416 (2014) 205-211.

43. L. Micheli, C. Mazzuca, A. Palleschi, G. Palleschi, Combining a hydrogel and an electrochemical biosensor to determine the extent of degradation of paper artworks, Anal. Bioanal. Chem., 403(6) (2012) 1485-1489.

44. F. Ricci, A. Amine, C. S. Tuta, A.A. Ciucu, F. Lucarelli, G. Palleschi, D. Moscone, Prussian Blue and enzyme bulk-modified screen-printed electrodes for hydrogen peroxide and glucose determination with improved storage and operational stability. Anal. Chim. Acta., 485(1) (2003) 111-120.

45. G. Ricci, R. Regazzi, L. Tositti, L. Barbaresi, A. Liverani, D. Mostacci, A comprehensive investigation of mechanical and acoustic modifications in wood treated with high doses of γ-radiation for sterilization. Rad. Eff. Defects Solids 171(9,19) (2016) 714–725.

46. OEPP/EPPO (European and Mediterranean Plant Protection Organization) Bulletin. Disinfestation of wood with ionizing radiation. 39 (2009) 34–35.

47. H. Kasprzyk, K. Wichłacz, S. Borysiak, The effect of γ-radiation on the supramolecular structure of pine wood cellulose in situ revealed by x-ray diffraction, EJPAU 7(1) 2004.

48. S.B. Pointing, E.N.G. Jones, A.M. Jones, Decay prevention in waterlogged archaeological wood using γ-irradiation, Int. Biodeter. Biodegr., 42(1) (1998) 17-24.

49. T. Schnabel, H. Huber, T. A. Grünewald, A. Petutschnigg, Changes in mechanical and chemical wood properties by electron beam irradiation, Appl. Surf. Sci., 332 (2015) 704-709.

50. J. R. Lamarsh,A. J. Baratta, Introduction to Nuclear Engineering, 3rd ed.; Prentice Hall: Upper Saddle River, NJ, (USA) 2001.

51. M. Picollo, E. Cavallo, N. Macchioni, O. Pignatelli, B. Pizzo, I. Santoni., Spectral Characterization of Ancient Wooden Artefacts with the Use of Traditional IR Techniques and ATR Device: A Methodological Approach. E-Preservation Science, 8 (2011) 23-28.

52. M. Strlic, J. Kolar J, S. Scholten. Paper and durability. In: Ageing and stabilization of paper. Strlic M, Kolar J Editors, Ljubljana National and University Library, pp. 1-23, 2005.

53. J. Lojewska, P. Miscowiec, T. Lojewski, L.M. Proniewicz, Cellulose oxidative and hydrolytic degradation: in situ FTIR approach, Polym. Degrad. Stab., 88 (2005) 512–520.

54. L. Micheli, C. Mazzuca, A. Palleschi, G. Palleschi, Development of a diagnostic and cleaning tool for paper artworks: a case of study, Microchem. J., 126 (2016) 32–41.

55. Z. Zhiwei, J. Helong, Enzyme-based Electrochemical Biosensors. In: Biosensors.. Serra PA editor, INTECH, Croatia, 2010, pp. 302-324 .

56. M. Mahosenaho, L. Micheli, F. Caprio, A. M. Sesay, G. Palleschi, V. Virtanen, A disposable biosensor for the determination of alpha-amylase in human saliva, Microchim. Acta, 170(3-4) (2010) 243-249.

57. A. A. Karyakin, E. E. Karyakina, Electroanalytical application of Prussian Blue and its analogs, Russ. Chem. B., 50(10) (2001) 1811-1817.

58. L. Micheli, C. Mazzuca, E. Cervelli, A. Palleschi, New strategy for the cleaning of paper artworks: A smart combination of gels and biosensors. Ad..Chem. 2014 (2014) 1-10 ID 385674.

59. S. O. Inyang, I. S. Inyang, N. O. Egbe. Radiation exposure levels within timber industries in Calabar, Nigeria. J. Med. Phys. 34(2) (2009) 97–100.

60. K. K. Pandey, A study of chemical structure of soft and hardwood and wood polymers by FTIR spectroscopy. J. Appl. Polym. Sci., 71 (1999) 1969-197.

61. F. Bettazzi, I. Palchetti, S. Sisalli, M. Mascini, A disposable electrochemical sensor for vanillin detection. Anal. Chim. Acta, 555(1) (2006), 134–138.

62. J. Peng, C. Hou, X. Hu. A Graphene-Based Electrochemical Sensor for Sensitive Detection of Vanilli, Int. J. Electrochem. Sci., 7 (2012) 1724-1733.

63. L. Micheli, C. Mazzuca, M. Missori, L. Teodonio, A. Mosca Conte, O. Pulci, L. Arcadipane, S. Dominijanni, A. Palleschi, G. Palleschi, S. Iannuccelli, S. Sotgiu, Interdisciplinary approach to develop a disposable real time monitoring tool for the cleaning of graphic artworks. Application on "le Nozze di Psiche", Microchem. J., 138 (2018) 369-378.

Table 1. Amount of glucose extracted using Gellan gel coupled with electrochemical biosensor from poplar, durmast, maple and fir treated with different doses of γ-rays

	Poplar	**Durmast**	**Maple**	**Fir**
	Glucose (mM±σ)	*Glucose (mM±σ)*	*Glucose (mM±σ)*	*Glucose (mM±σ)*
Non-treated	0.32±0.04	0.88 ± 0.07	0.58 ± 0.01	2.90 ± 0.01
25γ	1.12± 0.09	0.34± 0.06	0.34±0.02	2.94± 0.05
50γ	1.22 ± 0.01	0.42± 0.04	0.36±0.02	2.92± 0.06
100γ	1.34 ± 0.03	0.58± 0.05	0.42±0.04	2.98± 0.01
200γ	0.82 ± 0.04	0.34±0.01	0.44±0.08	2.92± 0.04

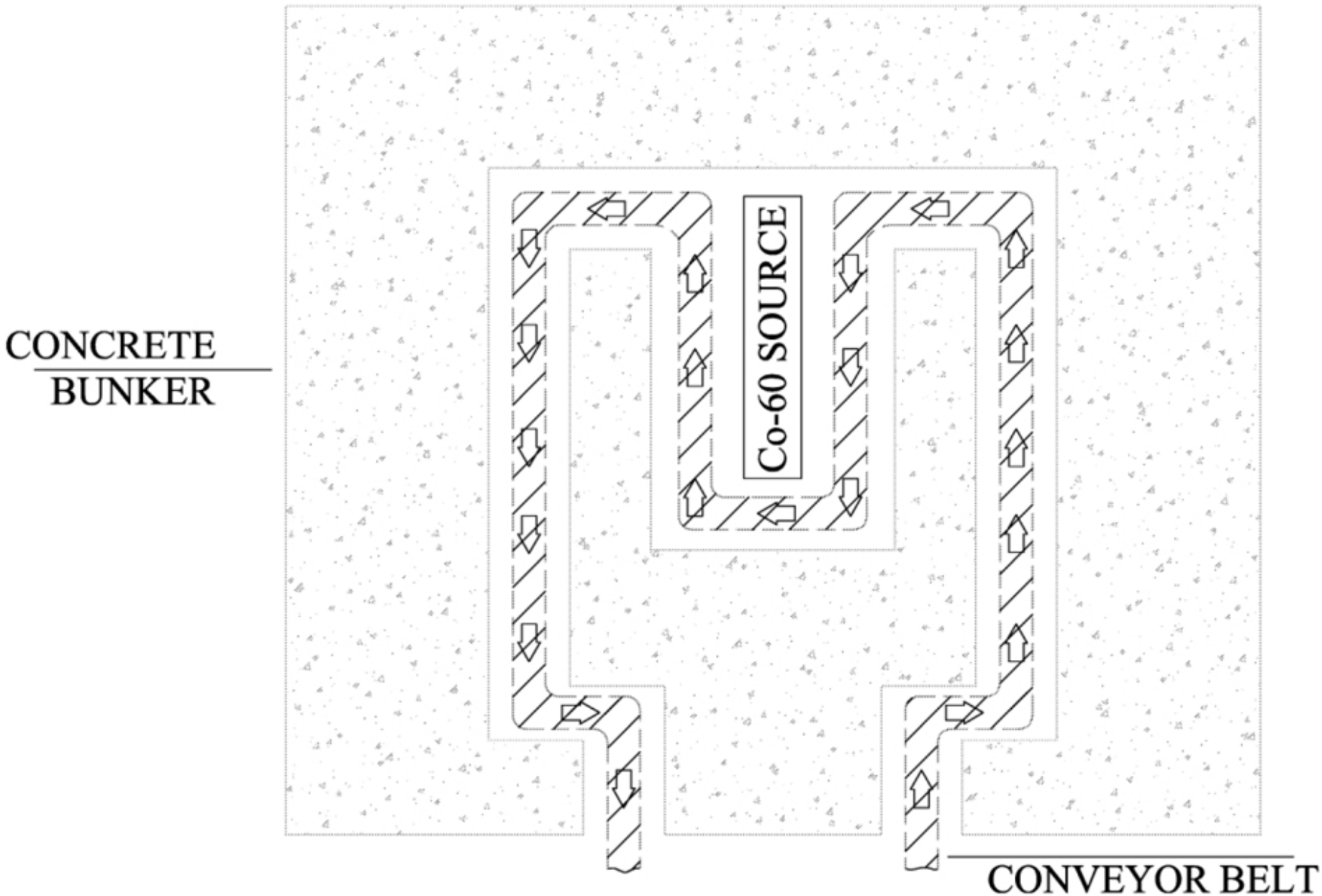

Figure 1

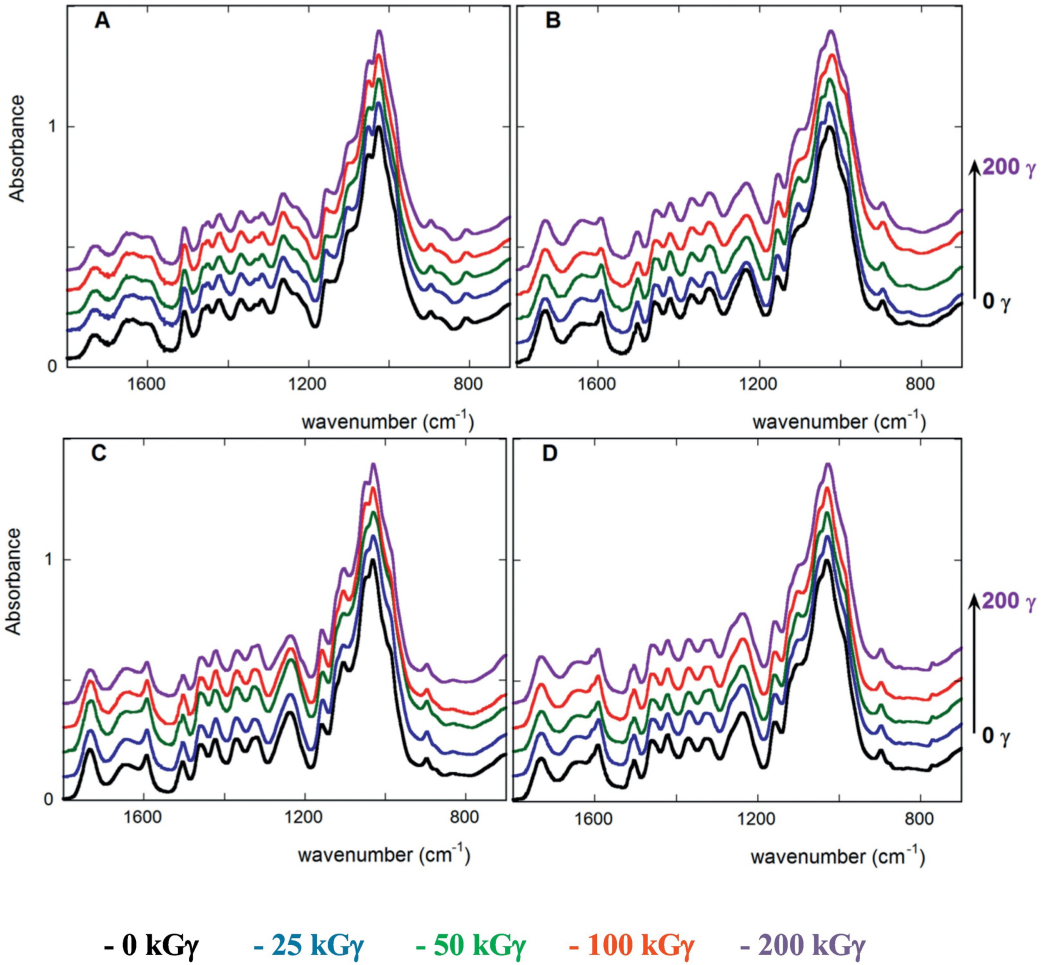
A
B
C
D
Absorbance
1
0
1600
1200
800
wavenumber (cm-1)
200 γ
0 γ
- 0 kGγ
- 25 kGγ
- 50 kGγ
- 100 kGγ
- 200 kGγ

Figure 2

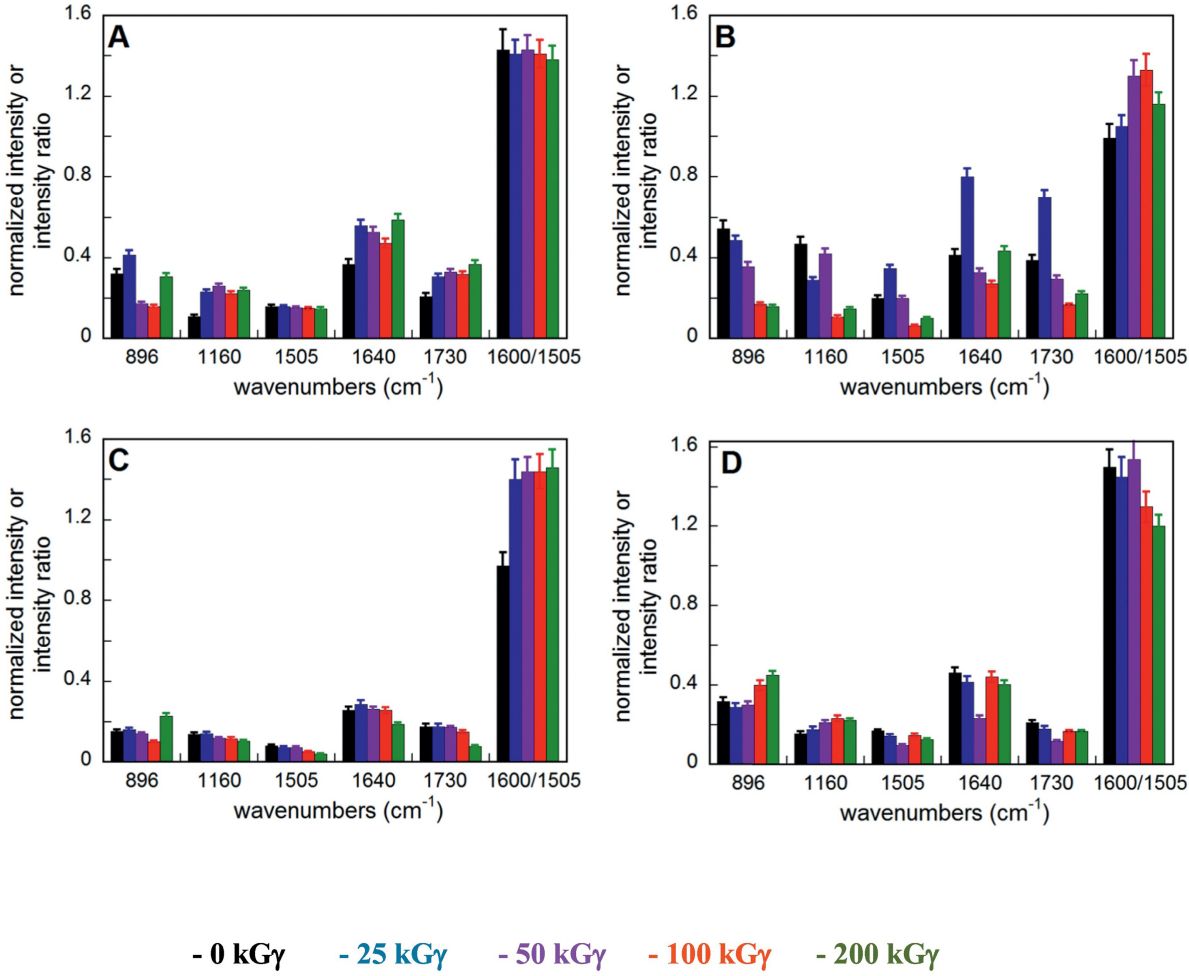
A
B
C
D
normalized intensity or intensity ratio
1.6
1.2
0.8
0.4
0
896
1160
1505
1640
1730
1600/1505
wavenumbers (cm-1)
- 0 kGγ
- 25 kGγ
- 50 kGγ
- 100 kGγ
- 200 kGγ

Figure 3

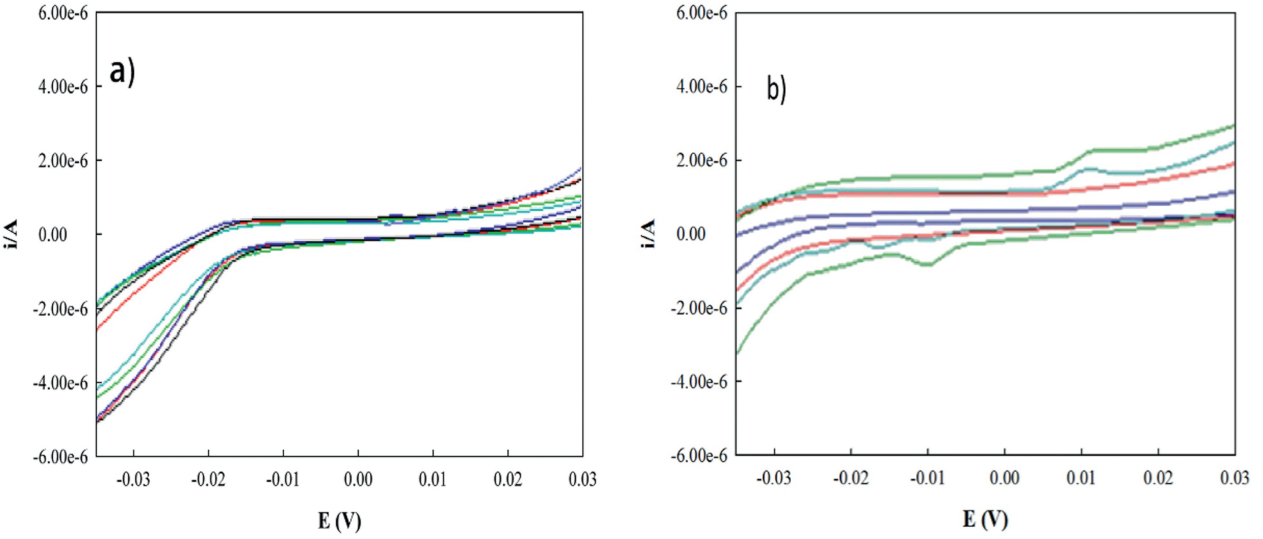
a)
b)
i/A
E (V)
6.00e-6
4.00e-6
2.00e-6
0.00
-2.00e-6
-4.00e-6
-6.00e-6
-0.03
-0.02
-0.01
0.00
0.01
0.02
0.03
- poplar
- durmast
- maple
- fir

Figure 4

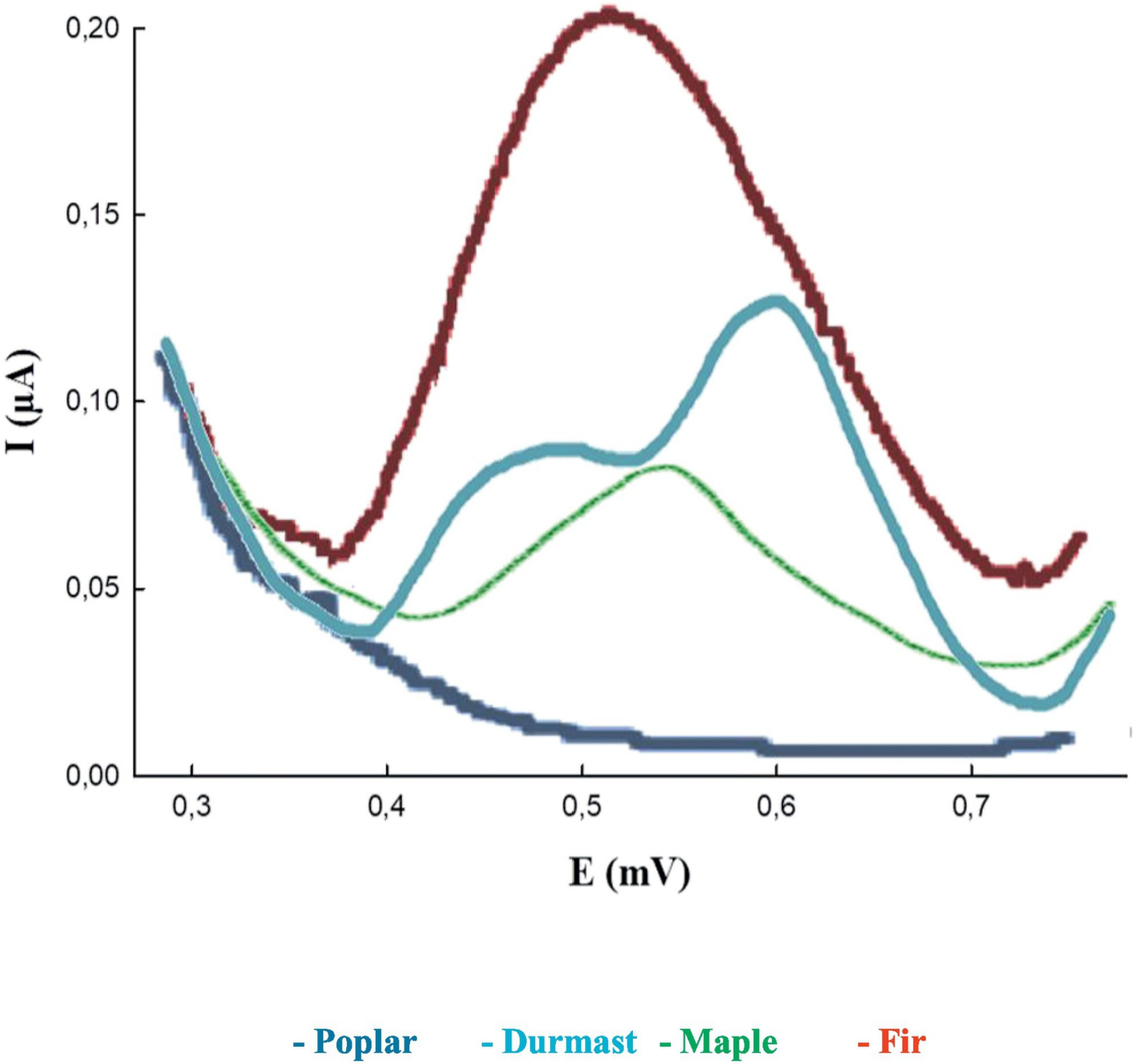
0,20
0,15
0,10
0,05
0,00
I (μA)
0,3
0,4
0,5
0,6
0,7
E (mV)
- Poplar
- Durmast
- Maple
- Fir

Figure 5

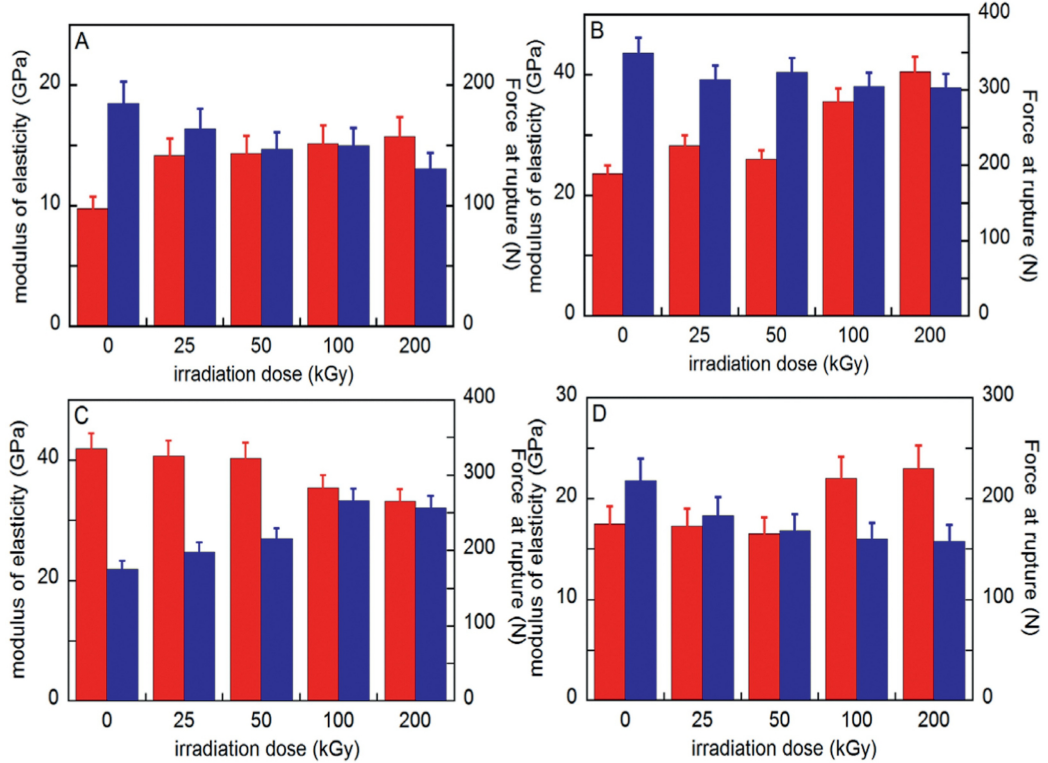
A
B
C
D
modulus of elasticity (GPa)
Force at rupture (N)
irradiation dose (kGy)
0
25
50
100
200
- Modulus of elesticity
- Maximum bending force before rupture

Figure 6

The chemistry of fossilization on Earth and Mars

Sean McMahon
(University of Edinburgh, UK)

The story of our world is written in the rocks. Turning over the stony pages, a trained geologist can read about mountains that rose and fell in the distant past, oceans that dried out in the sun, and continents that came together and drifted apart. The ground beneath us was shaped by processes like these over millions of years, and perhaps it is unsurprising that these epic shifts in the landscape should have left traces behind. But here and there, to our immense good fortune, the rocks yield something else: remains or traces of ancient life. If a good rock can be read like a good book, then a well-preserved fossil is like a finely wrought illustration, a vivid depiction of a fleeting moment in the life of the world. Fossils, whether on the scale of dinosaurs or individual molecules, provide our most decisive evidence for testing hypotheses about the abundance, diversity and evolution of life on Earth over the past three-and-a-half billion years. They are also our best hope for answering one of the most compelling questions in science: was there ever life on Mars?

How do fossils form?

There are many ways to make a fossil, but very few organisms fossilize; most simply rot away. Decay is driven by physical, chemical and biological agents, including the digestive and autolytic enzymes of the decaying organism itself. Aerobic bacteria rapidly destroy organic remains that are exposed to air, so burial under mud, silt or sand is a prerequisite for most styles of fossilization. After burial, new minerals can precipitate from groundwater inside and around the remaining structures, welding the sediment grains into a mould and filling any cavities left behind by decay. (Paradoxically, decay is often necessary for preservation to occur: the breakdown of organic matter favours mineral precipitation by changing chemical conditions and supplying mineral ions like sulphide and phosphate.) Finally, with deeper burial, compaction and further cementation by new minerals, soft sediment turns into hard rock, and the ephemeral stuff of life is converted into fossils that can last for millions or even billions of years.

Fossils vary enormously in their composition and level of detail, reflecting the complex and unpredictable play of biogeochemical interactions around decaying organic remains (Figure 1). There is a whole subdiscipline of palaeontology (*taphonomy*) dedicated to understanding the diverse ways in which fossils can form. Taphonomists often conceptualize fossilization as a contest or race between processes that tend to destroy biological information (decay) and processes that tend to secure it for posterity (preservation). Decay usually wins hands down. Admittedly, some biological materials are more resilient than others. Bones, teeth and shells lose their organic matrix long before their inorganic, crystalline components, which typically recrystallize after burial, forming more stable minerals while maintaining their original shape. Organic macromolecules vary widely in their resistance to decay. Nucleic acids break down fast, but lipids can be extraordinarily resilient, surviving for billions of years (as 'molecular fossils') as long as they are not exposed to high temperatures. Structural polymers like lignin, cellulose, collagen, keratin and chitin outlast other proteins and carbohydrates, but skin, muscles and other such 'soft parts' are still extremely rare as fossils. To preserve them, conditions must conspire to suppress decay for longer than usual, or minerals must precipitate unusually early and pervasively around the organism after (or even before) death. Even then, organic carbon preserved within fossils is typically altered by heat and pressure over time, gradually transforming into kerogen, petroleum, natural gas and graphite.

Why care about how fossils form?

There are at least four reasons why taphonomy matters to palaeontologists. First, the fossil record is not perfect. It tells an incomplete story, systematically biased in favour of certain biological materials, chemical conditions and physical environments. To fill in the gaps in the evolutionary timeline, we need to know what is likely to be missing from the fossil record and why. Second, to reconstruct the anatomy and physiology of ancient

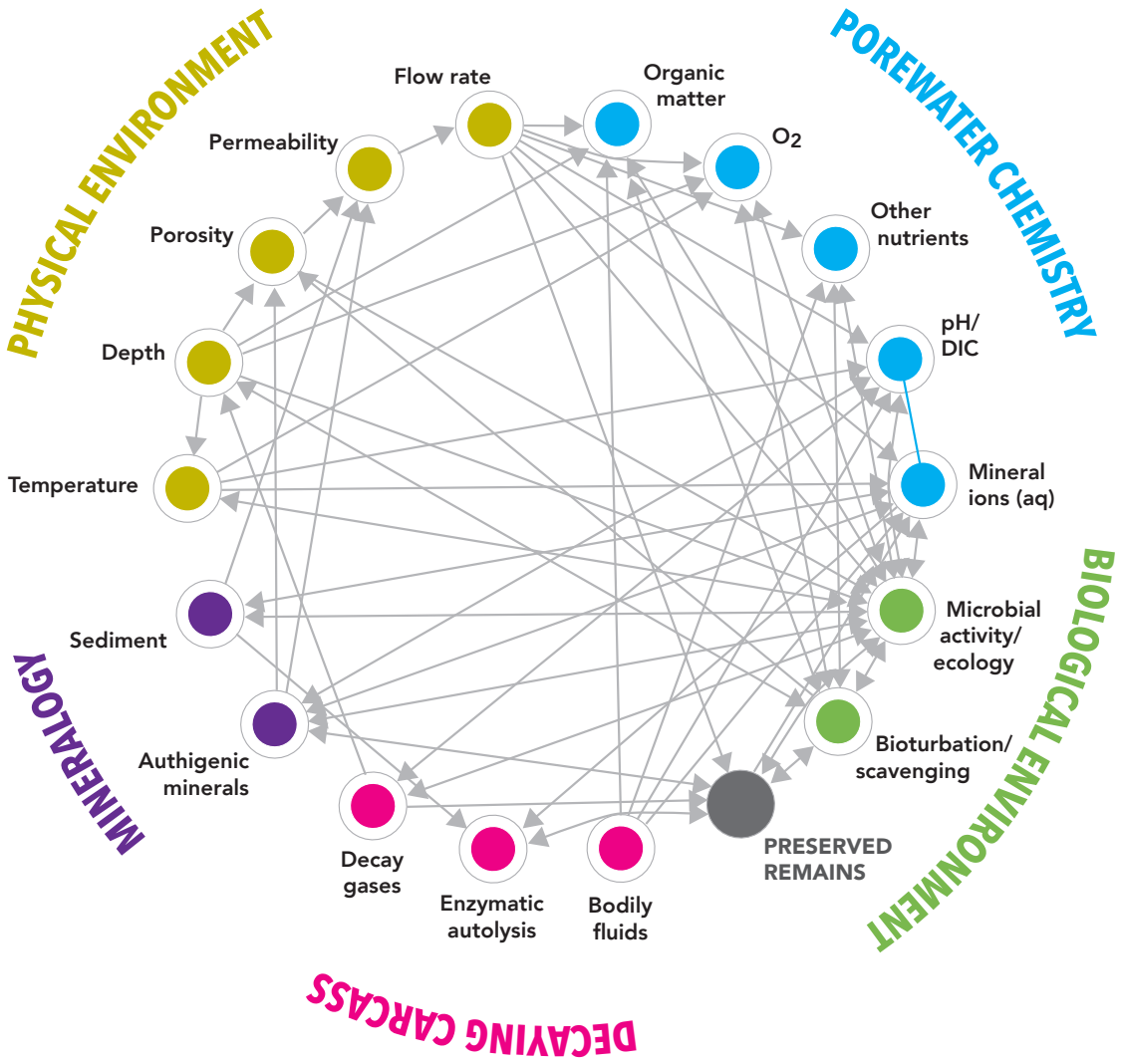

Figure 1. Schematic overview showing some of the interactions governing fossil preservation. Arrows indicate directions of influence. A carcass or microbial cell buried in sediment is a complex biogeochemical reactor that can behave unpredictably.
Figure designed with help from Victoria E. McCoy (University of Bonn)

organisms accurately from their fossils, we need to be able to compensate for the distortions and omissions produced during decay and mineral growth. Third, understanding what conditions are most favourable for fossil preservation allows us to optimize the search for the best-preserved fossils, which can provide unique insights into the physiology and ecology of extinct organisms. Fourth, understanding these conditions allows us to predict whether and how fossils would form in radically different environments — like those existing billions of years ago on Mars.

Why look for fossils on Mars?

Humans have speculated about life on Mars for hundreds of years, but the robotic missions of the last few decades have revealed the red planet to be a brutally inhospitable place. The low temperatures and pressures make water unstable on the Martian surface except where its freezing point is suppressed by toxically high concentrations of salts. Any organic matter lying around would soon be destroyed by a combination of oxidizing soil chemistry (including Fenton reactions) and intense ionizing radiation from space and the Sun, against which Mars' weak magnetic field and thin atmosphere offer very little protection. If there is life (as we know it) on Mars today, it would have to be restricted to deep sheltering niches underground, where geothermal heat could maintain a supply of liquid water. To find these hypothetical organisms would require drilling deep into the Martian subsurface, an impossible task with the technology (and budgets) currently available.

Between about four and three billion years ago, however, the surface of Mars was a much more hospitable environment. Ancient valley networks, exposed shorelines and sedimentary rocks — all preserved in

excellent condition because Mars lacks plate tectonics or forceful erosion — testify to the existence of an active water cycle on early Mars, which in turn implies higher temperatures and a thicker atmosphere. Intriguingly, conditions on Mars seem to have been most suitable for life at around the same time that life began on Earth. In my judgment, Earth's oldest convincing fossils are about 3.4 billion years old. Reports of fossil bacteria in meteorites from Mars have not stood up to scientific scrutiny, but there is experimental evidence to suggest that debris from asteroid impacts could have transported viable microorganisms from one planet to the other. Even if life originated only on Earth, it could still have spread to Mars, or *vice versa*.

Both NASA (the National Aeronautics and Space Administration) and ESA (the European Space Agency) have now committed billions of dollars to robotic rover missions that will search for physical or chemical remnants of life — fossils — in ancient Martian rocks. The long-term aspiration of both space agencies is to put these rocks into the hands of palaeontologists and geochemists back on Earth. To this end, NASA's Mars 2020 rover will collect its most promising finds and gather them together in one place. If these samples are deemed interesting enough to warrant the expense, they will be scooped up and returned to Earth by a purpose-built follow-on mission.

Clearly, understanding how and where fossils could have formed on Mars is critical to the success of these missions. Insights from taphonomy therefore have the potential to determine which landing sites are chosen, which routes the rovers take over the Martian surface, and which rocks they sample or collect for return to Earth.

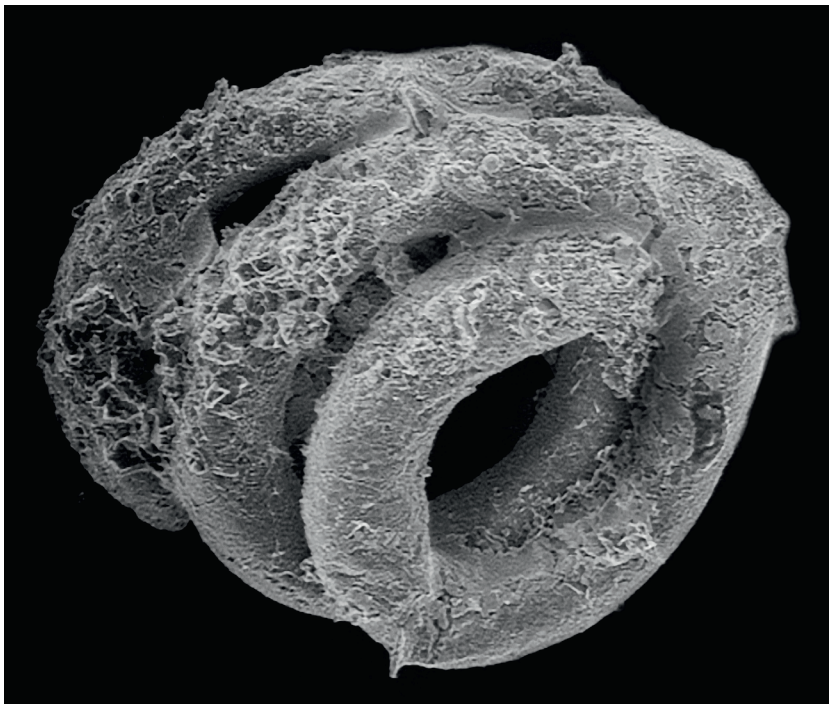

Figure 2. A spring-shaped phosphatic fossil cyanobacterium, *Obruchevella* (about 0.2 mm across), from 0.6 billion-year-old rocks in Mongolia.

Fossil microorganisms on Earth and Mars

By the time animals and plants arose on Earth, the surface of Mars had already been an icy wasteland for two or three billion years. Nobody, therefore, is looking for Martian dinosaur bones (sorry, Hollywood!). Instead, microbes like bacteria and archaea provide our best analogues for the kind of fossils we might hope to find on Mars. Such microorganisms dominated the Earth for most of its history—in many ways, they still do—and could have made a living in the anaerobic conditions on early Mars using photosynthesis or by catalysing redox reactions involving iron, sulphur and hydrogen. Fossil microbes are not especially rare on Earth, although most cannot be seen without scanning electron microscopes or polished slides for high-magnification optical microscopy. These techniques will not be available to rovers on Mars, so we won't know for sure if they've found fossil bacteria until we can get the samples back to Earth. We would be reasonably optimistic, however, if rovers on Mars found the macroscopic features that we associate with bacterial activity in ancient sediments on Earth, like fossilized gas bubbles or large convex-upward protrusions composed of fine laminations.

Cyanobacteria, the most important bacterial photosynthesizers on Earth, have a cellular fossil record stretching back over a billion years (Figure 2). These relatively large microorganisms are extremely abundant and commonly produce extracellular sheaths made of polysaccharides, which in some strains are highly resistant to decay. Under certain conditions, cyanobacterial sheaths have also been shown to facilitate the precipitation of minerals including carbonates and clays, which can encrust and preserve the cyanobacteria as fossils. Many other groups of bacteria share this ability to deposit minerals outside their cells for homeostatic purposes, making this is an important pathway by which bacteria can enter the fossil record — effectively fossilizing themselves.

Ultimately, however, most microbial fossils result from speedy entombment in minerals delivered by the environment. For example, geysers and hot springs can rapidly dump vast amounts of silica, a mineral which dissolves into hot water underground and precipitates as an amorphous mass in cooler conditions at the surface, trapping any organic remains within it (Figure 3). Amorphous silica is an excellent medium for preserving

Figure 3. El Tatio geyser field in Chile. The hot springs at this site discharge silica-laden water, forming fossiliferous rocks texturally similar to controversial deposits observed on Mars.

fossil cells at sub-micron resolution. It's also very common on Mars, mostly as a weathering product of ancient lava flows. NASA's Opportunity rover found a lot of silica in Gusev Crater, where its distribution and textural features are consistent with deposition in a geyser-like environment. At the time of writing, this locality is being considered as a possible landing site for NASA's Mars 2020 mission precisely because it could be a fossiliferous deposit. Other, less exciting interpretations of the silica haven't been fully ruled out, however, which makes this site a somewhat risky prospect.

Glorious mud

In my view, the most palaeontologically promising rocks on Mars are the lakebed mudstones — fine-grained, clay-rich, thinly layered rocks like those explored by NASA's Curiosity rover in Gale Crater (Figure 4; these rocks also turned out to be surprisingly rich in amorphous or very finely crystalline silica). By their very nature as the products of long-lived lakes, we know that these rocks formed in habitable environments. On Earth, many mudstones contain wonderfully preserved animals and plants, whose soft tissues appear to have been fortified by adsorptive interactions with clay particles and retained as thin carbonaceous films. Mudstones rarely contain fossil bacteria except for those with unusually robust cell walls or resistant sheaths, like cyanobacteria, although pervasive, early precipitation of silica would substantially improve the odds of preserving other kinds of microorganisms. More importantly, however, mudstones can preserve large amounts of ancient biological organic matter, even where structures like cells have broken down beyond recognition. The biological origin of this organic matter is revealed by the presence of molecular fossils: organic biomarkers, mostly derived from lipids like sterols or hopanoids.

As I remarked above, organic molecules would not fare well if exposed to the harsh conditions at the Martian surface. If entombed inside rocks, however, organic matter formed on early Mars could have survived for billions of years down to the present day. Indeed, using a miniaturized pyrolysis GC-MS instrument, the Curiosity rover has already been able to identify ancient organic matter within the four-billion-year-old mudstones in Gale Crater. Low yields and reactions with perchlorate inside the pyrolysis chamber have obscured the original composition of this organic matter, which may or may not have been biological. If future rovers visit similar rocks, they may settle the issue using more sensitive techniques. It could be a day to remember!

Figure 4. Four-billion-year-old lakebed mudstones on Mars, found by the Curiosity rover to contain organic matter

What can we do on Earth?

Our understanding of how fossils form on Earth — including much of the detail mentioned in this article — has been refined in recent decades by an experimental approach to the study of taphonomy. When it comes to soft tissues or microbes, the race between decay and preservation is often won in a matter of hours or days, not millions of years. This makes it possible to study these processes in the laboratory. A few workers, like Frances Westall and her colleagues at CNRS Orleans, have conducted taphonomic experiments using bacteria and archaea, artificially entombing them in silica, for example, to understand what controls the quality of silicified microfossils. In future, experiments like these will need to be adapted to take better account of the physical and chemical environments encountered on Mars over the past few billion years, such as anoxic CO_2-rich atmospheres, acidic brines, oxychlorine compounds and low temperatures. Future work addressing these conditions may provide further insights that can be used to guide us towards the first fossil to be identified on Mars. That long-anticipated discovery could be bacterial or even molecular in scale — but it would be another giant leap for humankind. ■

Further reading

- McMahon, S., Bosak, T., Grotzinger, J. et al. (2018) A field guide to finding fossils on Mars. Journal of Geophysical Research: Planets **153**, 1012–1040 (open access)
- Eigenbrode, J.L., Summons, R.E., Steele, A. et al. (2018) Organic matter preserved in 3-billion-year-old mudstones at Gale Crater, Mars. Science **360**, 1096–1101
- Parry, L.A., Smithwick, F., Nordén, K.K. et al. (2018) Soft-bodied fossils are not simply rotten carcasses–toward a holistic understanding of exceptional fossil preservation: exceptional fossil preservation is complex and involves the interplay of numerous biological and geological processes. Bioessays **40**, 1700167
- Westall, F. (1999) The nature of fossil bacteria: a guide to the search for extraterrestrial life. Journal of Geophysical Research: Planets **104**, 16437–16451
- Westall, F., Foucher, F., Bost, N. et al. (2015) Biosignatures on Mars: what, where, and how? Implications for the search for Martian life. Astrobiology **15**, 998–1029

Sean McMahon is a Marie Skłodowska-Curie Fellow at the UK Centre for Astrobiology, University of Edinburgh. He is a geobiologist with broad interests in ancient microbes and their fossil record and his work is funded by the European Union's Horizon 2020 research and innovation programme under grant agreement No. 747877.
Email: sean.mcmahon@ed.ac.uk. Twitter: @SeanHMcMahon

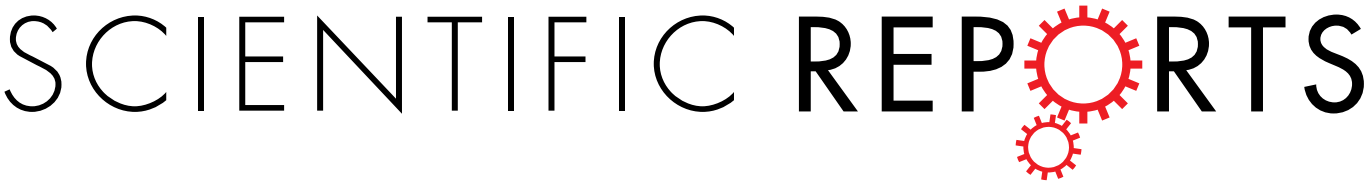

OPEN

3D Maps of Mineral Composition and Hydroxyapatite Orientation in Fossil Bone Samples Obtained by X-ray Diffraction Computed Tomography

Received: 25 January 2018
Accepted: 20 June 2018
Published online: 03 July 2018

Fredrik K. Mürer[1], Sophie Sanchez[2,3,4], Michelle Álvarez-Murga[3], Marco Di Michiel[3], Franz Pfeiffer[5,6], Martin Bech[7] & Dag W. Breiby[1,8]

Whether hydroxyapatite (HA) orientation in fossilised bone samples can be non-destructively retrieved and used to determine the arrangement of the bone matrix and the location of muscle attachments (entheses), is a question of high relevance to palaeontology, as it facilitates a detailed understanding of the (micro-)anatomy of extinct species with no damage to the precious fossil specimens. Here, we report studies of two fossil bone samples, specifically the tibia of a 300-million-year-old tetrapod, *Discosauriscus austriacus*, and the humerus of a 370-million-year-old lobe-finned fish, *Eusthenopteron foordi*, using XRD-CT – a combination of X-ray diffraction (XRD) and computed tomography (CT). Reconstructed 3D images showing the spatial mineral distributions and the local orientation of HA were obtained. For *Discosauriscus austriacus*, details of the muscle attachments could be discerned. For *Eusthenopteron foordi*, the gross details of the preferred orientation of HA were deduced using three tomographic datasets obtained with orthogonally oriented rotation axes. For both samples, the HA in the bone matrix exhibited preferred orientation, with the unit cell *c*-axis of the HA crystallites tending to be parallel with the bone surface. In summary, we have demonstrated that XRD-CT combined with an intuitive reconstruction procedure is becoming a powerful tool for studying palaeontological samples.

X-ray computed tomography (CT) based on attenuation contrast and/or phase contrast is increasingly used in palaeontology, owing to its ability of non-destructively providing internal 3D images of opaque materials[1,2]. In rare cases, the muscles are preserved, allowing their structure to be directly investigated[3]. The usual situation is however that soft tissues are not preserved, and the musculature of extinct animals can only be retrieved from the geometry and composition of the bone where the muscles once were attached. In extant vertebrates, muscles attach to the bones via collagen fibres embedded in the bone matrix to form muscle attachments (entheses)[4,5]. Muscle collagen fibres can be distinguished from the collagen fibres of the bone matrix based on their orientation, as the muscle collagen fibres are embedded in the bone matrix with an angle ranging from 0 to 60 degrees with respect to the bone surface normal[6,7]. Collagen fibres are positively birefringent structures and their orientation can be revealed using polarised light[8]. As muscle fibres are progressively embedded in the bone matrix during the animal development, they also mineralize[9]. The associated hydroxyapatite (HA) crystallites are negatively

[1]Department of Physics, Norwegian University of Science and Technology, Høgskoleringen 5, 7491, Trondheim, Norway. [2]Science for Life Laboratory and Uppsala University, Department of Organismal Biology, Evolutionary Biology Centre, Norbyvägen 18A, 75236, Uppsala, Sweden. [3]ESRF – The European Synchrotron, 71 Avenue des Martyrs, 38000, Grenoble, France. [4]Sorbonne Université – CR2P – MNHN, CNRS, UPMC, 57 rue Cuvier, CP38, F-75005, Paris, France. [5]Lehrstuhl für Biomedizinische Physik, Physik-Department & Institut für Medizintechnik, Technische Universität München, 85748, Garching, Germany. [6]Department of Diagnostic and Interventional Radiology, Klinikum rechts der Isar, Technical University of Munich, 81675, München, Germany. [7]Department of Medical Radiation Physics, Clinical Sciences, Lund University, 22185, Lund, Sweden. [8]Department of Microsystems, University of South-Eastern Norway, 3184, Borre, Norway. Martin Bech and Dag W. Breiby contributed equally to this work. Correspondence and requests for materials should be addressed to D.W.B. (email: dag.breiby@ntnu.no)

birefringent, and their orientation can also be revealed using polarised light in both extant and extinct physically sectioned specimens[10].

Studies done by transmission electron microscopy (TEM) of bone from extant animals have shown that the HA crystallites are platelet-shaped and arranged in parallel layers aligned along the collagen fibre axis[11]. Research indicates that the diagenesis, i.e. the process in which biological materials degrade during fossilisation, alters the morphology of HA in such a way that needle-shaped crystallites in addition to platelet-shaped crystallites can be found[11]. However, there is strong evidence that the orientation of the HA crystallites is preserved during fossilisation[12,13], which opens for investigating the bone microstructure and associated soft tissues, such as muscles in fossils[6,7].

Until recently, reconstructions of fossil musculature have been based mainly on the interpretation of muscle scars at the surface of fossil bones[14,15]. Polarised light micrography[6] and (propagation-based) phase contrast micro-CT[7] have been used to map muscle insertions on fossilised bone samples. However, they both have important limitations. In order to extract the information of HA orientation using polarised microscopy, the sample needs to be sectioned into thin slices, and thus destroyed. Conventional CT has insufficient resolution to study the nanoscale mineral orientation. High-resolution micro- or nano-CT, even if it may reach the appropriate resolution for studying crystallite shapes, has a limited field of view of about 1 mm at high resolution, which is insufficient for getting an overview of the muscle attachments in vertebrate fossil bones[16]. New approaches are therefore desired to extract the 3D orientation of the HA without damaging the fossils.

Bragg peaks seen in X-ray diffraction (XRD) contain information about atomic-scale crystal structures including the orientation of the crystal lattice[17]. XRD allows information to be gathered about the presence and concentration of different materials, as well as their morphology on the micro and nanoscale. These facts have made XRD the undisputed technique for resolving crystal structures, and for determining how materials respond to various external stimuli under *in-situ* conditions[17]. XRD is non-destructive, where other relevant techniques like transmission electron microscopy (TEM) or scanning electron microscopy (SEM) require destructive sample sectioning[12,18]. Fossil samples have previously been studied with XRD, however limited to powder diffraction[19,20], which does not allow spatially resolved information about the mineral concentration nor crystallite orientation to be obtained.

New X-ray sources, detectors, and optics, combined with increased computing power, have led to a range of new scattering and imaging methods allowing spatially resolved structural information to be obtained from macroscopic bulk samples using X-ray CT with unconventional contrast mechanisms. Examples of these methods are small-angle X-ray scattering computed tomography (SAXS-CT)[21,22], coherent diffractive imaging (CDI)[23–25] and ptychography[26–28]. Recently, several approaches to spatially resolving material *orientations*, known as X-ray *vectorial imaging*[16,29,30], have been developed, recently even with magnetic contrast[31].

The combination of XRD and computed tomography (CT), often referred to as XRD-CT, denotes an emerging family of techniques where the information obtained from the diffracted radiation, rather than beam attenuation, is used to form contrast for 3D tomographic reconstructions[32]. XRD-CT is not yet commonly available for routine studies, but the technique is increasingly used in the materials sciences. The first publication using XRD-CT dates back to the late 1980s[32], but because of the increased computational power and fast read-out low-noise detectors available today, more data can now be acquired and processed, which allows larger sample volumes to be measured and higher resolution images to be acquired. The fact that orientation information is contained in the scattering signal, is the salient feature that opens for 3D reconstructions of material *orientation*. Several publications employing the XRD-CT technique already exist, and frequently reported limitations include that the samples need to either consist of large crystallites compared to the resolved voxel size[33,34], or a large number of isotropically oriented crystallites must be contained in each voxel volume[35].

In this article, we report on the use of XRD-CT to gain insight into the microstructure of two fossil bones. We demonstrate for the first time that both the spatial distribution of minerals and the 3D orientation of HA can be obtained without damage to the fossils. Our XRD-CT approach opens new opportunities for non-destructive extraction of microstructural information from mineralized biological samples.

Samples were prepared from three bones: 1) The humerus of an extant tetrapod, *Desmognathus quadramaculatus*, for which the identification of a muscle insertion was known. The humerus was sectioned at the location of a muscle insertion[2,7], and raster-scanning XRD mapping was performed on a 50 µm thin section to validate the concept of visualising changes of HA orientation at the site of a muscle insertion in a fresh bone. 2) The tibia of a fossil specimen, the 300-million-year-old *Discosauriscus austriacus*, where the location of a muscle insertion was known from observations using polarised light[30]. An XRD-CT measurement was made in the region of the muscle insertion (Fig. S1a), confirming that the diagenesis did not destroy the crystal structure of HA, which is crucial for our XRD-CT approach to work. 3) The humerus of a 370-million-year-old lobe-finned fish *Eusthenopteron foordi*[36], which has remained un-sectioned but for which we know there are muscle insertions based on local high-resolution images produced by phase-contrast micro-CT[7]. The humerus of *Eusthenopteron foordi* has a complex shape and microanatomy[37] which is representative of most fossil bones. To the best of our knowledge, this is the first time 3D XRD-CT has been used for non-destructive structural analysis on a complex-shaped fossil bone.

XRD-CT reconstruction procedure. To understand the procedures we used for XRD-CT measurements and reconstruction, it is instructive to first reconsider the fundamentals of attenuation-CT, shown for parallel beam geometry in Fig. 1a. For a collimated monochromatic X-ray beam propagating in the z-direction, one can quantitatively describe the X-ray attenuation using Lambert-Beer's law,

$$I_t(x,\ y,\ \omega) = I_0 \exp\left(-\int \mu(x'(\omega),\ y',\ z'(\omega))ds\right) \quad (1)$$

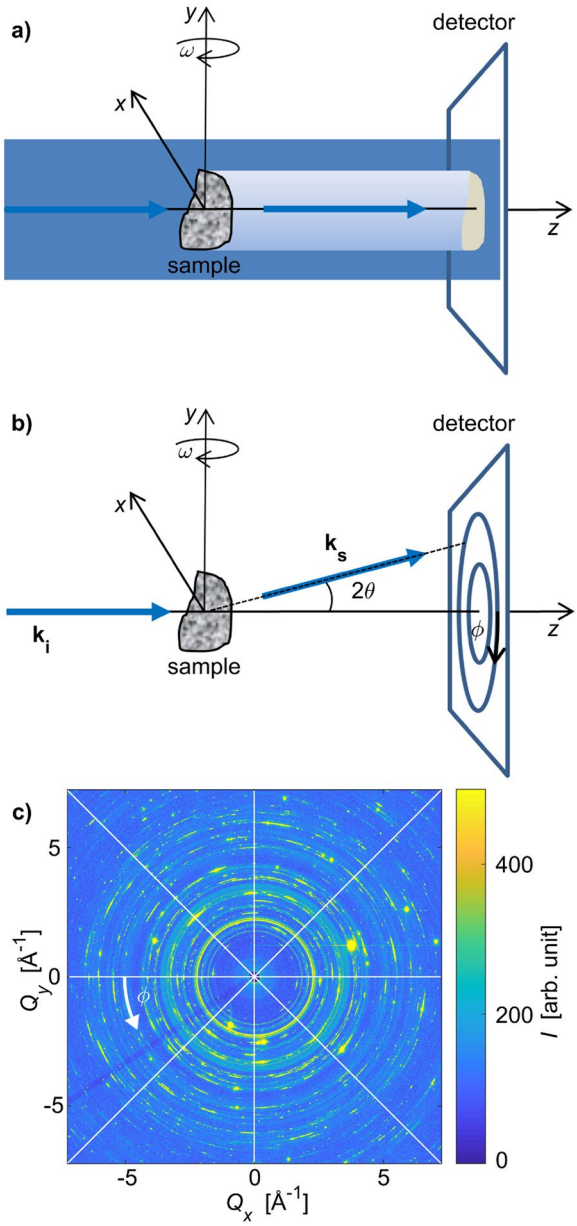

Figure 1. (**a**) Sketch of a parallel-beam attenuation-based CT setup with a rotating sample. A wide beam floods the sample, and the transmitted beam intensity is recorded on a detector. Through tomographic reconstruction the spatially resolved density of the sample is obtained. (**b**) Sketch of a generic XRD-CT setup as employed in our experiment. The collimated pencil beam from the synchrotron source with wavevector $\mathbf{k}_i$ enters the sample from the left. A fraction of the incoming beam is elastically scattered by the sample, and exits on the right as a scattered beam with wavevector $\mathbf{k}_s$, while the remaining un-scattered photons exit the sample as a transmitted beam which is blocked by a beam-stop. Diffraction patterns were measured for different combinations of sample positions (x, y) and projection angles ω. (**c**) An example of a recorded diffraction pattern from the humerus of *Eusthenopteron foordi* (with linear intensity scale). Continuous Debye-Scherrer diffraction rings originating from HA can be seen, while the scattering from barite, calcite, quartz and pyrite is seen as bright spots. The white lines indicate sectioning of the diffraction patterns into azimuthal sections, used for tomographic reconstruction. 8 sectors are indicated for illustration purposes, while 64 sectors were used in the actual analysis. The beam stop support is seen as a dark line in the lower left region.

Here $I_t(x, y, \omega)$ is the transmitted beam intensity, I_0 the incoming beam intensity, $\mu(x', y', z')$ the spatially resolved linear attenuation coefficient[38]. x, y and z are coordinates in the laboratory system (Fig. 1a), while x', y' and z refer to the internal sample coordinates. The sample coordinate system rotates during tomography with the sample projection angle ω, keeping $y' = y$. The integral is taken over the distance through the sample for a given ray. The transmitted intensity $I_t(x, y, \omega)$ of the X-ray beam through the sample is measured for a wide range of projection angles ω, ideally covering 180°. The notation emphasizes that for each tomographic projection angle

ω, the intensity is measured as a function of position (x, y). To reconstruct $\mu(x', y', z')$ from the measured data, the fast and robust filtered back-projection (FBP) algorithm, which is based on the inverse Radon transform, is often used[38].

In XRD-CT, the measured *diffracted* intensities, rather than the reduction in intensity (attenuation) of the direct beam, are used to reconstruct the scattering characteristics of each voxel in the sample volume (or cross-sectional area). Using carefully designed criteria (cf. SI), we extracted information from each 2D diffraction pattern using what we coin descriptors $I_{\text{descriptor}}(x, y, \omega)$. These descriptors are designed to return one single scalar value for each combination of (x, y, ω), which can then be fed into the FBP algorithm. Challenges arise because the scattering signal from each voxel volume in the sample changes with the projection angle. For retrieving the spatial distribution of minerals we define the descriptor $I^{\text{hkl}}_{\text{isotropic}}$ as the integrated intensity over all ϕ (Figs. 1b,c and S2) for a given diffraction lattice plane family *{hkl}* (i.e. a given scattering vector length Q). For the minerals being present in the bone samples with only few and large crystallites, resulting in tomograms with streak artefacts when reconstructing with the FBP algorithm, it proved useful to add several Bragg peaks for the composition analysis. Conversely, because the HA crystallites turned out to be small, numerous, and with wide orientation distributions, the descriptor for determining the spatial distribution of HA could be based on any of the HA Bragg peaks. The 002_{HA} reflection was selected for texture analysis because it has an easy interpretation as the unique axis of the hexagonal unit cell. We further define the descriptor I_{total} as the integrated intensity over all ϕ and Q, which is sensitive to the presence of any scattering compound in the sample.

The directional information contained in a diffraction pattern can be used to infer the orientation of the scattering mineral crystals. Two descriptors were designed to estimate the HA crystallite orientation, based on measurements with one or three tomography axes (Fig. S1). The single-axis approach was to first reconstruct the location of the HA crystallites based on the *meridional* $I_{||}$ and *equatorial* $I_{\perp}$ scattered intensities separately (cf. SI). Each descriptor yields its separate tomogram, showing the corresponding relative scattering of the HA. Because the HA was only weakly anisotropic, these tomograms were at first glance similar, but numerical comparisons indicated regions with a difference in the vertical and horizontal scattered signal. It proved useful to define an *orientational parameter* κ by

$$\kappa = \frac{I_{||} - I_{\perp}}{I_{||} + I_{\perp}} \tag{2}$$

to quantify orientation information. The other, multiple-axis, method of determining the HA crystallite orientation was to do several (here: three) full tomography scans with the sample mounted in different orientations with respect to the tomographic rotation axis. $I_{||}$ from a given location (voxel) in the sample will remain essentially invariant during sample rotation, which is a requirement for tomographic reconstructions using FBP. Having measured the sample with three orthogonal orientations, giving three different tomograms each based on $I_{||}$, gives the possibility of estimating an approximate *vectorial tomogram*, with one dominant HA crystallite orientation assigned to each of the voxels. For a more detailed explanation, cf. SI.

Results

Results for the extant reference and the two fossil samples are presented. Both fossil samples, the tibia from *Discosauriscus austriacus* and the humerus from *Eusthenopteron foordi*, contained minerals of different crystallite sizes. The HA crystallites were small (compared to the reconstructed voxel size) and numerous, with many crystallites satisfying the diffraction condition simultaneously, regardless of sample position and orientation. The other minerals, secondarily present in the bone due to the fossilisation, had larger crystallites, giving rise to bright spots in the diffraction patterns (Fig. 1c). Consequently, we could derive composition maps for all minerals, while for HA, also orientational maps indicating the dominant orientation could be obtained.

Scanning XRD of an extant salamander bone slice showing oriented HA crystallites. A 50 µm thin section made at midshaft in the humerus of the extant salamander *Desmognathus quadramaculatus* was studied to serve as a benchmark for the subsequent studies of fossil samples, demonstrating that the presence and orientation of HA in the vicinity of muscle attachments can be identified using XRD. Comparing Fig. 2a,b, it is apparent that polarised microscopy[8] reveals a change of the collagen structure at the muscle attachments. The raster-scanning XRD measurement of the physically cut thin slice shown in Fig. 2e demonstrates that the orientation of the HA associated to the collagen fibres is indeed markedly different at the muscle attachment. Precisely, observing this structural modification in the diffracted signal suggests that XRD-CT can be used to study muscle attachments also in fossilised samples, which is the prime motivation for this study. Figure 2f shows the size and radial orientation of extrinsic fibres at the location of a muscle attachment, as studied with phase-contrast CT. It is important to note that even though phase contrast CT measurements resolve the bone structure to high detail, these images do not contain information about the HA orientation.

2D XRD-CT of the tibia of *Discosauriscus austriacus* showing oriented HA crystallites. The tibia of *Discosauriscus austriacus* (Fig. 3a) was chosen as a first fossil sample for observing muscle attachments because it has a simple long-bone shape. This gives a uniaxial distribution of the HA crystallites with the *c*-axis tending to be parallel to the long axis, except in the vicinity of muscle attachments. XRD-CT and images of thin sections, taken with polarized light, were compared on this fossil bone to check whether the diagenesis modifies the crystal structure of HA, which would alter the diffraction signal. A thin section was made at midshaft[39] (Fig. 3a) where a muscle insertion could be visualised using polarised light (Fig. 3b). A 2D XRD-CT measurement (a single cross section) was obtained on the remaining half of the tibia embedded in polyester resin (Fig. S1). Bragg peaks corresponding to HA, as well as a broad scattering feature in Q corresponding to the surrounding amorphous resin,

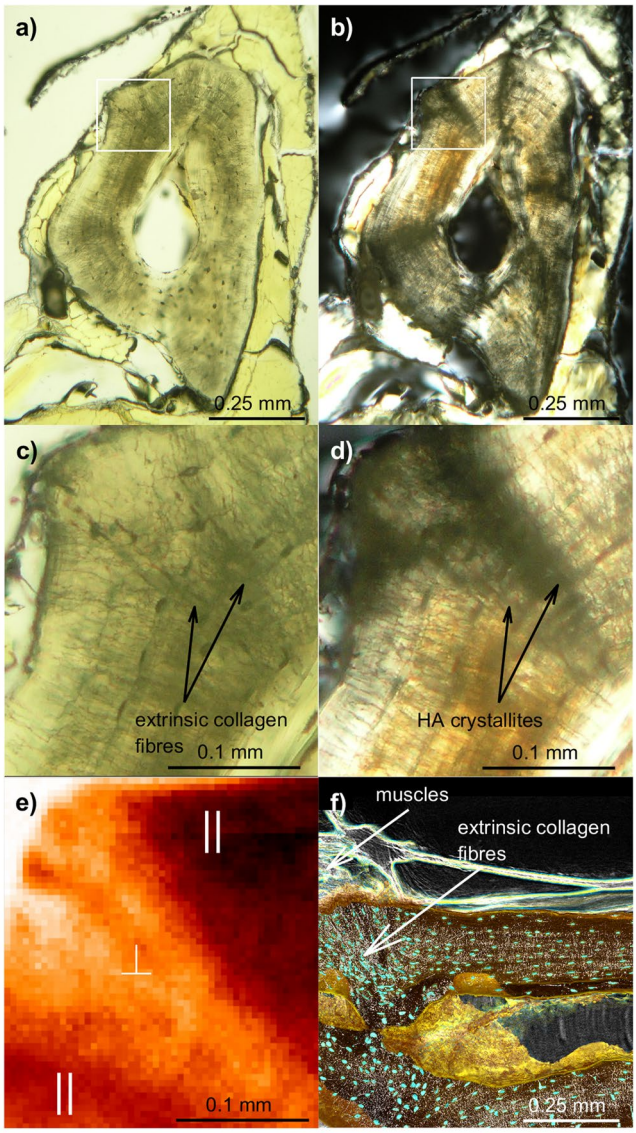

Figure 2. Humerus of the extant salamander *Desmognathus quadramaculatus*. (**a**,**b**) Natural and polarised light micrographs of a physically cut cross section through the sample, respectively, showing the region where the raster-scanning XRD map in (**e**) was made. (**c**,**d**) Details of the regions in (**a**) and (**b**), respectively. The arrows in (**c**) and (**d**) indicate locations of extrinsic collagen fibres and HA crystallites associated with muscle attachments. (**e**) Raster-scanning XRD map of the area indicated with a white rectangle in (**a**,**b**) and zoomed in (**c**,**d**), demonstrating that there is texture of the 002_{HA} reflection which can be mapped by XRD. Regions with either dominating meridional (out-of plane) diffraction or equatorial (in-plane) diffraction are marked by $\parallel$ or $\perp$, respectively. In other words, brighter hues of red correspond to the HA *c*-axis being more inclined with respect to the long-axis of the bone. (**f**) Longitudinal phase-contrast CT section, clearly showing the presence of extrinsic fibres at the location where muscles attach to the bone surface (indicated by an arrow).

were indexed and used for tomographic reconstructions (Fig. 3c–f). HA in the bone and resin around the bone are distinctly visualized, illustrating how XRD-CT allows accurately mapping out regions containing different compounds.

The gross orientation of the HA crystallites in the tibia diaphysis of *Discosauriscus austriacus* was obtained by comparing tomograms reconstructed separately from the meridional (vertical) descriptor $I_{\parallel}$ and the equatorial (horizontal) descriptor $I_{\perp}$. Note that albeit $I_{\perp}$ does not fulfil the Bragg condition for all sample rotations (as the meridional descriptor $I_{\parallel}$ does), the horizontal scattering still clearly provided visible image features (Fig. 3d). As seen, the vertical scattering is more intense than the horizontal scattering, due to the preferred orientation of the HA crystallites. A map of the orientation parameter κ (Equation 2) indicates that the position of muscle insertions in the bone sample coincides with the region of minimum difference in $I_{\perp}$ and $I_{\parallel}$ (Fig. 3e), as supported by a physically cut slice of the sample made in the same region viewed under polarised light (Fig. 3b).

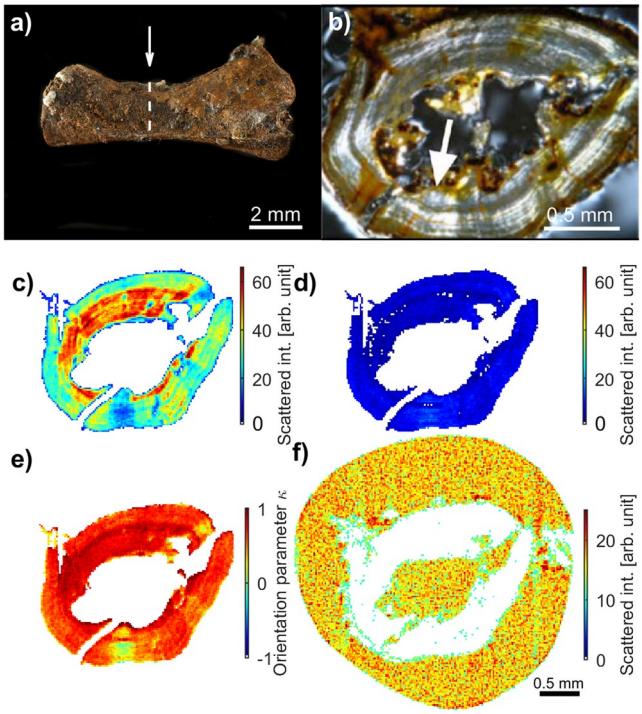

Figure 3. Tibia of the fossil tetrapod *Discosauriscus austriacus* (DE KO 58). (**a**) Photograph of the sample studied before sectioning. The arrow indicates the location of the cross-section measured with polarised light and XRD-CT. The photograph is provided by P. Loubry. (**b**) Polarised light micrograph of the physically-cut tibia cross section shown in (**a**). The arrow indicates the position of one of the muscle attachments, which corresponds to the region of maximum orientation contrast in the XRD-CT data, cf. (**e**). (**c**–**f**) *Vectorial* XRD-CT tomograms of the cross section in (**a**). (**c**) Tomograms based on $I_{||}^{002\mathrm{HA}}$ and (**d**) $I_{\perp}^{002\mathrm{HA}}$ (**e**) Normalized difference of the tomograms in (**a**) and (**b**), by using the orientation parameter κ (Equation 2). (**f**) Tomogram based on $I_{\mathrm{isotropic}}^{\mathrm{resin}}$ for the amorphous resin signal.

3D XRD-CT of the humerus of *Eusthenopteron foordi* showing the location of minerals. For the humerus of *Eusthenopteron foordi*, we performed three full XRD-CT measurements by laterally raster-scanning the whole sample for a large number of projection angles (cf. Methods). Bragg peaks corresponding to HA, barite, calcite, quartz and pyrite were indexed. Figure 4 shows a 3D mapping of the spatial mineral distribution in the humerus of *Eusthenopteron foordi*. Reconstructed tomograms based on $I_{\mathrm{isotropic}}$ for HA, barite, calcite and quartz are visualized separately, all with a surrounding semi-transparent region corresponding to a tomogram based on I_{total}. The pyrite signal was too weak to give reliable tomograms. Note how the spatial distributions of the various minerals are complementary to each other, jointly filling the 3D region constituting the sample.

A cross-section of the reconstructed compositional XRD-CT tomograms (Fig. 4f) is shown in Fig. 5a. The total scattered signal I_{total} is shown in Fig. 5b. A phase-contrast tomogram is shown in Fig. 5c for comparison. Regions containing different minerals have been labelled, and albeit having much higher resolution, the locations of the different minerals in the sample are qualitatively consistent with what is found through the XRD-CT analysis. The HA crystallites are located in the cortical and cancellous bone, while the quartz covers large regions inside the rock matrix, in-between bony trabeculae. There are also small regions of barite (Fig. 4c), matching what is seen in the XRD-CT tomograms. The determination of the locations of pyrite could not be ascertained in the XRD-CT measurements, due to diffraction peak overlap.

3D orientation of HA in the humerus of *Eusthenopteron foordi* revealed by vectorial XRD-CT. With three XRD-CT datasets obtained at orthogonal orientations (axes labelled **y1**, **y2**, and **y3** in Fig. 6) for the humerus of *Eusthenopteron foordi*, the spatially resolved preferred orientation of HA could be estimated. The meridional descriptor $I_{||}^{002\mathrm{HA}}$ for selecting intensity was applied to the 002_{HA} diffraction peak, giving for each of the three datasets an independent vectorial 3D tomogram emphasizing the regions having the highest density of HA crystallites oriented with the unit cell *c*-axis predominantly parallel to the actual tomographic axis. These tomograms are presented in Figs. 6 and 7, demonstrating that the *c*-axis of the HA unit cell tends to follow the external surface of the fossil bone, corroborating earlier reports[9]. As for the compositional tomograms, it gives credibility to the reconstruction algorithm that the tomograms independently show continuous regions that are complementary to each other.

A closer investigation of a 2D section of the humerus of *Eusthenopteron foordi* is given in Fig. 7, comparing orientation maps obtained using the single-axis XRD-CT method (with the tomographic axis perpendicular to the section, i.e. proximal) to the multiple-axis (three) orthogonal XRD-CT scans. The corresponding section is

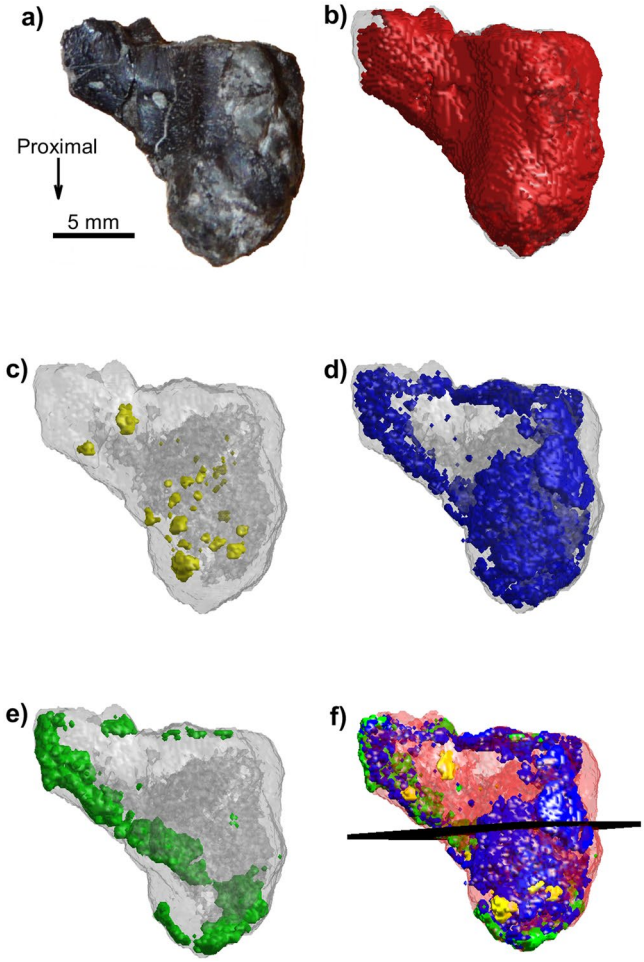

Figure 4. Humerus of the fossil lobe-finned fish *Eusthenopteron foordi* (NRM P246c) in mesial view. (**a**) Photograph of the sample studied. (**b**–**f**) 3D compositional tomograms of different minerals. (**b**) HA (red), (**c**) barite (yellow), (**d**) calcite (blue), (**e**) quartz (green). The grey shaded region in (**b**–**e**) corresponds to the total scattered signal I_{total} (integrated over the whole detector). Notice how the HA volume overlaps almost completely with the volume reconstructed by the total scattered signal. (**f**) Combined tomograms of all materials in (**b**–**e**), using the same colour coding, with HA semi-transparent for increased visibility. The plane plotted in the middle of the sample gives the location of the cross section shown in Fig. 5.

marked by a plane in Fig. 6e,f. Figure 7d shows the bone reconstructed from three datasets using $I_{||}$ for the 002_{HA} reflection, i.e. a 2D version of the 3D figures in Fig. 6. As can be seen in Fig. 7d, the dominating HA orientation varies in the surrounding cortical bone, thereby reflecting both the orientation of the HA in the bone matrix and the HA associated to the extrinsic fibres of the muscle insertions. HA in the spongiosa in the middle of the 2D section seems to have a preferred orientation along the bone axis (proximal). For generating the orientation map in Fig. 7c, we used the orientation parameter κ (Equation 2), with the additional requirement that the intensity along one direction should be at least 30% higher in one direction than the others, or otherwise the scattering was considered isotropic. The results from the single- and multiple-axes approaches are seen to be consistent, with the latter approach of course giving additional in-plane information. A comparison of Fig. 7c,d exhibits a gratifying similarity of the regions consisting of HA crystallites oriented with the *c*-axis out of the 2D section plane. One limitation of using a single tomographic dataset is a reduced ability at distinguishing between dominating horizontal scattering, i.e. crystallite orientation in the 2D section plane, and isotropic scattering.

Discussion

XRD-CT allows retrieving spatially resolved mineral identification and orientation information of semi-crystalline regions from non-destructive diffraction experiments. The diffraction contrast underlying XRD-CT thus provides information that cannot be obtained from conventional tomography. For the first time this method was applied, with success, to fossil hard tissues.

Using polarised light microscopy and scanning-XRD we demonstrated on a known muscle insertion in a physically cut thin slice of cortical bone from an extant salamander (Fig. 2) that the orientation of HA at muscle insertions could be mapped. We further showed that XRD-CT with a voxel size of 20 μm can be applied to fossil bones to map their muscle insertions. Indeed, a muscle insertion, previously identified using polarised light, could be observed in the tibia diaphysis of *Discosauriscus austriacus* by XRD-CT (Fig. 3). Significant equatorial

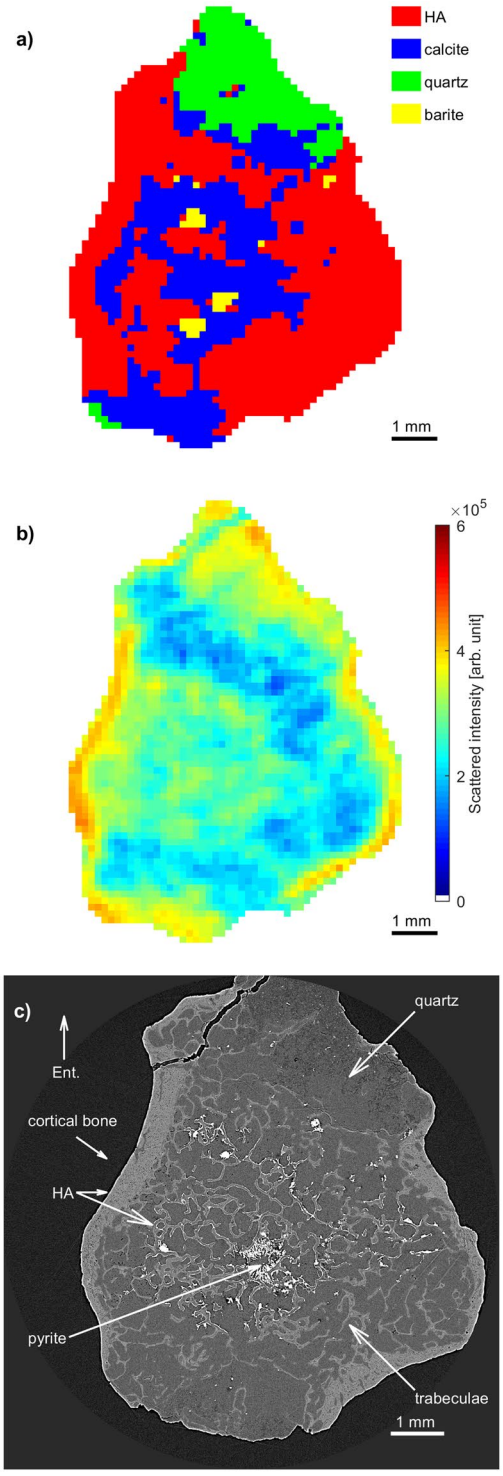

Figure 5. 2D cross sections of *Eusthenopteron foordi* (NRM P246c) CT measurements, midshaft of the humerus, corresponding to the plane indicated in Fig. 4f. (**a**) XRD-CT cross section showing the dominating mineral present at each voxel. (**b**) XRD-CT cross section based on I_{total}, being a rough estimate of the density of scattering material. (**c**) Phase contrast tomographic cross-section. Regions containing HA (cortical and trabecular bone), barite, quartz and pyrite have been labelled. Abbreviation: Ent., entepicondyle.

scattering ($I_{\perp}$) was observed, and tomograms of the diffracted signal showed explicitly that this scattering originated from regions that coincided with a muscle attachment. In other words, XRD-CT with a single tomography axis can therefore be able to locate the position of muscle attachments in fossil bones.

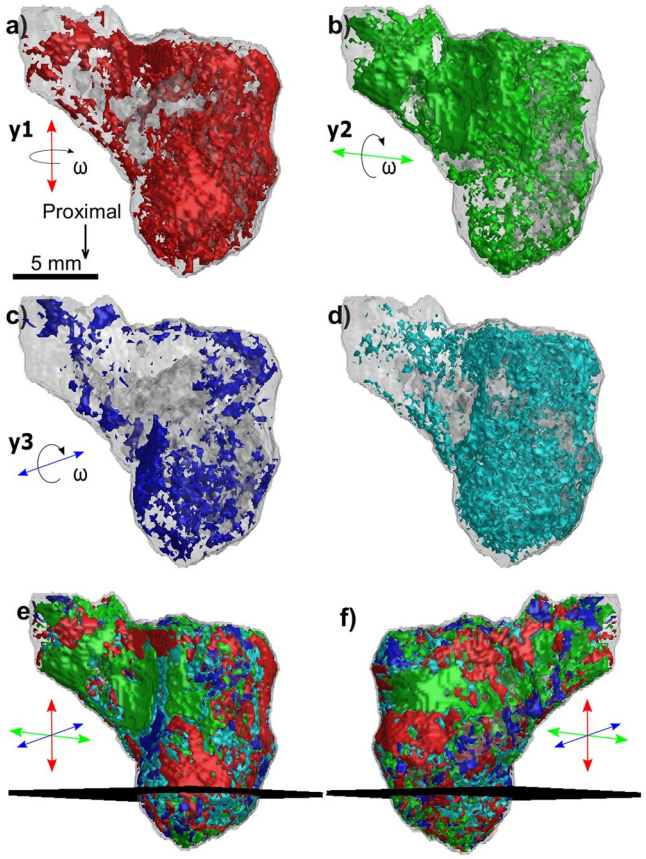

Figure 6. HA crystallite orientation in the bone of the humerus of *Eusthenopteron foordi* (NRM P246c) in mesial view. (**a**–**c**) Orientation-dependent 3D tomograms based on $I_{||}$, indicating the locations of HA crystallites with the unit cell *c*-axis predominantly parallel to the experimental tomographic axis (indicated with an arrow for each case). To be judged significantly anisotropic, the intensity contribution along one axis had to be at least 30% higher than for the other two axes, otherwise the HA orientation in the voxel was considered to be isotropic. The dominating direction of the HA crystallite *c*-axis in different regions of the sample is color-coded and indicated by the arrows. Red indicates a proximal orientation of HA. Blue and green denote transverse orientations; blue follows the entepicondyle axis of the humerus while green shows an orientation orthogonal to the entepicondyle axis. (**d**) Tomogram highlighting voxels with isotropically oriented HA. (**e**,**f**) Preferred orientation of HA, visualized by a superposition of the three orthogonal tomograms, shown in two different views. The mesh plane at the lower half of the bone marks the position of the 2D section shown in Fig. 7.

As XRD-CT for muscle attachment mapping seemed promising, we decided to apply this method to a long-bone of the 370 million-year-old lobe-finned fish *Eusthenopteron foordi*. The more complex microarchitecture of the humerus of *Eusthenopteron foordi* was revealed by combining three independent full XRD-CT measurements with orthogonal tomography rotation axes. Reconstructed tomograms based on diffraction contrast, using the FBP algorithm for different scalar "descriptors" (integrated intensities), demonstrated the identification and location of different minerals to a voxel size of 150 μm. Due to the comparably large size of the humerus of *Eusthenopteron foordi*, the measurement in 3D had to be done with a lower resolution to keep the measurement time manageable. Finding the locations of muscle attachments unfortunately proved to be more complicated at this resolution. Indeed, the orientation analysis revealed that the cortical bone of the humerus seems to contain larger regions with dominating scattering in either of the perpendicular directions. Smaller regions corresponding to muscle attachments, previously identified with phase contrast CT[7], could not be observed conclusively in these XRD-CT 3D tomograms. Consistently with previous studies[40], this implies that the preferred direction of the HA crystallite *c*-axis varies rapidly as function of position, thus requiring higher resolution and making the precise determination of muscle attachments much more difficult in 3D.

Using exclusively the meridional part of the 002_{HA} Debye-Scherrer diffraction ring, we have demonstrated that spatially resolved information on the preferred orientation of HA in both the cortical and trabecular bone can be retrieved. In the cortical bone of the humerus of *Eusthenopteron foordi*, the HA crystallites in the diaphysis did not seem to exhibit a global preferential orientation. Locally, the crystallites were either longitudinally oriented, transversally oriented or organized with no preferential orientation. This observation is certainly due to the non-tubular and more complex shape of the *Eusthenopteron foordi* sample as compared to the long-bone of *Discosauriscus austriacus*, and would require a more sophisticated measurement scheme to be fully resolved.

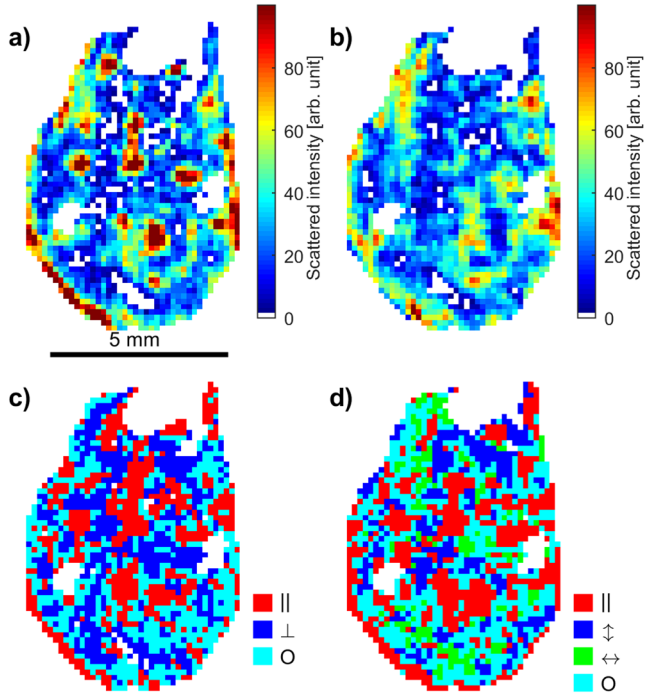

Figure 7. Cross section from 3D vectorial XRD-CT of the humerus of *Eusthenopteron foordi* (NRM P246c) yielding orientation information about the HA crystallites. (**a**) Single-axis tomogram based on $I_{\parallel}^{002HA}$, (**b**) single-axis tomogram based on $I_{\perp}^{002HA}$, (**c**) single-axis orientation parameter κ (Equation 2). Red colour corresponds to dominating out-of-plane scattering, while blue (small regions) indicate dominating in-plane scattering. Cyan means that the in-plane and out-of-plane contributions are approximately equal. (**d**) Orientation information reconstructed from the multiple-axis tomogram using $I_{\parallel}^{002HA}$ from each data set. This 2D section is a slice through the tomogram indicated by a plane in Fig. 6e,f. Results from both methods show consistency, and as expected, more details are visible in the multi-axis approach. Some empty regions in the sample (white) appear in all tomograms due to presence of other minerals than HA or low diffracted intensities $I_{\parallel}^{002HA}$ or $I_{\perp}^{002HA}$.

The analysis of fossil bone matrix ultrastructure allows interpretations on the paleobiology of animals, including bone growth rates[10,39] and/or adaptations to biomechanical loads[41]. Indeed, because the bone surface of the tibia of *Discosauriscus austriacus* was smooth and the bone long axis was oriented parallel to the tomography axis, the 002_{HA} Bragg peak could mainly be observed in the meridional direction ($I_{\parallel}$), thereby revealing that the gross orientation of HA was essentially parallel to the tomography axis (Fig. 3), i.e. with the HA *c*-axis parallel to the long axis of the bone. This confirms the identification of a parallel-fibred bone interpreted as the result of a relatively slow bone deposition rate[39]. Of course, using multiple-axes full tomography measurements with the sample in different orientations with respect to the tomography axis would have enabled more precise evaluations of the spatially varying main crystallite orientation[16,29] at the cost of a more complex and time-consuming experiment, which was not considered essential for the current purpose. We note that in addition to the biological information, XRD-CT also revealed details of the diagenesis. In the present study, we demonstrated that we could localize regions of calcite, barite and quartz resulting from the fossilisation.

Recently, other studies have been published[16,29,31] on reconstructing 3D orientation from non-crystalline objects using extensive data collection and advanced reconstruction algorithms, based on a large number of tomographic axes giving huge datasets. However, in our case the favourable nature of the HA crystallites allowed a simpler data collection and reconstruction process, using only one or three tomography axes. Combining scalar "descriptors" with the commonly used FBP algorithm is intuitively simple and easy to implement. It facilitates the analysis if the crystallites of interest have a close to isotropic distribution, and if their size is small compared to the beam size (or equivalently, small compared to the reconstructed voxel size). As explained in detail, the minerals constituting the *Eusthenopteron foordi* sample were found to exhibit different orientation properties and crystallite sizes. Importantly, the HA crystallites were deduced to be small compared to the voxels measured, because their orientation distributions were smooth, even when diffraction patterns from small volumes near the sample edge were studied. The HA crystallites exhibited broad orientation distributions ($\Delta\phi > 50°$, cf. SI), and the direction of the preferred orientation relative to the tomography axes was found to vary smoothly and systematically throughout the sample. For our approach based on the FBP, the spatially slowly varying HA orientation was decisive for being able to carry out the vectorial tomographic reconstructions for this material. Two procedures for creating vectorial tomograms were considered, one method using three orthogonal tomographic axes, the other using a single axis. The equatorial scattering $I_{\perp}$, being perpendicular to the sample rotation axis,

varied strongly during sample rotation, and FBP reconstruction artefacts in the tomograms must be expected for this reason. Nevertheless, as demonstrated, convincing similarities were found between the vectorial tomograms reconstructed from single-axis and three-orthogonal-axes tomographic measurements. Future work could consider the possibility of adopting iterative tomography reconstruction methods, effectively fitting an entire computer-generated 3D model, including spatial orientation distributions, to fully exploit the information contained in the experimental diffraction patterns.

In the special case of the sample containing a high number of small weakly textured oriented crystallites, XRD-CT provides detailed composition tomograms down to the limiting parameters of this experiment, i.e. the beam diameter giving reconstruction voxels of size 150 μm. The detector pixel size of 400 μm × 400 μm caused a resolution in Q of about 0.015 $Å^{-1}$. For the type of analysis performed, this rather low resolution in Q was an issue, as there were several overlapping Bragg peaks from the minerals. Of course, a higher detector resolution would demand even more from the data handling systems both during and after the experiment. A higher detector resolution would also allow extracting information about the crystallite size from the *width* of the Bragg peaks. Despite these limitations in this pioneering study, we have demonstrated for the first time that the spatially varying preferred orientation of HA in fossils can be obtained non-destructively.

The net exposure time for the XRD-CT experiments was approximately one hour for the tibia of *Discosauriscus austriacus* and approximately 24 hours for the humerus of *Eusthenopteron foordi*. There were additionally other time-consuming steps, e.g. calibration of the setup, alignment of samples before the start of each measurement and recording of dark current frames from the detector during the measurements. The total time spent on the experiments was therefore approximately 12 hours for the tibia of *Discosauriscus austriacus* and approximately 72 hours for the humerus of *Eusthenopteron foordi*. While the measurement strategy employed for these experiments was time consuming, we consider it likely that with the development of new high-brilliance synchrotron sources, more efficient detectors and read-out methods, XRD-CT in the near future can be performed at least one order of magnitude faster.

The current study demonstrates that XRD-CT is on the verge of becoming a powerful method for mapping in 3D the mineral composition and orientation in fossil samples. We showed here, to the best of our knowledge for the first time, that the information of muscle insertions could be retrieved with certainty in extant and fossil tetrapod bones. The muscle attachments are of vital importance to deduce how the extinct animals were moving through advanced biomechanical analysis. For the established method of polarized microscopy, it certainly is a huge disadvantage that scarce fossils have to be destroyed to extract the desired data. While the resolution in this study was too low to resolve the muscle attachments in the humerus of *Eusthenopteron foordi* in 3D, this pilot study still demonstrates the feasibility of extracting such information, even for old fossil bones. This is a considerable contribution towards the development of diffraction-based CT techniques for reconstructing the rearrangement of soft tissues through major evolutionary events. Despite the efforts that are needed to carry out an XRD-CT experiment and its subsequent analysis, we believe that the unique information that can be extracted from such experiments will prove the technique crucial for studying palaeontological, biological and synthetic functional materials in future.

Methods

The specimen of *Desmognathus quadramaculatus* was collected under ethical guidelines for research study by Bruce *et al.*[42]. The humerus was dissected, dried and embedded in a polyester resin. The bone was sectioned using an annular diamond-powder saw. The observations were made under polarized light through a Zeiss Axiovert 35 optical microscope. Pictures were taken with an Olympus Camedia C5060 camera fixed on the microscope at Sorbonne University (UPMC, France). The acid-prepared[43]. specimen of *Discosauriscus austriacus* (DE KO 58) is stored in the research collections of the Comenius University (Bratislava, Slovakia). The limb bone was embedded in a polyester resin to be sectioned, using the same method as for *Desmognathus quadramaculatus*. The mechanically prepared specimen of *Eusthenopteron foordi* (NRM P246c) was provided by Naturhistoriska Riksmuseet (Stockholm, Sweden).

All XRD-CT measurements on the two fossil samples were performed at beamline ID15A at ESRF, using a monochromatic beam with a wavelength 0.143 Å (86.6 keV). 2D diffraction patterns were recorded on a Perkin-Elmer XRD 1621 N ES Series detector with an effective pixel size of 400 μm × 400 μm. The exposure time for each recorded diffraction pattern was 70 ms for the tibia of *Discosauriscus austriacus* and 35 ms for the humerus of *Eusthenopteron foordi*. One highly resolved tomographic cross section was measured in the tibia of *Discosauriscus austriacus*, transversally through the diaphysis of the sample, resulting in a reconstructed pixel size of approximately 20 μm × 20 μm. For the humerus of *Eusthenopteron foordi*, the entire sample volume was imaged with three independent full sets of XRD-CT measurements. The latter were performed with three approximately orthogonal orientations of the sample on the sample stage, allowing information about the preferred orientation to be extracted. For each tomographic projection angle ω, 100 steps in x and y and 80 rotation angles were used, resulting in an effective voxel size of approximately 150 μm × 150 μm × 150 μm. For further details about the XRD-CT measurements and reconstruction procedure, cf. SI.

Transmission raster-scanning XRD measurements were performed at beamline ID27 at ESRF. An orientation map was obtained in the vicinity of a muscle insertion in a thin physically cut section of the humerus of the (extant) salamander *Desmognathus quadramaculatus*. For these measurements, a beam with wavelength 0.374 Å (33.2 keV) and a 20 × 20 μm cross section was used. Diffraction patterns were collected on a MAR345 image-plate detector with 158 × 158 μm pixel size and integrated using the XRDUA software[44]. The complete 2D data set consists of 61 × 51 diffraction patterns.

References

1. Cunningham, J. A., Rahman, I. A., Lautenschlager, S., Rayfield, E. J. & Donoghue, P. C. J. A virtual world of paleontology. *Trends Ecol Evol* **29**, 347–357 (2014).
2. Sanchez, S., Ahlberg, P. E., Trinajstic, K. M., Mirone, A. & Tafforeau, P. Three-dimensional synchrotron virtual paleohistology: a new insight into the world of fossil bone microstructures. *Microsc Microanal* **18**, 1095–1105 (2012).
3. Trinajstic, K. *et al*. Fossil musculature of the most primitive jawed vertebrates. *Science* **341**, 160–164 (2013).
4. Benjamin, M. *et al*. The skeletal attachment of tendons—tendon 'entheses'. *Comparative Biochemistry and Physiology Part A: Molecular & Integrative Physiology* **133**, 931–945 (2002).
5. Benjamin, M. *et al*. Where tendons and ligaments meet bone: attachment sites ('entheses') in relation to exercise and/or mechanical load. *Journal of anatomy* **208**, 471–490 (2006).
6. Hieronymus, T. L. Quantitative microanatomy of jaw muscle attachment in extant diapsids. *Journal of Morphology* **267**, 954–967 (2006).
7. Sanchez, S. *et al*. 3D microstructural architecture of muscle attachments in extant and fossil vertebrates revealed by synchrotron microtomography. *PLoS One* **8**, e56992 (2013).
8. Bromage, T. G. *et al*. Circularly polarized light standards for investigations of collagen fiber orientation in bone. *The Anatomical Record* **274**, 157–168 (2003).
9. Bacon, G. E., Bacon, P. J. & Griffiths, R. K. Orientation of apatite crystals in relation to muscle attachment in the mandible. *J Biomech* **13**, 725–729 (1980).
10. Francillon-Vieillot, H. B. V. *et al*. Microstructure and mineralization of vertebrate skeletal tissues. *Skeletal Biomineralization: Patterns, Processes and Evolutionary Trends* **20**, 471–1529 (1990).
11. Dumont, M., Pyzalla, A., Kostka, A. & Borbély, A. In *Biology of the sauropod dinosaurs: Understanding the life of giants* 150–170 (Indiana University Press, 2011).
12. Zocco, T. G. & Schwartz, H. L. Microstructural analysis of bone of the sauropod dinosaur Seismosaurus by transmission electron microscopy. *Palaeontology* **37**, 493–504 (1994).
13. Dumont, M., Borbely, A., Kaysser-Pyzalla, A. & Sander, P. M. Long bone cortices in a growth series of Apatosaurus sp.(Dinosauria: Diplodocidae): geometry, body mass, and crystallite orientation of giant animals. *Biological journal of the Linnean Society* **112**, 782–798 (2014).
14. Klembara, J. & Bartík, I. The postcranial skeleton of Discosauriscus Kuhn, a seymouriamorph tetrapod from the Lower Permian of the Boskovice Furrow (Czech Republic). *Earth and Environmental Science Transactions of The Royal Society of Edinburgh* **90**, 287–316 (1999).
15. Molnar, J. L., Diogo, R., Hutchinson, J. R. & Pierce, S. E. Reconstructing pectoral appendicular muscle anatomy in fossil fish and tetrapods over the fins-to-limbs transition. *Biol Rev* **93**, 1077–1107 (2018).
16. Liebi, M. *et al*. Nanostructure surveys of macroscopic specimens by small-angle scattering tensor tomography. *Nature* **527**, 349–352 (2015).
17. Als-Nielsen, J. & MacMorrow, D. *Elements of modern X-ray physics*. 187–191 (Wiley, 2011).
18. Brandon, D. G. & Kaplan, W. D. *Microstructural characterization of materials*. 261–331 (Wiley, 1999).
19. Dumont, M., Kostka, A., Sander, P. M., Borbely, A. & Kaysser-Pyzalla, A. Size and size distribution of apatite crystals in sauropod fossil bones. *Palaeogeography, Palaeoclimatology, Palaeoecology* **310**, 108–116 (2011).
20. Jörg, S. *et al*. Two-dimensional X-ray diffraction as a tool for the rapid, nondestructive detection of low calcite quantities in aragonitic corals. *Geochemistry, Geophysics, Geosystems* **16**, 3778–3788 (2015).
21. Schroer, C. *et al*. Mapping the local nanostructure inside a specimen by tomographic small-angle x-ray scattering. *Applied physics letters* **88**, 164102 (2006).
22. Feldkamp, J. *et al*. Recent developments in tomographic small-angle X-ray scattering. *physica status solidi (a)* **206**, 1723–1726 (2009).
23. Skjønsfjell, E. T. B. *et al*. High-resolution coherent x-ray diffraction imaging of metal-coated polymer microspheres. *Journal of the Optical Society of America A* **35**, (2017).
24. Miao, J. W., Charalambous, P., Kirz, J. & Sayre, D. Extending the methodology of X-ray crystallography to allow imaging of micrometre-sized non-crystalline specimens. *Nature* **400**, 342–344 (1999).
25. Chapman, H. N. & Nugent, K. A. Coherent lensless X-ray imaging. *Nature Photonics* **4**, 833–839 (2010).
26. Rodenburg, J. M. *et al*. Hard-x-ray lensless imaging of extended objects. *Phys Rev Lett* **98** (2007).
27. Thibault, P. *et al*. High-resolution scanning x-ray diffraction microscopy. *Science* **321**, 379–382 (2008).
28. Esmaeili, M. *et al*. Ptychographic X-ray Tomography of Silk Fiber Hydration. *Macromolecules* **46**, 434–439 (2013).
29. Schaff, F. *et al*. Six-dimensional real and reciprocal space small-angle X-ray scattering tomography. *Nature* **527**, 353–356 (2015).
30. Schaff, F. *et al*. Correlation of X-Ray Vector Radiography to Bone Micro-Architecture. *Sci Rep-Uk* **4** (2014).
31. Donnelly, C. *et al*. Three-dimensional magnetization structures revealed with X-ray vector nanotomography. *Nature* **547**, 328–331 (2017).
32. Harding, G., Kosanetzky, J. & Neitzel, U. X-ray diffraction computed tomography. *Medical physics* **14**, 515–525 (1987).
33. Alvarez-Murga, M. *et al*. Microstructural mapping of C60 phase transformation into disordered graphite at high pressure, using X-ray diffraction microtomography. *J Appl Crystallogr* **44**, 163–171 (2011).
34. Poulsen, H. F. An introduction to three-dimensional X-ray diffraction microscopy. *J Appl Crystallogr* **45**, 1084–1097 (2012).
35. Bleuet, P. *et al*. Probing the structure of heterogeneous diluted materials by diffraction tomography. *Nature materials* **7**, 468–472 (2008).
36. Clack, J. A. Devonian tetrapod trackways and trackmakers; A review of the fossils and footprints. *Palaeogeogr Palaeocl* **130**, 227–250 (1997).
37. Sanchez, S., Tafforeau, P. & Ahlberg, P. E. The humerus of Eusthenopteron: a puzzling organization presaging the establishment of tetrapod limb bone marrow. *P Roy Soc B-Biol Sci* **281** (2014).
38. Kak, A. C. & Slaney, M. *Principles of computerized tomographic imaging*. 49–117 (IEEE Pr., 1988).
39. Sanchez, S., Klembara, J., Castanet, J. & Steyer, J. S. Salamander-like development in a seymouriamorph revealed by palaeohistology. *Biol Lett* **4**, 411–414 (2008).
40. Nakano, T., Ishimoto, T., Jee-Wook, L. & Umakoshi, Y. Preferential orientation of biological apatite crystallite in original, regenerated and diseased cortical bones. *Journal of the Ceramic Society of Japan* **116**, 313–315 (2008).
41. De Margerie, E., Sanchez, S., Cubo, J. & Castanet, J. Torsional resistance as a principal component of the structural design of long bones: comparative multivariate evidence in birds. *The Anatomical Record* **282**, 49–66 (2005).
42. Bruce, R. C., Castanet, J. & Francillon-Vieillot, H. Skeletochronological analysis of variation in age structure, body size, and life history in three species of desmognathine salamanders. *Herpetologica* **58**, 181–193 (2002).
43. Štamberg, S. Chemical preparation of vertebrates from the Lower Permian of the BoskoviceFurrow *Acta Musei reginaehradecensis. Series A, Scientiae naturales* **29**, 143–150 (2003).
44. De Nolf, W., Vanmeert, F. & Janssens, K. XRDUA: crystalline phase distribution maps by two-dimensional scanning and tomographic (micro) X-ray powder diffraction. *J Appl Crystallogr* **47**, 1107–1117 (2014).

Acknowledgements

We are grateful to Jozef Klembara from the Comenius University (Bratislava, Slovakia) and Thomas Mörs at Naturhistoriska Riksmuseet (Stockholm, Sweden) for providing the fossil material for the current study. We thank Paul Tafforeau (ESRF) for his help during the experiment at beamline ID19. We thank Irene Zanette (TUM) and Mario Scheel (ESRF) for their help with the experiment at beamline ID15A. We acknowledge Timothy Bromage (NYU), Armand de Ricqlès (MNHN) and Maïtena Dumont (UU) for fruitful discussions. We thank Philippe

Loubry (MNHN) for the photograph of the tibia of *Discosauriscus austriacus*. Beamtime was allocated at the European Synchrotron Radiation Facility for the XRD-CT measurements at beamline ID15A (EC-1017); inhouse beamtime at ID27 and phase contrast experiments at ID19 ID19 (ES-203). S.S. was funded by a grant from the Vetenskapsrådet (2015-04335) and received a stipend from Helge Ax:son Johnsons Stiftelse. F. K. M. and D.W.B. gratefully acknowledge the Norwegian Research Council for financial funding.

Author Contributions

F.P., S.S., M.B., M.M. and M.A. designed the experiment. S.S. prepared the samples. F.P., S.S., M.B., M.M., M.A. and F.K.M. performed the measurements. F.K.M., M.B. and D.W.B. analysed the data from the fossil samples. M.A. performed the data analysis on the extant sample. S.S. made biological and palaeontological interpretations. F.K.M. and D.W.B. wrote the manuscript. All authors commented on the manuscript.

Additional Information

Supplementary information accompanies this paper at https://doi.org/10.1038/s41598-018-28269-1.

Competing Interests: The authors declare no competing interests.

Publisher's note: Springer Nature remains neutral with regard to jurisdictional claims in published maps and institutional affiliations.

Discover Geoscience

RESEARCH Open Access

Geochemical and mineralogical analysis of ophiolitic and sedimentary formations in middle Andaman

Pardeep Kumar[1,3], Deeksha Khandelwal[2], Varinder Kanwar[1] and Saumitra Mukherjee[3*]

*Correspondence:
Saumitra Mukherjee
saumitramukherjee3@gmail.com
[1]National Accreditation Board for Education and Training, Quality Council of India, New Delhi 110002, India
[2]Inter University Accelerator Center, New Delhi 110067, India
[3]School of Environmental Sciences, Jawaharlal Nehru University, New Delhi 110067, India

Abstract
The Middle Andaman region of the Andaman Islands is of considerable geological and ecological significance. This study provides a comprehensive geochemical and mineralogical analysis of major oxides and trace elements in soil and rock samples from ophiolitic and sedimentary formations. A total of 24 samples were collected and analyzed using X-ray fluorescence (XRF), X-ray diffraction (XRD), and thin section analysis to assess their composition and distribution. Dominant major oxides identified include silica (SiO_2), alumina (Al_2O_3), and iron oxide (Fe_2O_3), which are typically associated with felsic volcanic and sedimentary formations. Trace elements are found in the following order of abundance: Cr, Ba, Zr, Zn, V, Ni, Rb, Sr, Pb, Co, Th, and Sc. Mineralogical investigations reveal key minerals such as albite, biotite, garnet, kyanite, chromite, and celestite, indicating volcanic and sedimentary origins, with a complex geological history shaped by a semi-arid to semi-humid climate. Geochemical analysis suggests moderate to intense weathering, reflected in the chemical index of alteration (CIA) values. Dissolution of undersaturated minerals like calcite and gibbsite influences groundwater chemistry, while oversaturated minerals such as halite and manganese oxides precipitate, affecting groundwater flow and aquifer permeability. Trace metals, including iron, manganese, cadmium, and lead, indicate both natural and anthropogenic influences. These findings underscore the need for ongoing geochemical monitoring and integrated management strategies for sustainable groundwater and marine resource management in the region.

Keywords Middle andaman, XRF, XRD, Trace metals, Groundwater quality, Thin section analysis.

1 Introduction

Geochemical analysis, utilizing various methods, is crucial for assessing paleo-weathering and understanding the influence of climate on depositional settings [1, 2]. The study of the mineralogical and chemical compositions of clastic sedimentary rocks offers valuable insights into erosional processes and the degree of weathering in source regions. This is important as the primary variables that influence the geochemistry of clastic sedimentary rocks are lithology, mineral composition, chemical weathering, source

locations, and post-depositional modifications during diagenesis [3]. Given this, the analysis of major and trace elements provides essential information on how climatic factors influenced clastic sediment deposition and weathering in a region.

Geochemical and mineralogical properties have long been recognized for their importance in understanding tectonic evolution, geological history, and potential resource identification, as well as providing inferences for environmental considerations [1, 4–7]. Moreover, these properties lay the groundwork for comprehending the geological forces that shaped the Andaman Islands and their significance within the context of plate tectonics and Earth's long geological history [8–10]. The Middle Andaman region, located in the Andaman and Nicobar Islands archipelago, is particularly important due to its unique geological history and diverse mineralogical assemblages. Detailed geochemical analysis of this region offers a deeper understanding of both its geological evolution and the underlying environmental conditions.

Geochemical analysis plays a central role in identifying the elemental composition and distribution patterns of rocks, sediments, and soils in a given environment [11, 12]. By investigating key oxides and trace elements in the Middle Andaman region, scientists can derive valuable insights into the processes that have shaped this terrain over millions of years [2, 13]. The geological study of the region involves a systematic approach that includes field sampling, laboratory examination, and data interpretation to derive meaningful conclusions about the area's geochemistry. The most commonly used methods for quantifying major oxides and trace elements are X-ray fluorescence (XRF) and X-ray diffraction (XRD). These techniques are fundamental in geochemical studies as they enable the identification of chemical composition, mineralogy, and provenance, providing insights into the climatic, erosional, and diagenetic processes that have influenced the region's sedimentary formations.

X-ray fluorescence (XRF) is a widely used, non-destructive method that identifies the elemental composition of a sample by measuring the secondary X-rays emitted when the sample is exposed to high-energy radiation. This technique allows for the quantification of major oxides and trace elements in rocks, soils, and sediments, making it an invaluable tool in geochemical studies [14–17]. By applying XRF to the Middle Andaman samples, this study assesses the concentrations of major elements like SiO_2, Al_2O_3, and Fe_2O_3, which are significant in understanding the mineralogical composition and geochemistry of the region. X-ray diffraction (XRD) is another essential technique employed in this research. It is used to identify crystalline mineral phases by analyzing diffraction patterns that emerge when X-rays interact with a material's atomic structure. Since each mineral exhibits a unique diffraction pattern, XRD is invaluable in identifying minerals and understanding their structural characteristics. This method is particularly useful in identifying mineral phases in sedimentary rocks and understanding their geological history.

In addition to these methods, thin-section petrography is used to examine the textural and mineralogical properties of the samples at a microscopic level [14–17]. This technique provides detailed information on grain size, mineral composition, texture, and the degree of weathering or diagenesis, which further enriches the understanding of the geological processes that shaped the Middle Andaman region.

The major oxides—SiO_2, Al_2O_3, Fe_2O_3, MgO, K_2O, Na_2O, CaO, TiO_2, MnO, and P_2O_5—are the building blocks of most rocks, and their concentrations provide significant

insights into the mineralogy, lithology, and weathering history of the region [18–20]. The study of these oxides is crucial for understanding the degree of chemical weathering that has occurred in the Middle Andaman region, offering a window into its past climatic conditions and erosional history [21–23]. For instance, higher concentrations of SiO_2 and Al_2O_3 typically indicate more weathered or felsic source rocks, while higher concentrations of Fe_2O_3 can indicate more mafic or iron-rich formations.

Beyond major oxides, trace metals are of great importance in understanding the geochemical properties of a region. Although trace elements are found in much lower concentrations, they provide valuable information about the region's geological processes, mineralogy, and environmental conditions. Elements such as iron (Fe), chromium (Cr), cobalt (Co), nickel (Ni), copper (Cu), lead (Pb), zinc (Zn), and rare earth elements (REEs) are commonly studied due to their relevance in petrogenesis, mineralogy, and economic potential [24–27]. The analysis of these elements helps identify the provenance of the sedimentary materials and can offer clues regarding tectonic settings and the history of the region.

The Middle Andaman region is particularly significant for its diverse and unique mineralogical assemblages, which include a wide range of silicate, oxide, and carbonate minerals. The region's hydrological and seawater data reveal an intricate balance between mineral dissolution and precipitation, which affects groundwater quality and availability [28]. Continuous monitoring of mineral dissolution and precipitation processes is essential for managing groundwater resources and assessing contamination risks from both natural and anthropogenic sources [7, 29].

This study presents a detailed investigation of the geochemical and mineralogical characteristics of the Middle Andaman region (Fig. 1). By examining the major oxides and trace elements, the research aims to provide insights into the geological evolution of the Andaman Islands, the climatic and weathering history, and the potential for sustainable management of groundwater resources in this ecologically significant region.

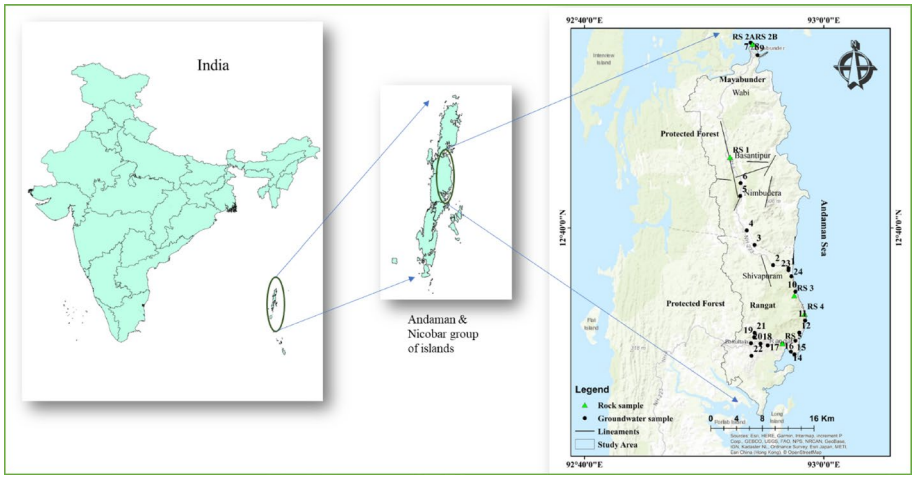

Fig. 1 Geospatial map of India (left) highlighting the Andaman and Nicobar Islands (center), with a detailed view of the study area (right) showing locations of rock and soil sample collection

2 Geology and lithostratigraphy

The Middle Andaman region boasts a rich and complex geological history, shaped by millions of years of tectonic activity, including rifting, subduction, and volcanic processes [30]. Positioned along the active boundary between the Indian Plate and the Burma Plate, this region is part of the larger tectonic framework that forms the Andaman Trench. The tectonic interactions in the area have contributed to the formation of a diverse geological landscape, which includes a combination of igneous, sedimentary, and metamorphic rocks. These rock formations reflect the region's dynamic tectonic evolution over time [31, 32] (Fig. 2b).

The geological framework of Middle Andaman falls within the Mélange Structural Unit, a tectonically complex zone characterized by a mix of highly deformed and sheared lithologies. This includes ophiolitic rocks, deep-sea sediments, and volcanic formations, all of which provide essential clues to understanding the region's geological history [33, 34]. The Mélange Unit offers a snapshot of various geological processes that have shaped the region, providing a wealth of information about the tectonic forces at play and their impact on the local lithology (Fig. 2a).

The primary lithostratigraphic units in the Middle Andaman region include the Karmatang Sandstone and the Mithakhari Formation, both of which are key sedimentary deposits that were formed under different depositional conditions. The Karmatang Sandstone, composed predominantly of quartz arenites and lithic arenites, is indicative of fluvial to deltaic depositional environments. The mineral composition of these sandstones reflects the influence of water transport, leading to the sorting and deposition of fine to coarse particles in river and delta systems. On the other hand, the Mithakhari Formation, composed of interbedded sandstones and shales, is associated with marine depositional settings, highlighting the diverse environmental conditions that influenced sedimentation in the area [35].

Earlier geological studies of the region [33, 34] have also identified the presence of ophiolitic sequences, including basalt, peridotite, and gabbro, which are remnants of ancient oceanic crust. These ophiolitic rocks, along with associated sedimentary

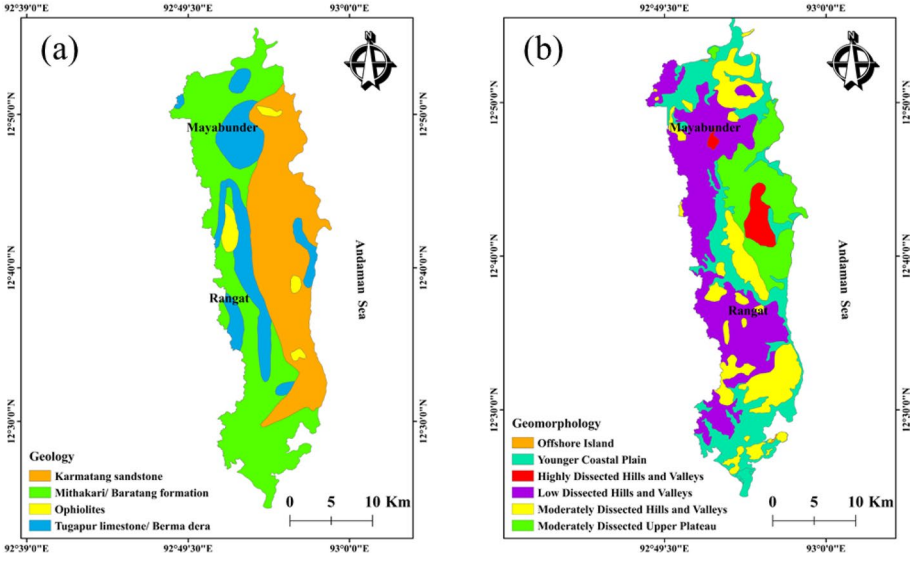

Fig. 2 **a** Geological map of Middle Andaman showing rock formations and lithological units **b** Geomorphological map of Middle Andaman depicting landforms and surface features

successions, are significant as they provide valuable insights into the tectonic evolution and paleogeographic history of the Andaman region. These formations not only reveal the processes that have shaped the area but also offer clues to understanding the movement and interactions between the tectonic plates over geological time.

Petrographic and geochemical analyses of rock samples from the Middle Andaman region confirm the dominance of quartz-rich sandstones, clay minerals, and feldspathic components, with strong evidence of weathering and diagenetic alterations. The presence of these components suggests significant changes in the composition and texture of the rocks over time, potentially due to climatic conditions, tectonic forces, and chemical weathering processes. Furthermore, the identification of microfossils and mineralogical assemblages within the sedimentary formations adds another layer of understanding, indicating fluctuating depositional environments throughout the region's history. These findings suggest that the Middle Andaman region has experienced a range of environmental conditions, from marine to transitional settings, influencing the deposition of sediments and the formation of various geological features [36].

2.1 Seismotectonic of middle Andaman

The geology and hydrogeology of the Middle Andaman region have been profoundly shaped by seismic activity, as evidenced by historical earthquake events. Notable large-magnitude earthquakes, such as those in 1762, 1847, and 1881, have had lasting effects on the region's physical landscape and subsurface water systems [7]. These seismic events, especially those accompanied by substantial co-seismic uplift and subsidence, have significantly reshaped the coastline and altered the topography of the area. The resulting changes have a direct impact on groundwater flow patterns and storage, influencing the movement and availability of water in the region's aquifers.

Uplift and subsidence, as a result of seismic activity, have major implications for aquifer structures by modifying key factors such as porosity, permeability, and water recharge zones. The alteration of these physical properties affects how groundwater flows and accumulates in the subsurface. Seismic events also create fractures and faults within the earth's crust, which can serve as new conduits for mineral dissolution. This process can lead to the increased concentration of major ions and trace metals in groundwater, thereby altering its chemical composition and potentially affecting water quality. In some cases, these fractures may act as barriers that impede the movement of water, further complicating the hydrological dynamics of the region.

Furthermore, the tsunamis triggered by these significant seismic events often result in saltwater intrusion into coastal aquifers, degrading water quality. This phenomenon is particularly problematic in the low-lying coastal regions of the island, where the effects of saltwater intrusion are more pronounced [37]. The interaction between seismic activity and hydrogeology highlights the dynamic and evolving nature of groundwater systems in tectonically active regions. It also underscores the need to incorporate seismic impacts into groundwater management and resilience strategies, ensuring that water resources are managed sustainably in the face of ongoing tectonic and seismic events. Figure 3 illustrates the major earthquakes (magnitude > 6) that have occurred between 1990 and 2022, providing further context to the seismic activity influencing the region's geology and hydrology [38].

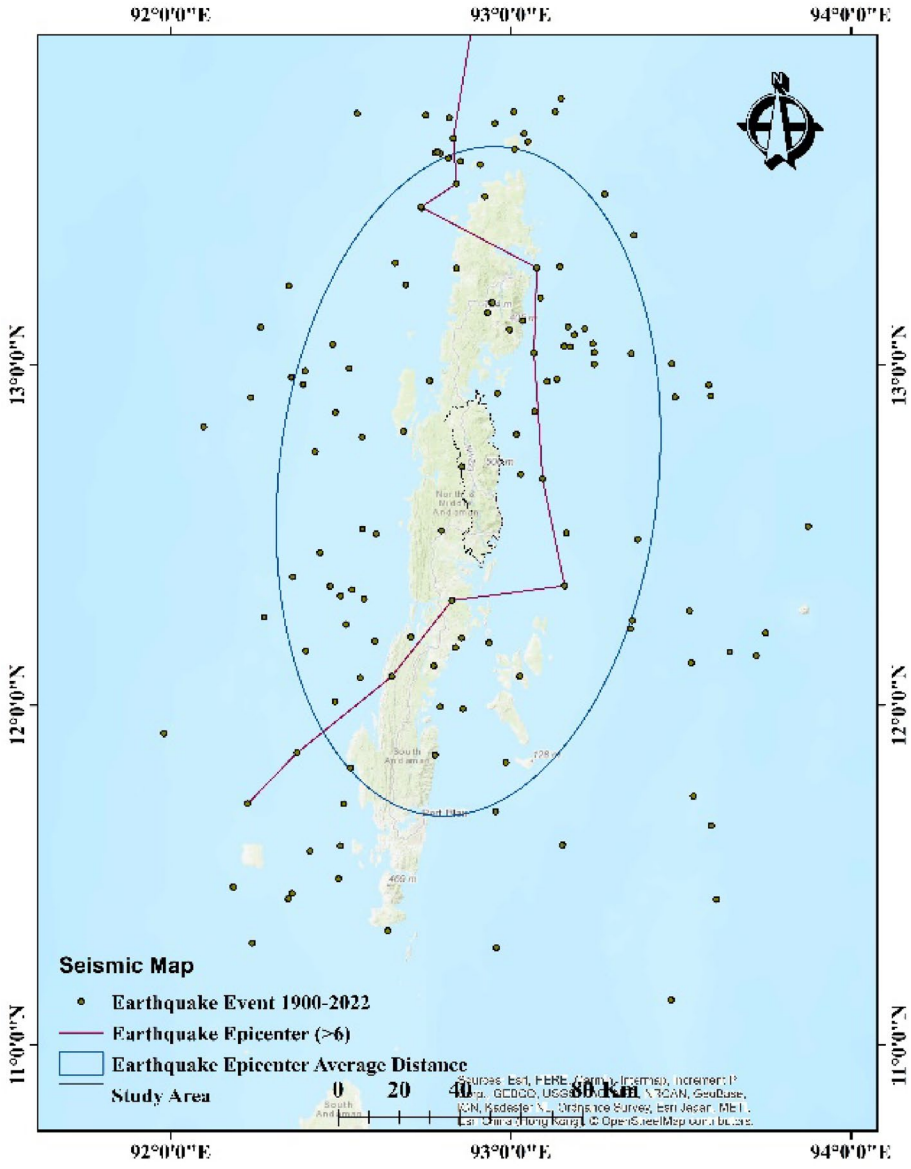

Fig. 3 Seismotectonic map of Middle Andaman illustrating fault lines, seismic activity, and tectonic features [38]

3 Methodology

In this study, 16 soil samples and 2 core samples (Fig. 1) from Middle Andaman were analyzed using X-ray diffraction (XRD) and X-ray fluorescence (XRF). Additionally, thin-section analysis was conducted on 6 rock samples. The detailed methodology for each analysis is outlined below.

3.1 Sample collection and preparation

In April 2019, representative rock, soil, and core samples were collected from various locations in Middle Andaman along a horizontal transect towards the tide line. A total of 24 groundwater samples and one seawater sample were also collected for hydrogeological analysis [7]. The rock samples were cleaned to remove weathered surfaces and then broken into smaller fragments. A portion of the rock samples was sent for thin-section analysis, while the remaining samples were crushed into smaller pieces. Soil and core

samples were cleaned to remove organic impurities and homogenized using the coning and quartering method. Subsequently, all samples were crushed into a powdered form and dried in an oven at 110 °C for 24 h. Once dried, the samples were pulverized and sieved through a 200-micron mesh for further analysis.

3.2 XRD and XRF analysis

The sieved rock and soil samples were analyzed using X-ray diffraction (XRD) with a PANalytical X'Pert PRO instrument with Cu–Kα radiation. Each sample was scanned over a 2θ range of ~5–80° at a step size of ~0.02° (2θ) and dwell time of a few seconds per step (typical Bragg-Brentano geometry). The mineralogical composition was determined using X'Pert HighScore 1.0a software. The XRD data provided d-spacing values, which were matched with a known mineral database to confirm the mineralogy of the samples. Primary and secondary d-spacing peaks were compared with standard reference values [40] for mineral identification. For X-ray fluorescence (XRF) analysis, the powdered samples were dried at 110 °C until no further weight loss was observed. One gram of the finely ground sample was mixed with 0.5 g of boric acid, thoroughly homogenized, and pressed into a 30 mm diameter pellet using a 15-ton hydraulic press. These pellets were analyzed using an Axios Max (PANalytical) XRF instrument to quantify the major oxides and trace metal concentrations. Elemental results were considered valid when measurements from standard and duplicate samples agreed within ± 5% (1σ) of the certified reference values.

3.3 Petrography

Thin-section preparation began by cutting an 8–10 mm piece from each rock sample using a cutting station at the Micropaleontology Lab, Department of Geology, University of Delhi, India. The rock surface and glass slide were roughened using silicon carbide and water to improve adhesion. The samples were then bonded with KEPT epoxy resin under pressure using Geofix. The rock samples were cut down to approximately 2.0 mm thickness and ground on the Geoform station to 80 microns, with 50-micron steps above 200 microns. The samples were then lapped with a silicon carbide/water mix on a KemTech III machine, and once cleaned, the slides were polished using a PSU-M pad and diamond suspension, progressively reducing the micron size to achieve a final thickness of around 30 microns. The prepared thin sections were cleaned, inspected, and were ready for petrographic analysis [39]. Thin sections were analyzed or observed under a petrographic microscope.

3.4 Software used

For the analysis of XRD data, Origin 2018 was used to create plots and interpret results. Binary and ternary plots of soil samples were also generated to aid interpretation. Geospatial modeling for the Middle Andaman region was carried out using ArcGIS 10.8.

4 Result and discussion

4.1 Soil sample analysis

4.1.1 XRD analysis of soil samples

The X-ray Diffraction (XRD) analysis of soil samples from various stations in the Middle Andaman region offers significant insights into their mineralogical composition,

depositional history, and geological framework. The results reveal a diverse mineral assemblage comprising albite, biotite, brookite, cassiterite, celestite, chloritoid, chromite, garnet (pyrope), glauconite, glauberite, hypersthene, kyanite, magnetite, muscovite, oligoclase, phillipsite, sanidine, tourmaline, and wollastonite, along with trace minerals [40].

The spatial distribution of these minerals correlates strongly with the geological and geomorphological characteristics of the study area. The presence of high-pressure, high-temperature metamorphic minerals such as garnet, kyanite, and chloritoid suggests a significant contribution from high-grade metamorphic rock sources, likely derived from ophiolitic sequences and regional metamorphic complexes. The occurrence of magnetite and chromite, typically associated with ultramafic rocks, further supports the influence of ophiolitic fragments within the Andaman accretionary prism, reflecting a history of subduction-related geological processes.

Marine depositional influences are evident through the identification of glauconite and phillipsite, minerals commonly formed in marine and estuarine environments. Their presence aligns with the tectonic and sedimentary evolution of the Andaman region, highlighting prolonged sedimentation under marine conditions. Additionally, the detection of biotite—a mineral present in both metamorphic and igneous formations—suggests contributions from the continental crust. This interpretation is reinforced by the abundance of albite, oligoclase, and muscovite, which are characteristic of granitic and felsic igneous sources.

Furthermore, the presence of brookite (a titanium-bearing mineral) and cassiterite (a tin-bearing mineral) suggests possible hydrothermal activity or weathering processes that concentrated these minerals within the sediments. The distribution of minerals across different sampling locations indicates variations in topography, weathering intensity, and depositional environments. Coastal and deltaic regions exhibit higher concentrations of glauconite and phillipsite, confirming strong marine influences, whereas upland areas display a dominance of garnet, kyanite, and chloritoid, suggesting proximity to metamorphic and tectonically uplifted zones.

The XRD results validate the diverse lithological contributions to soil formation in Middle Andaman, emphasizing the role of climate-controlled weathering, sediment transport, and tectonic evolution in shaping the mineralogical landscape. The sample distribution across the study area is depicted in the location map (Fig. 1), while Figs. 4 and 5 illustrate the labeled d-spacing values of minerals for each station, providing a comprehensive overview of the mineralogical variations across the region.

4.2 Statistics of chemical composition of major oxides and trace metals

X-ray Fluorescence (XRF) analysis was conducted on soil samples to quantify the major oxides and trace metals present. Statistical parameters, including average, minimum, maximum, and standard deviation, were calculated to determine their dominance in the study area. The order of abundance of major oxides (%) in the soil samples is SiO_2 >Al_2O_3 >Fe_2O_3 >MgO > K_2O > Na_2O > CaO > TiO_2 >MnO > P_2O_5, with SiO_2 being the most dominant (35.38–77.56%, avg. 63.16%). This high silica content suggests the presence of silicate minerals such as quartz, feldspar, and mica, predominantly sourced from granitic and metamorphic rocks [7]. In contrast, Chandrasekaran et al. (2015) [41] reported higher CaO levels (12.18% avg.) and dominance of carbonate minerals like calcite and

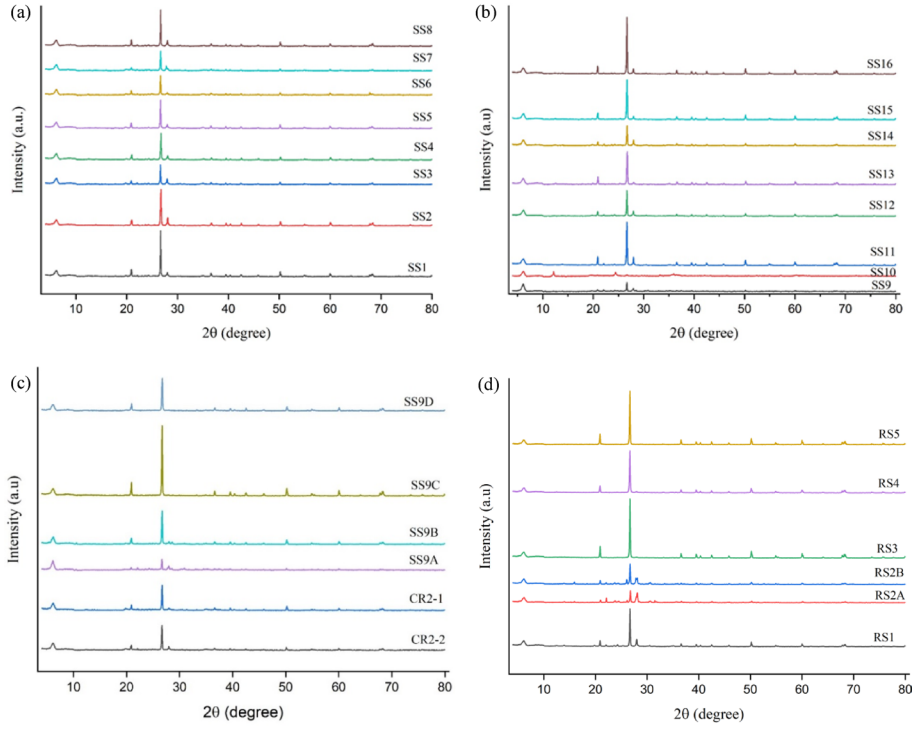

Fig. 4 XRD plots illustrating the mineralogical compositions of samples from the Middle Andaman region: **a** Soil samples (SS1 to SS8), **b** Soil samples (SS9 to SS16), **c** Soil profile samples (CR2-1, CR2-2, and SS9A-SS9D), and **d** Rock samples (RS1 to RS5)

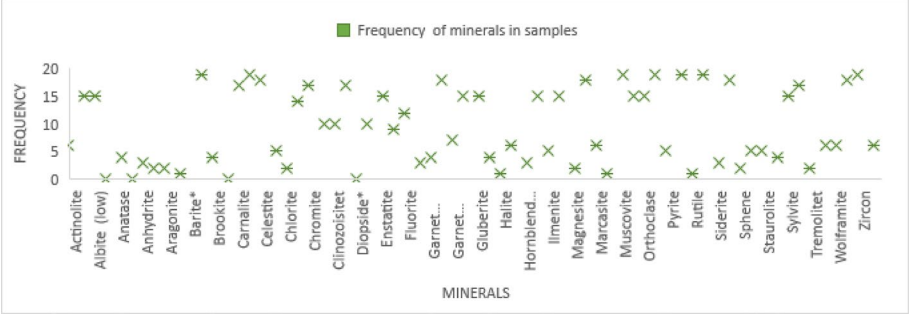

Fig. 5 Mineral composition of Middle Andaman, highlighting the distribution of major silicate, oxide, and carbonate minerals identified through XRD and geochemical analysis

aragonite in Andaman beach rocks, which were interpreted as products of biogenic and chemical cementation. This contrast highlights a clear distinction between inland quartzose soils and coastal carbonate-rich sediments, linked to differing depositional and diagenetic environments.

The significant Al_2O_3 content (4.28–19.10%, avg. 13.45%) indicates intense chemical weathering and the presence of alumino-silicate minerals like kaolinite and illite, which are commonly associated with tropical and subtropical climatic conditions. The Fe_2O_3 concentration (3.83–11.81%, avg. 7.13%) suggests the presence of iron oxides, such as hematite and goethite, which are formed through oxidative weathering and contribute to the lateritic soil characteristics of the region.

Magnesium oxide (MgO), potassium oxide (K_2O), and sodium oxide (Na_2O) show average concentrations between 1% and 5%, reflecting the contribution of ferromagnesian minerals such as biotite, chlorite, and pyroxene, which originate from mafic and ultramafic rocks. K_2O content suggests the presence of potassium feldspars and mica minerals, indicative of granitic influences, while Na_2O is associated with sodium-rich feldspars like albite. In contrast, CaO, TiO_2, MnO, and P_2O_5 are present in lower concentrations (< 1%). Titanium dioxide (TiO_2) is primarily derived from stable minerals like rutile and ilmenite, which resist weathering and persist in the soil as residual phases. This mineralogical and chemical weathering profile is notably different from the marine cementation processes in beach rock, where diagenesis is driven by supersaturation with respect to calcite and aragonite—conditions absent in the inland soil environment studied here [41].

For trace metals (ppm), the order of abundance in soil samples is Cr > Ba > Zr > Zn > V > Ni > Rb > Sr > Pb > Co > Th > Sc, with Cr, Ba, Zr, and Zn concentrations exceeding 100 ppm. Vanadium (V), nickel (Ni), rubidium (Rb), and strontium (Sr) range between 50 and 100 ppm, while lead (Pb) and cobalt (Co) fall between 20 and 30 ppm (Table 1). Chromium (Cr) and nickel (Ni) are particularly enriched due to their affinity for iron and manganese oxides, which act as metal scavengers, and their association with ultramafic sources such as ophiolitic fragments. Zirconium (Zr), often found in zircon minerals, reflects contributions from granitic and felsic sources, whereas barium (Ba) is linked to feldspar weathering and secondary mineral formation.

Compared to rock samples, soil samples exhibit higher concentrations of Al_2O_3, Fe_2O_3, K_2O, MgO, TiO_2, and MnO, as well as an increase in trace metals (except for Sc, Sr, and Ba). These variations are attributed to chemical weathering, leaching, and secondary

Table 1 Statistics of major oxides (%) and trace metals (ppm) of soil and rock samples

		Soil samples				Rock samples			
		Mean	**Min.**	**Max.**	**Std. Dev.**	**Mean**	**Min.**	**Max.**	**Std. Dev.**
Major Oxides (%)	Al_2O_3	13.45	4.28	19.10	3.61	8.23	1.85	13.84	4.77
	CaO	0.73	0.15	4.02	0.90	0.89	0.12	1.69	0.75
	Fe_2O_3	7.20	3.83	11.81	2.11	5.66	2.69	13.81	4.16
	K_2O	1.26	0.02	2.39	0.58	0.92	0.00	1.77	0.59
	MgO	2.31	0.54	10.41	2.09	1.04	0.30	3.30	1.13
	Na_2O	1.01	0.13	1.69	0.44	1.91	0.16	4.28	1.87
	P_2O_5	0.08	0.03	0.15	0.03	0.12	0.05	0.19	0.05
	SiO_2	63.16	35.38	77.56	9.53	66.30	60.78	69.67	4.82
	TiO_2	0.60	0.24	0.88	0.14	0.45	0.10	0.71	0.24
	MnO	0.15	0.02	0.44	0.11	0.13	0.03	0.36	0.14
Trace metals (ppm)	Th	8.32	1.00	15.00	3.77	6.33	1.00	14.00	4.55
	Sc	1	1	1	0	2.5	1	4	1.29
	V	95.41	41.00	164.00	28.44	61.67	7.00	114.00	43.49
	Cr	261.80	85.00	636.00	159.34	118.50	69.00	178.00	36.77
	Co	22.86	9.00	55.00	11.63	12.17	3.00	29.00	11.94
	Ni	85.60	23.00	229.00	53.34	54.33	16.00	110.00	41.05
	Cu	64.62	22.00	212.00	45.79	40.00	22.00	55.00	13.42
	Zn	138.32	64.00	882.00	167.76	76.50	34.00	90.00	21.60
	Rb	65.64	4.00	126.00	31.97	40.50	1.00	92.00	30.74
	Sr	68.3	1	118	26.84	143.8	8	307	136.98
	Zr	172.09	18.00	442.00	91.72	124.17	13.00	309.00	104.34
	Ba	251.14	38.00	373.00	89.19	262.17	45.00	379.00	135.21
	Pb	25.50	3.00	46.00	10.88	20.00	10.00	36.00	9.57

mineral formation. The breakdown of feldspars leads to increased Al_2O_3 content, while Fe_2O_3 and MnO enrichment results from the oxidation and precipitation of iron and manganese oxides, typical of lateritic soil development. The relative increase in K_2O and MgO concentrations suggests the formation of secondary clay minerals and ion adsorption processes, whereas TiO_2 enrichment is due to the residual accumulation of rutile and ilmenite.

The increased trace metal content in soils is influenced by geochemical mobility, adsorption onto clay minerals, and complexation with organic matter. Elements such as Cr, Zn, and Ni show enrichment due to their strong association with iron and manganese oxides, which enhance their retention in soils. In contrast, lower concentrations of Sc, Sr, and Ba in soil samples suggest their retention in feldspar and carbonate minerals within the parent rock, making them less susceptible to weathering and transport. While Sr and Ba are retained within carbonate-hosting beach environments, our results demonstrate their depletion from soils under intense weathering and the lack of carbonate retention phases—reflecting fundamentally different geochemical behaviors in coastal vs. upland settings of the Andaman Islands [41].

To further evaluate the intensity of chemical weathering in soils, sediments, and soil profiles, the Chemical Index of Alteration (CIA) was calculated using the equation proposed by Nesbitt and Young (1984) [42]:

$$CIA = Al_2O_3/(Al_2O_3 + CaO + Na_2O + K_2O \quad (1)$$

The CIA values in the study area range from 67.98 to 87.27, with an average of 81.34 and a standard deviation of 5.15. These values reflect advanced chemical weathering, typical of humid tropical to subtropical conditions, where prolonged exposure to rainfall and surface water facilitates the extensive leaching of mobile elements such as Na, Ca, and K. This process results in the residual enrichment of Al-bearing minerals, particularly kaolinite and gibbsite. Higher CIA values are therefore indicative of intensified hydrolytic alteration, especially in environments characterized by sustained climatic humidity and active surface processes.

Compared to the geochemical profiles reported by Alqahtani and Khalil (2021) [43], which reflect moderate weathering and limited elemental mobility under semi-arid conditions in the Al-Rehaili area of Saudi Arabia, the Middle Andaman samples exhibit significantly higher CIA values, greater depletion of base cations (Na, Ca, Sr), and notable Fe–Mn oxide enrichment. These differences underscore the impact of a more aggressive tropical weathering regime and the tectonically active forearc setting in the Andaman region, contributing to more mature soil development and mineralogical transformation.

4.2.1 Soil geochemical analysis

Several geochemical diagrams were plotted to interpret the relative chemical constituents of the examined soil samples and classify their lithological characteristics.

4.2.1.1 TiO_2 vs. Al_2O_3 plot This diagram was used to distinguish between mudstone and sandstone compositions (Fig. 6a) [44]. The results indicate that sandstone is the dominant lithological component in all analyzed soil samples, highlighting a siliciclastic sedimentary influence in the region.

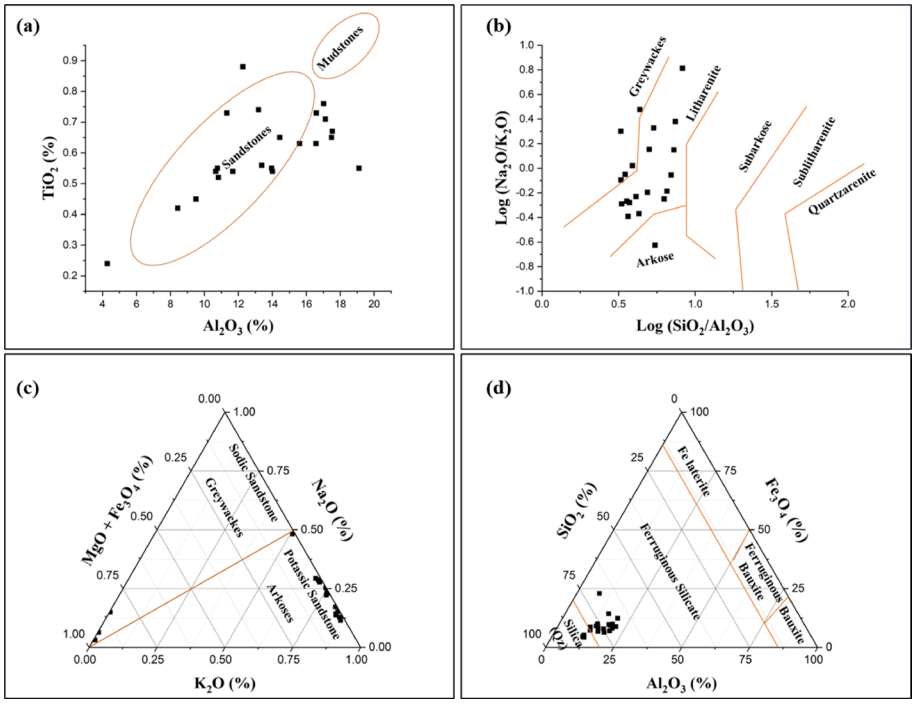

Fig. 6 **a** Binary plot of TiO_2 vs. Al_2O_3, illustrating the geochemical relationship between these oxides in soil samples; **b** Binary diagram of log (SiO_2/Al_2O_3) vs. log (Na_2O/K_2O), indicating weathering trends and feldspar alteration; **c** Ternary diagram of K_2O - (Fe_2O_3 + MgO) - Na_2O, reflecting sediment source and mineralogical composition; **d** Ternary plot of Fe_2O_3 - SiO_2 - Al_2O_3, showing geochemical differentiation and potential sedimentary processes in the study area

4.2.1.2 Binary diagram of log (SiO_2/Al_2O_3) vs. log (Na_2O/K_2O) This plot was employed to categorize different types of sandstones [45, 46]. The majority of analyzed samples fall within the litho-arenite sandstone field, while greywacke and arkose compositions were identified in five and one samples, respectively (Fig. 6b). This distribution suggests varying degrees of mineralogical maturity and sedimentary provenance, with litho-arenites indicating moderate to high quartz content and feldspar depletion.

4.2.1.3 Ternary diagram of K_2O - (Fe_2O_3 + MgO) - Na_2O This classification method was used to distinguish different silicate compositions [47, 48]. The ternary diagram confirms that most soil samples correspond to potassic ferromagnesium sandstone (Fig. 6c), suggesting a sedimentary source enriched in potassium feldspars, iron-bearing silicates, and mafic minerals.

4.2.1.4 Ternary plot of Fe_2O_3–SiO_2–Al_2O_3 This diagram primarily categorizes the samples based on their iron, silica, and aluminum oxide content [49]– [50]. The results show that most of the samples fall within the ferruginous silicate field, suggesting significant iron oxide contributions from lateritic weathering and sedimentary processes. However, three samples fall within the quartz silica field (Fig. 6d), indicating high silica concentrations and potentially more mature or reworked sediments.

4.2.2 Source area weathering and mineral composition

Geochemical analyses of soil samples were conducted to assess weathering intensity and mineral composition. Various binary and ternary diagrams were utilized to determine

the extent of chemical weathering and identify dominant mineral constituents in the study area.

4.2.2.1 Ternary diagram of CaO - Al_2O_3 - K_2O This plot was used to evaluate the degree of chemical weathering [51]. The majority of the analyzed samples exhibit strong weathering, with some samples falling within the intermediate weathering zone (Fig. 7c). This trend suggests prolonged exposure to tropical and subtropical weathering processes, which are characteristic of feldspar breakdown and clay mineral formation.

4.2.2.2 Binary plot of al_2o_3 vs. K_2O The mineralogical composition was further assessed using this binary diagram [1]. Most samples are positioned between the feldspar and muscovite compositional range, indicating intermediate to strong degrees of weathering (Fig. 7a). A few samples lie closer to feldspar and muscovite fields, reflecting varying degrees of alteration and leaching of alkali elements. The relative abundance of muscovite and feldspar suggests significant alumino-silicate weathering, characteristic of granitic and metamorphic parent materials.

4.2.2.3 Ternary diagram of K_2O - ($CaO + Na_2O$) - Al_2O_3 This plot was used to assess weathering trends and source rock compositions. The samples predominantly indicate intermediate to strong weathering, consistent with mineral leaching and feldspar decomposition under humid climatic conditions. The loss of CaO and Na_2O suggests the

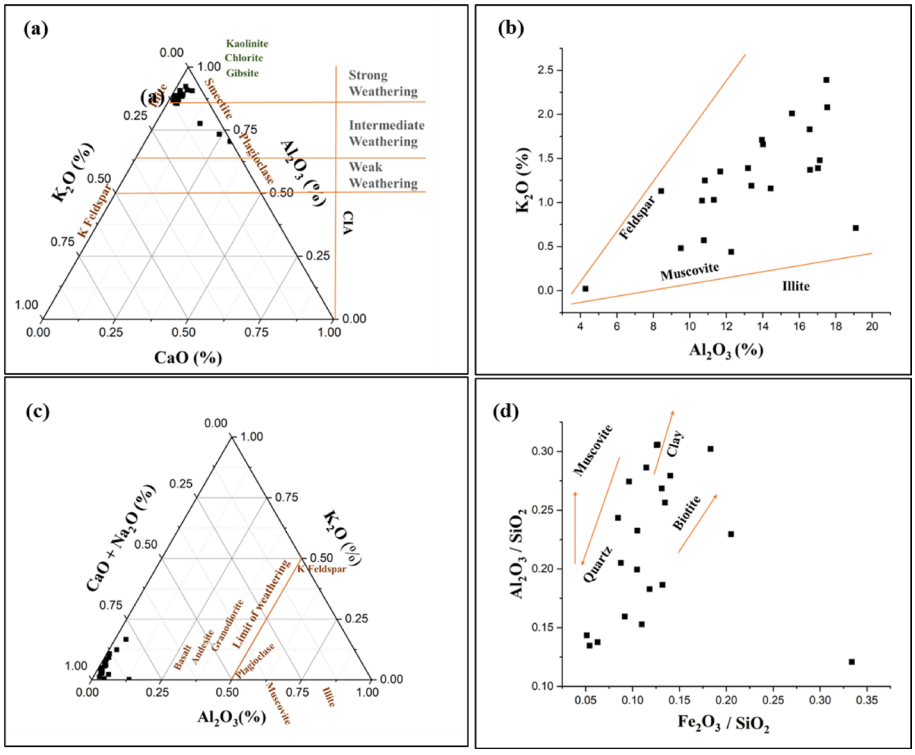

Fig. 7 Ternary diagram of CaO - Al_2O_3 - K_2O, illustrating the geochemical classification and weathering trends of soil samples; **b** Binary plot of Al_2O_3 vs. K_2O, indicating the mineralogical association of clay and feldspar components; **c** Ternary diagram of K_2O - ($CaO + Na_2O$) - Al_2O_3, reflecting sediment provenance and weathering intensity; **d** Binary plot of Al_2O_3/SiO_2 versus Fe_2O_3/SiO_2, showing geochemical differentiation and alteration processes in soil samples

transformation of primary minerals into secondary clay minerals, further reinforcing the degree of chemical weathering.

4.2.2.4 Binary diagram of al_2o_3/sio_2 vs. Fe_2O_3/SiO_2 This plot was used to differentiate the source mineralogy of the examined samples. The majority of soil samples are composed of quartz and clay minerals (Fig. 7d). This indicates that the parent material has undergone significant silicate weathering, resulting in the depletion of less stable minerals and enrichment of residual quartz and alumino-silicates. The high Fe_2O_3/SiO_2 ratios in some samples also suggest contributions from iron-rich sources, likely derived from lateritic weathering processes.

4.2.3 Climate and effects of diagenesis

The paleoclimatic conditions during sediment deposition and the post-depositional diagenetic processes were assessed using geochemical proxies and binary diagrams. These analyses help to understand how climatic factors influenced sediment composition and how diagenetic alterations modified the geochemical signatures of the soils in Middle Andaman.

4.2.3.1 Paleoclimate Estimation using sio_2 vs. $(Al_2O_3 + K_2O + Na_2O)$ binary diagram The binary plot of SiO_2 against $(Al_2O_3 + K_2O + Na_2O)$ was employed to reconstruct the paleoclimatic conditions during the formation of the soil deposits [46, 52]. The majority of the analyzed soil samples fall within the semi-arid climatic zone, with certain patches indicating a semi-humid environment, similar to Alqahtani and Khalil's classification [43] (Fig. 8b). The relatively high Chemical Index of Alteration (CIA) values in the Andaman samples (67.98–87.27; avg. 81.34) suggest stronger chemical weathering, likely driven by monsoonal rainfall, in contrast to the more arid Red Sea setting where only moderate weathering was observed.

This distribution indicates that the sedimentary materials experienced moderate to intense weathering, likely influenced by seasonal variations in precipitation and temperature. The semi-arid signature implies limited chemical alteration, whereas the presence of semi-humid indicators in some samples suggests episodic increases in humidity, which may have enhanced weathering intensity and leaching of mobile elements.

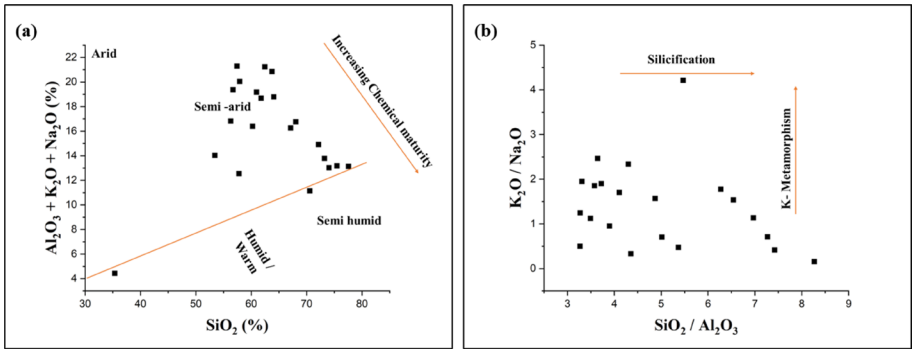

Fig. 8 Binary diagram of SiO_2 vs. $(Al_2O_3 + K_2O + Na_2O)$, illustrating the geochemical classification and weathering trends of soil samples; **b** Logarithmic binary diagram of log (K_2O/Na_2O) versus log (SiO_2/Al_2O_3), depicting sediment maturity and compositional variations in the study area

4.2.3.2 Post-depositional alterations and diagenesis Sediments and soil profiles undergo significant post-depositional modifications, altering their primary geochemistry. Two key diagenetic processes—K-metasomatism and silicification—were identified as major factors influencing the mineral composition of the region's soils and sediments.

4.2.3.3 K-Metasomatism This process involves the introduction of potassium (K_2O) into the sediments through post-depositional reactions, often linked to hydrothermal activity or syn-depositional water interactions at lower temperatures [52]. The replacement of primary feldspars with K-feldspar or illite results in potassium enrichment, altering the bulk geochemistry of the sediments.

4.2.3.4 Silicification The influx of silica (SiO_2) during diagenesis leads to the replacement of pre-existing minerals with secondary quartz or chalcedony. This process occurs due to hydrothermal fluids or prolonged interaction with percolating groundwater, promoting silica precipitation and hardening of sedimentary layers.

4.2.3.5 Binary diagram of log (K_2O/Na_2O) vs. log (SiO_2/Al_2O_3) This plot was used to assess the post-depositional diagenetic processes, specifically interactions of the sediments with water at low temperatures (Fig. 8a). The data reveal significant potassium enrichment in certain samples, indicating that K-metasomatism played a role in altering the mineral composition. Additionally, some samples display enhanced SiO_2 values, confirming silicification as an influential post-depositional modification.

4.2.4 Environments of deposition

The depositional environments of the Middle Andaman sediments were characterized using multiple geochemical proxies. The MgO vs. Fe_2O_3/Al_2O_3 binary plot indicates that most samples represent non-marine deltaic sandstones, with the exception of one outlier (Fig. 9a) [52–54]. This interpretation is further supported by the log–log plot of MgO/Al_2O_3 vs. K_2O/Al_2O_3, which confirms the non-marine deltaic classification for all samples (Fig. 9b) [49, 55]. These results align with the fluvial–deltaic depositional environment proposed by Alqahtani and Khalil [43], although the Middle Andaman samples display reduced marine influence and more consistent redox trends.

Additionally, the ternary Fe_2O_3 – (SiO_2/Al_2O_3) – MgO diagram supports this classification (Fig. 9c) [47, 54]. Paleo-redox conditions, evaluated using a V/Cr vs. Ni/Co binary plot, indicate predominantly oxic environments, though a few samples reflect dysoxic to anoxic conditions (Fig. 9d) [56–58]. These findings suggest that the Middle Andaman sediments were primarily deposited in deltaic, non-marine settings under variable redox conditions, reflecting shifts in environmental and hydrodynamic processes.

4.2.5 Paleosols and climate

Paleosols, or ancient soils preserved in the geological record, are crucial indicators of past climatic conditions, landscape evolution, and soil formation processes. In the Middle Andaman region, the presence of multilevel paleosols suggests periodic climate shifts, particularly transitions between semi-arid and semi-humid conditions, which influenced soil development and weathering intensity. Compared to the findings of Alqahtani and Khalil (2021) [43], where paleosols reflect limited humidity and

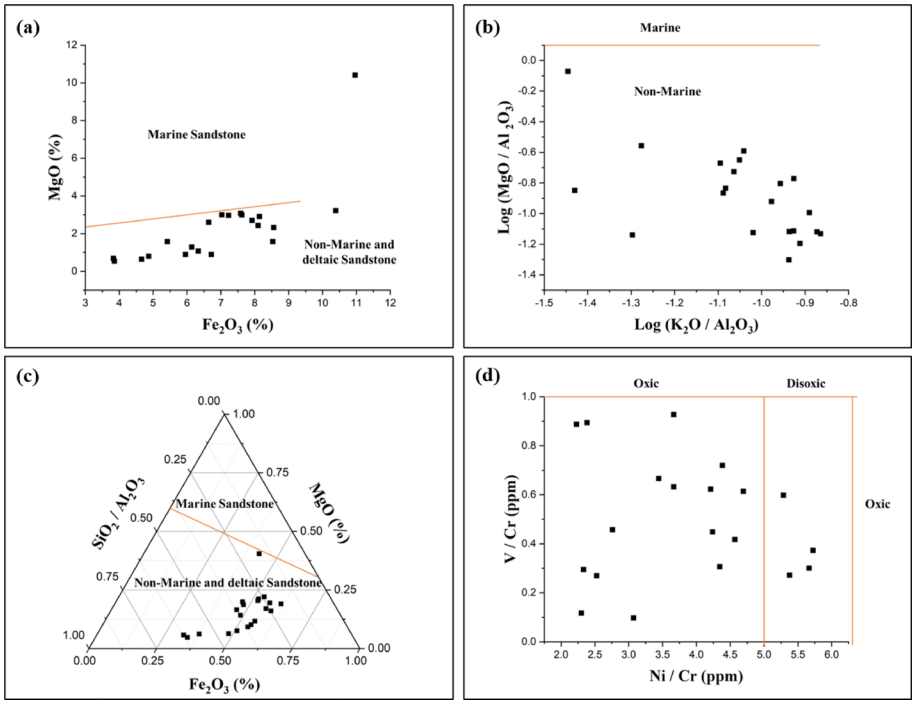

Fig. 9 **a** Binary plot of MgO vs. Fe_2O_3/Al_2O_3, illustrating the geochemical relationship between magnesium and iron oxides; **b** Logarithmic binary plot of MgO/Al_2O_3 versus K_2O/Al_2O_3, highlighting weathering intensity and mineralogical variations; **c** Ternary diagram of Fe_2O_3 - (SiO_2/Al_2O_3) - MgO, showing compositional trends and sediment provenance; **d** Biary plot of V/Cr versus Ni/Co, indicating redox conditions and trace metal behavior in the soil samples

fewer pedogenic phases, the Andaman profiles exhibit more advanced clay mineral formation and greater hydrological variability. These characteristics underscore a stronger monsoonal influence and a more dynamic weathering regime typical of island arc environments.

Geochemical proxies, such as the Chemical Index of Alteration (CIA), which ranges from 67.98 to 87.27, indicate moderate to intense chemical weathering, further supporting this interpretation. The predominance of minerals such as kaolinite, illite, and smectite reflects variability in precipitation and leaching intensity, while Fe_2O_3/SiO_2 and Al_2O_3/SiO_2 ratios highlight temporal differences in chemical weathering intensity. The paleosols in this region exhibit moderate to strong weathering, with detrital muscovite, quartz, and secondary clay minerals suggesting progressive pedogenesis and episodic hydrological changes. These findings point to the significant role of climatic fluctuations in shaping sediment deposition and influencing soil development in the Middle Andaman region.

4.2.6 Hierarchical cluster analysis (HCA)

Hierarchical Cluster Analysis (HCA) is a valuable method for identifying spatial similarities in geochemical data by grouping samples based on statistical significance. In this study, HCA classified the dataset into nine distinct clusters, allowing for meaningful interpretation with minimal data loss (Fig. 10). The first cluster primarily represents weathering of geochemically similar minerals, including CaO-MgO, Fe-Ti oxides (Fe_2O_3/Fe_3O_4-TiO_2), silicates (SiO_2-MnO), alumino-silicates (Al_2O_3-K_2O), and phosphates (Na_2O-P_2O_5). Since Fe_2O_3 and Fe_3O_4 coexist in weathering environments, further

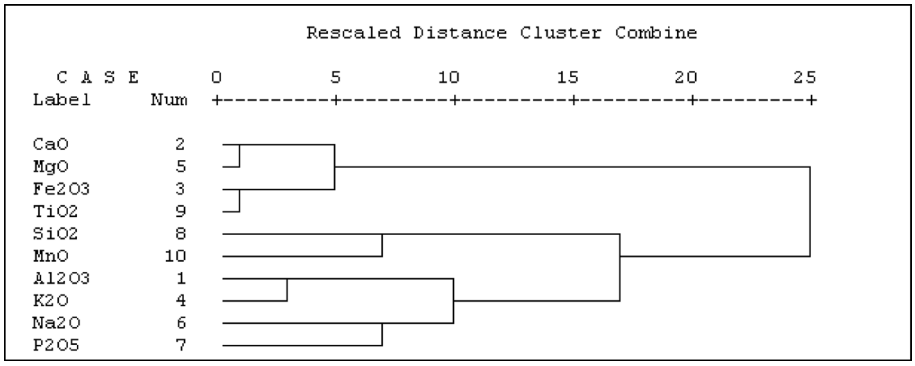

Fig. 10 Hierarchical Cluster Analysis (HCA) of major oxides in soil samples, depicting geochemical grouping and mineral associations that influence soil composition and weathering processes in the study area

Table 2 Rotated component matrix of principal component analysis (PCA) for major oxides and trace metals in soil samples, illustrating the geochemical clustering and elemental associations influencing sediment composition and weathering processes

Metal oxides	Component			
	1	2	3	4
Al_2O_3	0.093	**0.933**	0.121	0.052
CaO	**0.81**	-0.25	-0.313	-0.171
Fe_2O_3	**0.813**	0.334	-0.239	0.254
K_2O	-0.194	0.491	**0.753**	0.236
MgO	**0.918**	0.048	-0.237	-0.28
Na_2O	0.019	0.045	0.103	-0.908
P_2O_5	-0.236	-0.112	0.85	-0.277
SiO_2	-0.516	-0.665	-0.013	0.328
TiO_2	**0.839**	0.267	-0.004	0.351
MnO	**0.543**	-0.535	0.236	0.459
Initial Eigenvalues	3.915	2.222	1.581	1.066
Total Variance (%)	39.146	22.216	15.815	10.664
Cumulative variance (%)	39.146	61.362	77.177	87.841

Trace metals	Rotated Component Matrix(a)		
	Component		
	1	2	3
Th	**0.548**	0.385	**0.742**
Sc	0.048	**0.863**	0.148
V	**0.582**	**0.598**	**0.531**
Cr	-0.082	0.098	**0.902**
Co	-0.606	-0.486	-0.627
Ni	0.066	**0.839**	0.35
Cu	0.264	**0.63**	**0.711**
Zn	-0.941	-0.253	0.192
Rb	**0.868**	-0.04	0.487
Sr	0.346	**0.928**	-0.026
Zr	-0.456	-0.706	-0.537
Ba	**0.896**	0.175	0.027
Pb	**0.88**	0.238	0.409
Initial Eigenvalues	8.547	2.137	1.477
% of Variance	35.632	31.604	26.304
Cumulative %	35.632	67.236	93.54

mineralogical analysis is needed for their precise distinction. The second cluster identifies the source rocks contributing to the mineral deposits, while the third cluster reflects geological formations, specifically the Bhartang Formation and associated sedimentary deposits. The final stage of the analysis reveals geological processes, such as island formation, potentially linked to magmatic or volcanic activity. Overall, HCA proves to be an effective method for understanding the spatial and geochemical relationships within the region, aiding in the interpretation of the underlying geological processes.

4.2.7 Factor analysis (PCA) of major oxides of soil samples

The Factor Analysis (PCA) of major oxides in soil samples revealed four components with eigenvalues of 3.915, 2.216, 1.581, and 1.066, and respective variances of 39.146%, 22.216%, 15.815%, and 10.664% (Table 2). The first component primarily grouped CaO, Fe_2O_3, MgO, TiO_2, and MnO, suggesting these oxides originate from a common source, likely linked to the weathering of primary igneous and metamorphic rocks. This component indicates that these oxides are typically associated with silicate minerals undergoing alteration processes. The second and third components are related to Al_2O_3 and

K_2O, which are often products of silicate weathering and sea salt spray in coastal environments. This highlights the influence of marine conditions on the geochemistry of the region, where weathering of feldspars and clay minerals contributes to the presence of these oxides in the soil.

In the PCA analysis of trace metals, three components were identified, with eigenvalues of 8.547, 2.137, and 1.477, and corresponding variances of 35.632%, 31.604%, and 26.304%, respectively. The first component shows that trace metals such as Th, V, Rb, Ba, and Pb are derived from a common source, predominantly igneous rocks. These elements are typically enriched in such rocks and can be mobilized during weathering and erosion processes. The second component suggests that Sc, V, Ni, Cu, and Sr are also sourced from igneous rocks but may be influenced by different processes, such as hydrothermal alteration or leaching. The third component identified Th, V, Cr, and Cu as originating from a separate source, possibly from secondary mineralization or different geological formations. This reflects the complex behavior and mobility of trace metals in the region, where multiple sources contribute to their presence in the soil, influenced by both natural and weathering processes. The results of this PCA provide a clearer understanding of the geochemical processes at play, highlighting the interrelationships between major oxides and trace metals, as well as the contributions of various geological and environmental factors.

4.2.8 Correlation matrix of major oxides of soil samples

The correlation matrix of major oxides and trace metals, presented in Table 3, reveals significant geochemical interactions within the study area. Strong positive correlations are observed between Al_2O_3-K_2O, Al_2O_3-TiO_2, CaO-Fe_2O_3, CaO-MgO, Fe_2O_3-MgO, Fe_2O_3-MnO, K_2O-P_2O_5, MgO-TiO_2, MgO-MnO, Th-Rb, Th-Zr, Th-Ba, Th-Pb, V-Ni, Co-Ni, Co-Cu, Ni-Cu, Rb-Zr, Rb-Ba, Rb-Pb, Zr-Ba, Zr-Pb, and Ba-Pb. Conversely, negative correlations are found between Al_2O_3-MnO, CaO-K_2O, CaO-P_2O_5, CaO-SiO_2, Fe_2O_3-SiO_2, MgO-SiO_2, SiO_2-MnO, Th-Co, Th-Ni, Th-Cu, Co-Rb, Co-Zr, Co-Pb, Ni-Rb, Ni-Zr, Ni-Pb, Cu-Rb, Cu-Zr, and Cu-Pb.

These correlations highlight the geochemical affinities and mineral associations present in the Middle Andaman region. The positive correlation between Al_2O_3 and K_2O suggests their common occurrence in clay minerals such as illite and kaolinite, indicative of moderate to intense weathering processes. Similarly, the CaO-Fe_2O_3 and CaO-MgO relationships point to their co-occurrence in carbonate and ferromagnesian minerals, playing a crucial role in soil geochemistry. The strong correlation between Th and elements like Rb, Zr, and Ba suggests their association with heavy mineral phases such

Table 3 Correlation matrix of major oxides and trace metals in soil samples, highlighting geochemical affinities, mineral associations, and element interrelationships within the study area

	Al_2O_3	CaO	Fe_2O_3	K_2O	MgO	Na_2O	P_2O_5	SiO_2	TiO_2	MnO
Al_2O_3	1.00									
CaO	-0.19	1.00								
Fe_2O_3	-0.09	**0.65**	1.00							
K_2O	**0.68**	**-0.53**	-0.39	1.00						
MgO	0.07	**0.93**	**0.80**	-0.39	1.00					
Na_2O	0.46	-0.02	-0.36	0.18	0.28	1.00				
P_2O_5	0.18	**-0.53**	-0.48	**0.61**	-0.40	0.13	1.00			
SiO_2	0.18	**-0.50**	**-0.85**	0.34	**-0.66**	0.46	0.34	1.00		
TiO_2	**0.63**	0.34	0.13	0.38	**0.85**	0.49	0.13	0.10	1.00	
MnO	**-0.58**	0.48	0.63	-0.39	**0.56**	-0.36	-0.15	**-0.64**	-0.23	1.00

	Th	Sc	V	Cr	Co	Ni	Cu	Zn	Rb	Sr	Zr	Ba	Pb
Th	1.00												
Sc	0.24	1.00											
V	0.00	-0.36	1.00										
Cr	-0.36	-0.04	-0.02	1.00									
Co	**-0.68**	-0.23	0.28	-0.05	1.00								
Ni	**-0.70**	-0.32	**0.67**	0.10	**0.89**	1.00							
Cu	-0.64	-0.24	0.38	0.00	**0.92**	**0.86**	1.00						
Zn	-0.42	-0.06	-0.36	-0.15	0.28	0.17	0.49	1.00					
Rb	**0.94**	0.04	0.17	-0.45	**-0.56**	**-0.54**	**-0.53**	-0.39	1.00				
Sr	0.48	0.13	0.28	0.16	-0.52	-0.41	-0.32	-0.39	0.42	1.00			
Zr	**0.72**	0.30	-0.18	0.26	**-0.66**	**-0.73**	**-0.60**	-0.39	**0.57**	0.49	1.00		
Ba	**0.82**	0.07	0.22	-0.49	-0.42	-0.38	-0.46	**-0.51**	**0.86**	0.39	**0.54**	1.00	
Pb	**0.84**	0.12	0.12	-0.32	-0.56	**-0.51**	**-0.60**	-0.43	**0.86**	0.47	**0.55**	**0.76**	1.00

as monazite and zircon, reflecting the influence of felsic igneous sources in sediment formation.

Negative correlations indicate contrasting geochemical behaviors or competitive substitution within mineral structures. The inverse relationship between CaO and SiO_2 suggests that silica enrichment is linked to quartz-dominated soils rather than carbonate-rich compositions. Similarly, the negative correlation between Th and Co/Ni may reflect differences in their provenance, with Th being more enriched in felsic environments, while Co and Ni are commonly associated with mafic-ultramafic rock formations. These findings align with the broader geochemical framework of the Middle Andaman region, where sedimentary, metamorphic, and igneous contributions shape the soil composition and mineral interactions.

4.3 Soil profile analysis

The soil profile analysis was carried out on two core samples to assess the vertical distribution of mineral oxides. The XRD plot of the core samples is shown in Fig. 3, with the location map provided in Fig. 1. Core sample CR-2-1 to CR-2-2 had a depth of approximately 4 cm, while the thickness profile for samples SS-9 A to SS-9D ranged from 4 cm to 6 cm. The percentage oxide data for these core samples are presented in Table 1, and their comparative graphs are illustrated in Fig. 11.

In soil profile (Fig. 11a) (sample SS-9), the oxides Al_2O_3, CaO, Fe_2O_3, K_2O, MgO, Na_2O, and TiO_2 generally decreased with increasing depth from SS-9 A to SS-9D. A slight increase in most oxides was observed from SS-9 C to SS-9D, indicating the percolation and accumulation of oxides from the surface layer to the deeper layers. Phosphorus pentoxide (P_2O_5) showed a fluctuating pattern, increasing at SS-9B, then decreasing at SS-9 C, and increasing again at SS-9D. Manganese oxide (MnO) increased with depth up to SS-9 C and slightly decreased at SS-9D. Silica oxide (SiO_2) exhibited a rise in the second layer before decreasing at SS-9D.

In core sample (Fig. 11b) (CR-2), the profile consisted of two layers within a 6 cm depth. From the top layer (CR-2-1) to the deeper layer (CR-2-2), there was an increase in the percentage of oxides such as Al_2O_3, CaO, Fe_2O_3, K_2O, Na_2O, P_2O_5, and TiO_2, suggesting enhanced weathering or percolation of these elements downward. In contrast, oxides like MgO, SiO_2, and MnO showed a decrease in percentage from the top to the bottom layer, indicating a selective distribution or leaching of these oxides within the soil profile. These observations provide insights into the vertical distribution and mobility of various

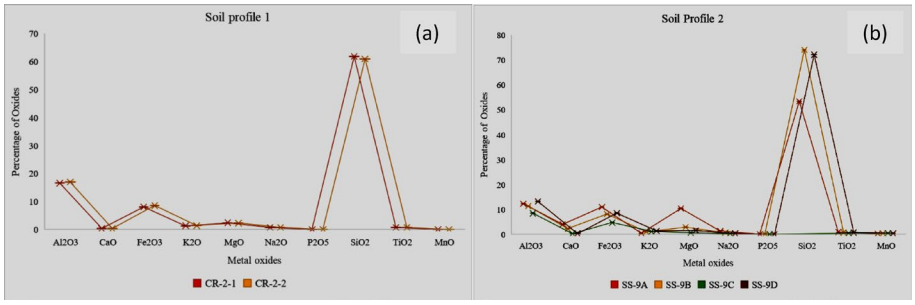

Fig. 11 Major oxides distribution in **a** Soil Profile 1 and **b** Soil Profile 2, illustrating geochemical variations and weathering trends in the study area

oxides, suggesting dynamic weathering and percolation processes at play in the region's soil formation.

4.4 Thin section analysis of rock samples

Thin section analysis offers valuable insights into the mineral characteristics, composition, texture, and weathering of rocks [59]. It examines the grain shape, size, orientation, interlocking degree, and relative proportions of minerals in the rock matrix. This method helps determine rock texture across different lithologies, as well as the correlation between texture coefficient and uniaxial compressive strength, which can be used to estimate the rock weathering index [60].

In the current study, thin section observations reveal a mineral assemblage dominated by alumina and silica (Fig. 12). The presence of thorium suggests a volcanic origin, while the low titanium dioxide content points to silica-rich, rhyolitic parent rocks (Fig. 12a and b). Petrographic analysis identifies several key mineral features based on color: black indicates iron oxide (Fig. 12g, 12h), white represents silica, green corresponds to ferromagnesian minerals (Fig. 12e and f), basal cleavage is associated with mica, and grayish tones are indicative of feldspar (Fig. 12c and d). The mineral orientation and characteristics do not support a metamorphic origin; instead, they suggest a mixed composition from igneous and sedimentary sources, likely entrapped within magma during formation.

Opaque minerals like chromite are found embedded in serpentinite and ophiolite, along with green minerals typical of serpentinite and ferromagnesian compositions. This mineral assemblage suggests past water infiltration, potentially facilitated by microseismic activity caused by fault shifts or fluid movements in the rock. The presence of biotite, chromite, clinoptilolite, and corundum highlights interactions between various rock types under changing temperature, pressure, and seismic conditions, emphasizing the role of tectonic activity in shaping the study area's aquifer systems [61].

High-grade metamorphism is also evident in the thin sections, with minerals such as actinolite, albite, biotite, and celestite. The combination of chromite, spinel, albite, actinolite, and hedenbergite suggests the intrusion of ultramafic mineral assemblages—rich in magnesium- and iron-bearing silicates—into sedimentary formations (Fig. 12g, 12h). Cementing minerals like calcite, iron oxide-rich carbonates, anhydrite, barite, and various clays further complicate the rock's geological history, highlighting deposition, diagenesis, and tectonic reworking [62]. These findings underscore the dynamic geological processes—both internal and external—that have shaped the region. Thin section analysis provides insights into the mineral characteristics, composition, arrangement, porosity, textures, and weathering states of rocks [59]. It describes grain shape, size, orientation, degree of interlocking, and their relative proportions within the matrix. Additionally, it helps determine rock texture across different lithologies, the correlation between texture coefficient and uniaxial compressive strength, and the application of texture coefficient for estimating the rock weathering index [60].

Thin section observations reveal a mineral assemblage rich in alumina and silica (Fig. 12). The presence of thorium suggests a volcanic origin, while the low titanium dioxide content indicates silica-rich or rhyolitic parent rocks (12a, 12b). Petrographic analysis identifies distinct mineralogical features based on color: black represents iron oxide (12g, h), white denotes silica, green corresponds to ferromagnesian minerals (12e,

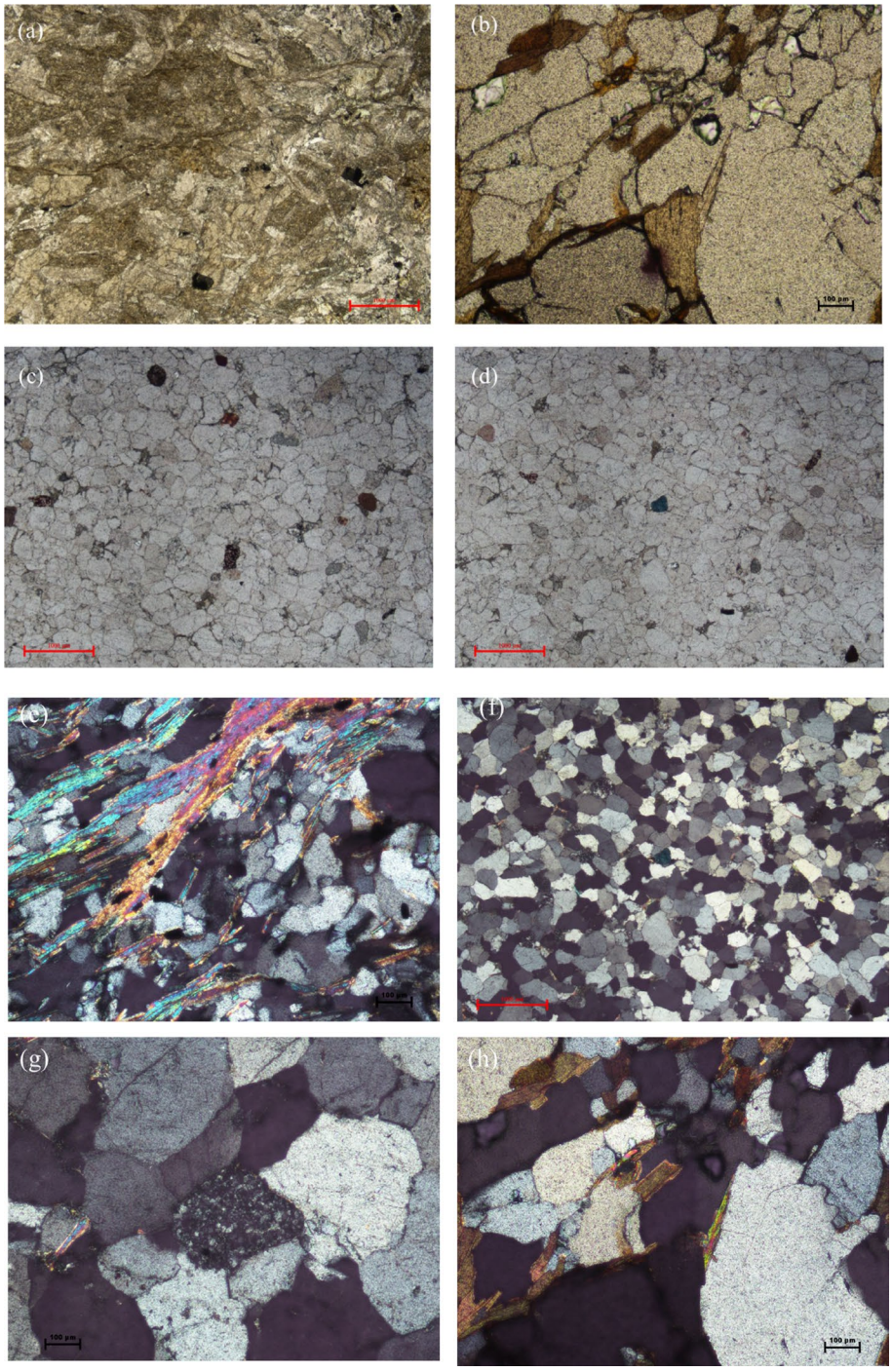

Fig. 12 Photomicrographs of rock samples in the study area, labeled with corresponding rock types and mineralogical compositions: **a** Jasper, an aggregate of microgranular quartz, and **b** Rhyolite, both rich in alumina and silica, indicating a volcanic origin; **c** Feldspathic sandstone with feldspar grains and **d** Arkosic sandstone containing feldspar and quartz, suggesting igneous or sedimentary influences; **e** Serpentinite with green ferromagnesian minerals and **f** Ultramafic rock with distinct mineralogical textures, characteristic of ultramafic assemblages; **g** Iron-rich schist with hematite deposits and **h** Manganese-bearing metasedimentary rock, highlighting secondary mineralization through iron oxide deposits; **i** Calcite-cemented limestone and **j** Schist with foliated texture containing mica and quartz, reflecting cementing minerals such as calcite, anhydrite, and barite, indicative of diagenetic and depositional processes

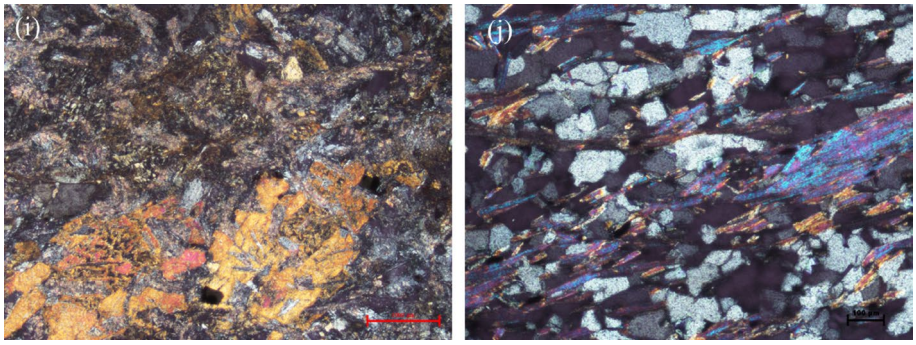

Fig. 12 (continued)

f), basal cleavage is associated with mica, and grayish tones indicate feldspar (12c, d). The mineral orientation and characteristics do not indicate a metamorphic origin; instead, they suggest a mixed composition derived from igneous and sedimentary sources, likely entrapped within magma during formation.

Opaque minerals, such as chromite, are embedded within serpentinite and ophiolite, accompanied by green minerals characteristic of serpentinite and ferromagnesian compositions. This mineral assemblage suggests past water infiltration, likely facilitated by microseismic activity—small-scale seismic movements often caused by fault shifts or fluid movements within rock formations. The presence of biotite, chromite, clinoptilolite, and corundum indicates interactions between multiple rock types under varying temperature, pressure, and seismic conditions. These mineralogical features underscore the role of tectonic activity in shaping the aquifer systems of the study area [61].

Evidence of high-grade metamorphism is also apparent in the thin sections, as indicated by minerals such as actinolite, albite, biotite, and celestite. The association of chromite, spinel, albite, actinolite, and hedenbergite suggests the intrusion of ultramafic mineral assemblages—rock formations composed predominantly of magnesium- and iron-rich silicate minerals—into sedimentary formations (12g, h). The presence of cementing minerals—including calcite, iron oxide-rich carbonates, anhydrite, barite, and various clays—further highlights the complexity of the geological processes involved (12i, j) [62]. These findings indicate a history of deposition, diagenesis, and tectonic reworking, shaped by both internal and external geological processes [63].

4.5 Dissolution and deposition

Groundwater sampling locations were selected based on surface indicators identified through satellite imagery and accessibility considerations. A total of 25 samples were collected across Middle Andaman, comprising 24 groundwater samples and one seawater sample for reference. To prevent contamination, groundwater samples were obtained from wells and boreholes using pre-cleaned polyethylene bottles. The saturation index (SI), which helps determine the equilibrium between groundwater and minerals, was calculated using PHREEQC Version 3. The analysis focused on major ions and trace metals present in the minerals. Figures 13 and 14 show the saturation status of minerals in the Middle Andaman region.

Undersaturated minerals (SI < -5), such as Alunite, Aragonite, Calcite, $Fe(OH)_3$, Gibbsite, Goethite, Hematite, and Rhodochrosite, indicate a tendency to dissolve into groundwater. This dissolution process releases calcium and aluminum ions, significantly

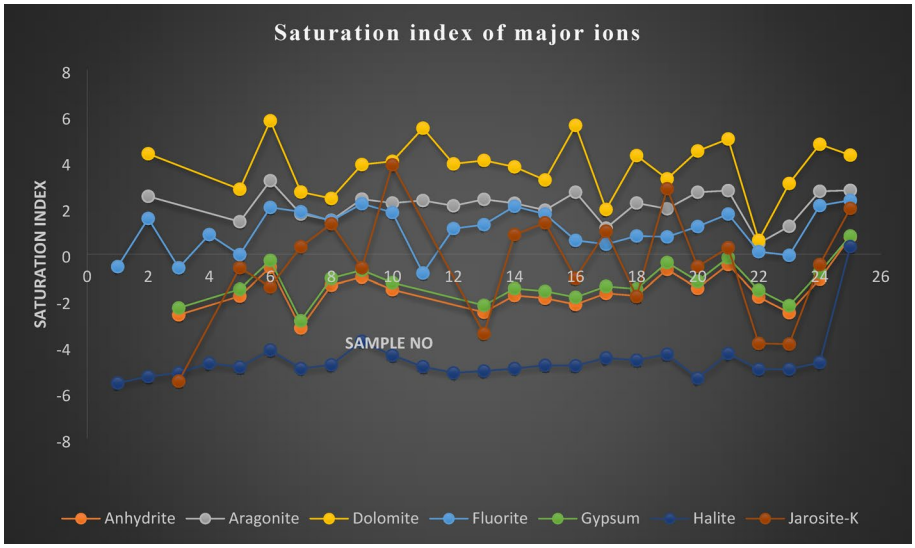

Fig. 13 Saturation index of major ions in groundwater samples, highlighting the saturation states of key mineral phases and their role in controlling groundwater chemistry through dissolution and precipitation processes in the study area

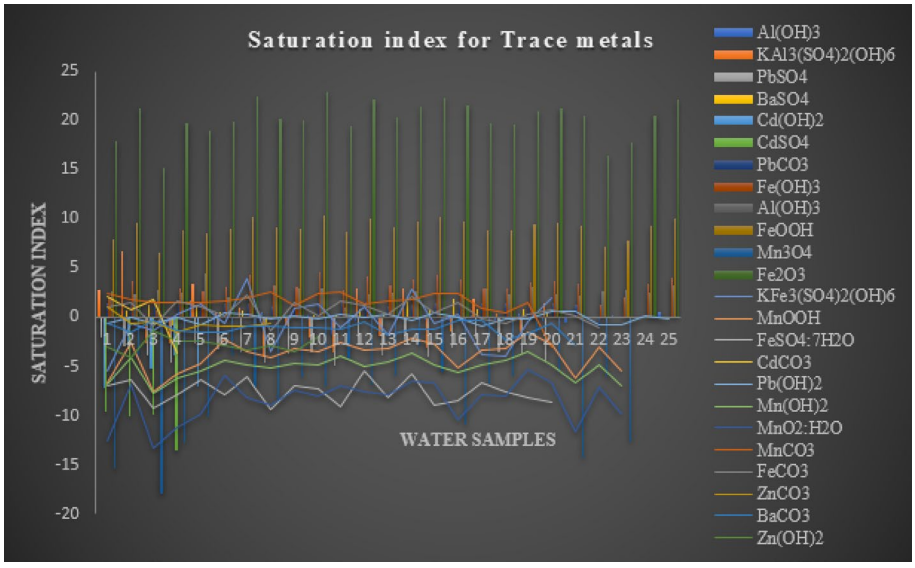

Fig. 14 Saturation index of trace metal ions in groundwater samples, illustrating the supersaturation and undersaturation states of various metal-bearing minerals, which influence precipitation and dissolution processes in the study area

influencing groundwater hardness, pH, and overall geochemical composition, all of which are vital for understanding aquifer dynamics and water resource management.

In contrast, oversaturated minerals (SI > 2), including $Cd(OH)_2$, Halite, Hausmannite, Manganite, Pyrochroite, Pyrolusite, and Sylvite, are prone to precipitation, leading to mineral deposition within the aquifer. This deposition can decrease permeability and porosity, thereby affecting groundwater flow and recharge rates. The oversaturation of trace metals like cadmium and manganese also raises concerns about groundwater contamination, as elevated levels of cadmium can pose significant environmental and health risks.

4.6 Major ions and trace metal constituents in sub-surface hydrology

The groundwater quality in the subsurface aquifer is assessed through key parameters that provide insight into its chemical characteristics and potential influences. The pH levels range from 6.20 to 8.50, with an average of 7.44, indicating predominantly neutral water, though slight variations towards acidity or alkalinity suggest interactions with surrounding geological formations and possible buffering by carbonate minerals. Electrical conductivity (EC) varies between 100 and 1500 µS/cm, with an average of 525 µS/cm, reflecting the concentration of dissolved ions, which is influenced by mineral dissolution, weathering processes, and potential seawater intrusion. Total dissolved solids (TDS) range from 30 to 740 mg/L, averaging 272.5 mg/L, signifying variations in groundwater recharge, rock-water interactions, and evaporation effects [7, 29].

Major ion concentrations further support these geochemical trends. Sodium (Na) levels range from 3.00 to 90.30 mg/L, with a mean of 26.88 mg/L, while calcium (Ca) concentrations vary from 10.02 to 213.43 mg/L, averaging 104.25 mg/L. These values indicate the influence of lithology, particularly carbonate and silicate minerals, in regulating groundwater composition.

Trace metal concentrations highlight potential natural and anthropogenic inputs. Iron (Fe) ranges from 0.02 to 5.85 mg/L, with an average of 0.79 mg/L, and manganese (Mn) varies from below detection limit (BDL) to 1.31 mg/L, averaging 0.30 mg/L. Elevated levels of Fe and Mn in some samples suggest possible leaching from lateritic soils, iron-bearing minerals, or contamination from industrial or domestic sources. Additionally, lead (Pb) and selenium (Se) have mean concentrations of 0.05 mg/L and 0.03 mg/L, respectively, raising concerns due to their toxicity even at trace levels [7, 29].

The relatively low concentrations of nitrates (NO_3) and chlorides (Cl) indicate limited agricultural or industrial contamination, suggesting that the aquifer remains largely unaffected by anthropogenic pollutants.

4.7 Trace metal contamination in seawater

Trace metal contamination in seawater significantly affects the health of coastal and estuarine ecosystems, with concentrations influenced by both natural processes and anthropogenic activities. Soil particles act as carriers of trace metals, and their accumulation is shaped by factors like tectonic activities, soil texture, mineral composition, and physical transport mechanisms [64, 65]. These metals enter the marine environment through various pathways, including physico-chemical adsorption, biological uptake, and direct physical accumulation. Studies on the Andaman Islands provide valuable insights into the sources of trace metal contamination in seawater. For example, research on seagrass in the region suggests that, in general, the marine environment remains relatively non-polluted by trace metals [66]. In Wandoor, South Andaman, trace metals in seaweeds were found to be predominantly composed of manganese (Mn), followed by lead (Pb) and cadmium (Cd) [67, 68]. Pollution in Port Blair is primarily linked to land runoff, sewage outfalls, and tidal flows, whereas studies in Aerial Bay indicate greater pollution due to anthropogenic activities. In contrast, Rangat Bay experiences less contamination, attributed to effective oceanic flushing and natural water circulation mechanisms [69, 70].

In the context of the Middle Andaman region, potential anthropogenic sources contributing to trace metal enrichment include agricultural runoff, improper waste disposal,

vehicular emissions, fishing harbor operations, and limited but growing urbanization. These localized human activities, when combined with natural geological inputs, play a key role in shaping the spatial distribution of heavy metals in coastal and marine environments. These findings underscore the dual influence of geological and human factors on trace metal distribution in seawater, with notable implications for both water and soil quality across the Andaman Islands.

5 Conclusion

The geochemical and mineralogical investigation of soil and rock samples from Middle Andaman reveals a complex geological setting influenced by diverse sediment sources and environmental processes. XRD and XRF analyses confirmed the dominance of silicate, oxide, and carbonate minerals—primarily quartz, feldspar, and mica—along with metamorphic indicators like garnet and kyanite, suggesting contributions from both igneous and metamorphic rocks. Geochemical classification identified litho-arenite as the main lithology, supported by CIA values ranging from 67.98 to 87.27, indicating moderate to intense weathering consistent with tropical climatic conditions. Elemental correlations and major oxide relationships reflect inputs from Himalayan-derived detritus and local volcanic activity, while statistical tools such as PCA and HCA revealed distinct geochemical clusters associated with depositional, volcanic, and diagenetic processes. Groundwater analysis highlighted mineral dissolution and precipitation dynamics, with spatial variability in trace metals (Fe, Mn, Pb, Cd) suggesting both geogenic and anthropogenic influences, particularly near Aerial Bay and Port Blair.

Overall, the study demonstrates the effectiveness of an integrated geochemical and environmental approach in characterizing sedimentary processes, weathering patterns, and groundwater interactions, while emphasizing the need for long-term monitoring and interdisciplinary strategies to support sustainable water resource management in the Andaman region. High-resolution remote sensing and GIS can significantly enhance sedimentary and hydrological modelling, strengthening environmental assessments. Robust monitoring, informed policies, and targeted interventions are essential to safeguard coastal and groundwater systems, reduce future risks, and support long-term sustainable development.

Acknowledgements
The authors are thankful to the National Geochronology Facility at IUAC for the XRF analysis.

Author contributions
P.K. wrote the manuscript; V.K. and S.M. did the Editing and review; S.M. did supervision; P.K., and D.K. methodology.

Data availability
The datasets generated during and/or analyzed during the current study are available from the corresponding author on reasonable request.

Declarations

Competing interests
The authors declare no competing interests.

Received: 16 December 2024 / Accepted: 31 July 2025
Published online: 11 August 2025

References

1. Obasi RA, Madukwe HY. Use of geochemistry to study the provenance, tectonic setting, source-area weathering and maturity of Igarra marble, southwest, Nigeria. Am J Eng Res (AJER). 2016;5(6):90–9.

2. Garzanti E, Limonta M, Resentini A, Bandopadhyay PC, Najman Y, Andò S, Vezzoli G. Sediment recycling at convergent plate margins (Indo-Burman ranges and Andaman–Nicobar Ridge). Earth Sci Rev. 2013;123:113–32.
3. Armienti P, Messiga B, Vannucci R. Sand provenance from major and trace element analyses of bulk rock and sand grains. Terra Antartica. 1998;5(3):589–99.
4. Zarasvandi A, Carranza EJM, Ellahi SS. Geological, geochemical, and mineralogical characteristics of the Mandan and Dehnow bauxite deposits, Zagros fold belt, Iran. Ore Geol Rev. 2012;48:125–38.
5. Torró L, Proenza JA, Aiglsperger T, Bover-Arnal T, Villanova-de-Benavent C, Rodríguez-García D, Salas R. Geological, geochemical and mineralogical characteristics of REE-bearing Las Mercedes bauxite deposit, Dominican Republic. Ore Geol Rev. 2017;89:114–31.
6. Eliopoulos DG, Economou-Eliopoulos M. Geochemical and mineralogical characteristics of Fe–Ni-and bauxitic-laterite deposits of Greece. Ore Geol Rev. 2000;16(1–2):41–58.
7. Kumar P, Mukherjee S. Impact of limestone caves and seawater intrusion on coastal aquifer of middle Andaman. J Contam Hydrol. 2023;256:104197.
8. Chatterjee S, Scotese CR, Bajpai S. (2017). The restless Indian plate and its epic voyage from Gondwana to Asia: its tectonic, paleoclimatic, and paleobiogeographic evolution.
9. Pal T, Chakraborty PP, Gupta TD, Singh CD. Geodynamic evolution of the outer-arc–forearc belt in the Andaman islands, the central part of the Burma–Java subduction complex. Geol Mag. 2003;140(3):289–307.
10. Hamilton WB. Tectonics of the Indonesian region. Volume 1078. US Government Printing Office; 1979.
11. Tepanosyan G, Sahakyan L, Maghakyan N, Saghatelyan A. Identification of Spatial patterns, geochemical associations and assessment of origin-specific health risk of potentially toxic elements in soils of Armavir region. Armen Chemosphere. 2021;262:128365.
12. Curtis CD. Aspects of Climatic influence on the clay mineralogy and geochemistry of soils, palaeosols and clastic sedimentary rocks. J Geol Soc. 1990;147(2):351–7.
13. Joseph A. Investigating seafloors and oceans: from mud volcanoes to giant squid. Elsevier; 2016.
14. Bunaciu AA, UdriŞTioiu EG, Aboul-Enein HY. X-ray diffraction: instrumentation and applications. Crit Rev Anal Chem. 2015;45(4):289–99.
15. Shackley MS. (2011). An introduction to X-ray fluorescence (XRF) analysis in archaeology. X-ray fluorescence spectrometry (XRF) in geoarchaeology, 7–44.
16. Monecke T, Köhler S, Kleeberg R, Herzig PM, Gemmell JB. Quantitative phase-analysis by the Rietveld method using X-ray powder-diffraction data: application to the study of alteration halos associated with volcanic-rock-hosted massive sulfide deposits. Can Mineral. 2001;39(6):1617–33.
17. Hou X, He Y, Jones BT. Recent advances in portable X-ray fluorescence spectrometry. Appl Spectrosc Rev. 2004;39(1):1–25.
18. Ganai JA, Rashid SA, Alam MM. Petrography and geochemical studies of upper paleozoic sandstones from the Tethys himalaya, Spiti valley, Himachal Pradesh. J Appl Geochem. 2016;18(1):3–14.
19. Das BK, Haake BG. Geochemistry of Rewalsar lake sediment, lesser himalaya, india: implications for source-area weathering, provenance and tectonic setting. Geosci J. 2003;7:299–312.
20. Dash B, Sahu KN, Bowes DR. Geochemistry and original nature of precambrian khondalites in the Eastern ghats, orissa, India. Earth Environ Sci Trans Royal Soc Edinb. 1987;78(2):115–27.
21. Banerji US, Dubey CP, Goswami V, Joshi KB. Geochemical indicators in provenance Estimation. Geochemical treasures and petrogenetic processes. Singapore: Springer Nature Singapore; 2022. pp. 95–121.
22. Miriyala P. (2017). Late Quaternary geochemical history of lithogenic sedimentation in the Andaman Sea (Doctoral dissertation, Goa University).
23. Sharma BK. Environmental chemistry. Krishna Prakashan Media; 2014.
24. Jonathan MP, Ram-Mohan V, Srinivasalu S. Geochemical variations of major and trace elements in recent sediments, off the Gulf of mannar, the Southeast Coast of India. Environ Geol. 2004;45:466–80.
25. Romic D, Romic M, Zovko M, Bakic H, Ondrasek G. Trace metals in the coastal soils developed from estuarine floodplain sediments in the Croatian mediterranean region. Environ Geochem Health. 2012;34:399–416.
26. Ali MH, Mustafa ARA, El-Sheikh AA. Geochemistry and Spatial distribution of selected trace metals in surface soil of sohag, egypt: a multivariate statistical and GIS approach. Environ Earth Sci. 2016;75:1–17.
27. Zhang C, Yu ZG, Zeng GM, Jiang M, Yang ZZ, Cui F, Hu L. Effects of sediment geochemical properties on trace metal bioavailability. Environ Int. 2014;73:270–81.
28. Temple RC. Andaman and nicobar Islands. Asian Educational Services; 1994.
29. Kumar P, Vishwakarma CA, Singh P, asthana H, Rena V, mate CC, Mukherjee S. Hydrogeochemical characterization and water quality evaluation for drinking and irrigation purposes of coastal aquifers of middle Andaman. Discover Appl Sci. 2024;6(5):228.
30. Curray JR. Tectonics and history of the Andaman sea region. J Asian Earth Sci. 2005;25(1):187–232.
31. Morley CK, Searle M. Chapter 5 regional tectonics, structure and evolution of the Andaman–Nicobar Islands from ophiolite formation and obduction to collision and back-arc spreading. Geol Soc Lond Mem. 2017;47(1):51–74.
32. Sloan RA, Elliott JR, Searle MP, Morley CK. (2017). Active tectonics of Myanmar and the Andaman Sea.
33. Bandopadhyay PC, Carter A. Chapter 6 geological framework of the Andaman–Nicobar Islands. Geol Soc Lond Mem. 2017;47(1):75–93.
34. Srivastava DK, Dave A, Dangwal V. Sequence stratigraphy of the Andaman basin, Northern Indian ocean. Mar Pet Geol. 2021;133:105298.
35. Bandopadhyay PC, van Hinsbergen DJ, Bandyopadhyay D, Licht A, Advokaat EL, Plunder A, Trabucho-Alexandre JP. Paleogeography of the West Burma block and the Eastern Neotethys ocean: constraints from cenozoic sediments shed onto the Andaman-Nicobar ophiolites. Gondwana Res. 2022;103:335–61.
36. Chakraborty N, Mandal A, Nagendra R, Srimani S, Banerjee S, Sarkar S. (2021). Cretaceous deposits of India: a review. *Mesozoic Stratigraphy of India: a multi-proxy approach*, 39–85.
37. Mageswaran T, Sachithanandam V, Sridhar R, Mahapatra M, Purvaja R, Ramesh R. Impact of sea level rise and shoreline changes in the tropical Island ecosystem of Andaman and nicobar region, India. Nat Hazards. 2021;109:1717–41.
38. Kumar P, Singh P, Asthana H, Yadav B, Mukherjee S. Groundwater potential zone mapping of middle Andaman using multi-criteria decision-making and support vector machine. Groundw Sustainable Dev. 2024;26:101191.

39. Kelemen PB, Matter JM, Teagle DAH, Coggon JA, Oman Drilling Project Science Team. Methods and explanatory notes. Proc Oman Drill Project: Coll Stn TX (International Ocean Discovery Program). 2020.
40. Lindholm RC. 1987. Mineral identification using X-ray diffraction. In: A Practical Approach to Sedimentology, pp. 124–153.
41. Chandrasekaran A, Rajalakshmi A, Ravisankar R, Kalarasai S. Analysis of beach rock samples of Andaman island, India by spectroscopic techniques. Egypt J Basic Appl Sci. 2015;2(1):55–64.
42. Nesbitt HW, Young GM. Prediction of some weathering trends of plutonic and volcanic rocks based on thermodynamic and kinetic considerations. Geochim Cosmochim Acta. 1984;48(7):1523–34.
43. Alqahtani F, Khalil M. Geochemical analysis for evaluating the paleoweathering, paleoclimate, and depositional environments of the siliciclastic Miocene-Pliocene sequence at Al-Rehaili area, Northern jeddah, Saudi Arabia. Arab J Geosci. 2021;14:1–12.
44. Moore RM. Tfie Skiddaw group of cumbria: early ordovician turbidite sedimentation and provenance on an evolving microcontinental margin. Submitted in accordance with the requirements for the degree of Doctor of philosophy. University of Leeds Department of Earth Sciences; 1992. p. 300.
45. Madukwe HY, Ayodele SO, Akinyemi SA, Adebayo OF. Classification, maturity, provenance, tectonic setting, and sourcearea weathering of Ipole and Erin Ijesa stream sediments, South West Nigeria. Int J Adv Sci Tech Res. 2016;1(6):232–55.
46. Pettijohn FJ, Potter PE, Siever R. Sand and sandstone. 2nd ed. Berlin Heidelberg New York: Springer; 1987. p. 553.
47. Madukwe HY, Bassey CE. Geochemistry of the Ogwashi-Asaba formation, Anambra basin, nigeria: implications for provenance, tectonic setting, source area weathering, classification and maturity. Inter J Sci Techno. 2015;4(7):312–27.
48. El-Desoky H, El-Rahmany M, Farouk S, Ahmed Khalil A, Fahmy W. Geochemical characteristics of goethite-bearing deposits in the Dakhla – Kharga oases, Western desert, Egypt. Int J Sci Eng Appl Sci (IJSEAS). 2015;1(8):72–85.
49. Dury GH. Quantitative measurement of available relief and of depth of dissection. Geol Mag. 1951;88:339–43.
50. Jing G, Huang Z, Fan H, Zhongguo Jin C, Yan Z, Zhang J. Mineralogy, geochemistry, and genesis of lateritic bauxite deposits in the Wuchuan–Zheng'an–Daozhen area, Northern Guizhou province, China. J Geochem Explor. 2013;130:44–59.
51. Shao J, Yang S, Li C. Chemical indices (CIA and WIP) as proxies for integrated chemical weathering in china: inferences from analysis of fluvial sediments. Sed Geol. 2012;265:110–20.
52. Wronkiewicz DJ, Condie KC. Geochemistry of archean shales from the Witwatersrand supergroup. South Afr Geochim Cosmochim Acta. 1987;51:2401–16.
53. Jacobson AD, Blum JD, Chamberlian CP, Craw D, Koons PO. Climate and tectonic controls on chemical weathering in the new Zealand Southern alps. Geochim Cosmochim Acta. 2003;37:29–46.
54. Ratcliffe KT, Morton AC, Ritcey DH, Evenchick CA. Whole-rock geochemistry and heavy mineral analysis as petroleum exploration tools in the Bowser and Sustut basins, British columbia, Canada. Bull Can Petrol Geol. 2007;55(4):320–36.
55. Blatt H, Middleton GV, Murray RC. Origin of sedimentary rocks. New Jersey: Printice Hall; 1972. p. 634.
56. Roaldest E, Thesis PD. Geol. Inst., Univ. of Oslo, Norway.
57. Noori A, Rais S. Geochemistry and detrital models of sandstone from Barakar formation in mand Valley basin, chhattisgark, india: implications for provenance, tectonic setting and paleo-weathering. Inter J Basic App Sci. 2014;14:124–33.
58. Scarciglia F, Sauer D, Zerboni A. Pleistocene paleosols of italy: pedostratigraphy, genesis, paleoclimate and geoarchaeology. Alp Mediterranean Quaternary. 2023;36(2):1–35.
59. Irfan TY. Mineralogy, fabric properties and classification of weathered granites in Hong Kong. Q J Eng GeolHydrogeol. 1996;29(1):5–35.
60. Tuğrul A, Zarif IH. Correlation of mineralogical and textural characteristics with engineering properties of selected granitic rocks from Turkey. Eng Geol. 1999;51(4):303–17.
61. Stoops G. Guidelines for analysis and description of soil and regolith thin sections. Wiley; 2021.
62. Ulmer-Scholle DS, Scholle PA, Schieber J, Raine RJ. A color guide to the petrography of sandstones, siltstones, shales and associated rocks. Volume 109. Tulsa, OK, USA: American Association of Petroleum Geologists; 2014.
63. Lazar OR, Bohacs KM, Macquaker JH, Schieber J, Demko TM. Capturing key attributes of fine-grained sedimentary rocks in outcrops, cores, and thin sections: nomenclature and description guidelines. J Sediment Res. 2015;85(3):230–46.
64. Rena V, Vishwakarma CA, Singh P, Roy N, Asthana H, Kamal V, Mukherjee S. Hydrogeological investigation of fluoride ion in groundwater of Ruparail and Banganga basins, Bharatpur district, rajasthan, India. Environ Earth Sci. 2022;81(17):430.
65. Singh P, Asthana H, Rena V, Kumar P, Kushawaha J, Mukherjee S. Hydrogeochemical processes controlling fluoride enrichment within alluvial and hard rock aquifers in a part of a semi-arid region of Northern India. Environ Earth Sci. 2018;77:1–15.
66. Roussos LA, Stout WF, Marden JI. Using new proximity measures with hierarchical cluster analysis to detect multidimensionality. J Educ Meas. 1998;35(1):1–30.
67. Thangaradjou T, Nobi EP, Dilipan E, Sivakumar K, Susila S. Trace metal enrichment in seagrasses of the Andaman Islands and its implication to the health of the coastal ecosystem. Indian J Mar Sci. 2010;39:85–91.
68. Karthick P, Siva Sankar R, Kaviarasan T, Mohanraju R. Ecological implications of trace metals in seaweeds: bio-indication potential for metal contamination in wandoor, South Andaman Island. Egypt J Aquat Res. 2012;38:227–31.
69. Sahu BK, Begum M, Khadanga MK, Jha DK, Vinithkumar NV, Kirubagaran R. Evaluation of significant sources influencing the variation of physicochemical parameters in Port Blair bay, South andaman, India by using multivariate statistics. Mar Pollut Bull. 2013;66:246–51.
70. Jha DK, Devi MP, Vinithkumar NV, Das AK, Dheenan PS, Venkateshwaran P, et al. Comparative investigation of water quality parameters of aerial and Rangat bay, the Andaman Islands using in-situ measurements and Spatial modeling techniques. Water Qual Exposure Health. 2013;5:57–67.

Publisher's note